ADVANCED ELECTROMAGNETIC NUMERICAL MODELING TECHNIQUES FOR VARIOUS PERIODIC AND QUASI-PERIODIC SYSTEMS

A Dissertation

Presented to

the Faculty of the Department of Electrical and Computer Engineering

University of Houston

In Partial Fulfillment

of the Requirements for the Degree

Doctor of Philosophy

in Electrical Engineering

by

Xichen Guo

December 2014

ADVANCED ELECTROMAGNETIC NUMERICAL MODELING TECHNIQUES FOR VARIOUS PERIODIC AND QUASI-PERIODIC SYSTEMS

Xichen Guo

Approved:

Chair of the Committee
Ji Chen, Professor
Electrical and Computer Engineering

Committee Members:

David R. Jackson, Professor
Electrical and Computer Engineering

Donald R. Wilton, Professor
Electrical and Computer Engineering

George Zouridakis, Professor
Engineering Technology

Driss Benhaddou, Associate Professor
Engineering Technology

Daniel Onofrei, Assistant Professor
Mathematics

Suresh K. Khator, Associate Dean
Cullen College of Engineering

Badri Roysam, Professor and Chair
Electrical and Computer Engineering

Acknowledgements

My sincerest appreciation goes to my esteemed advisers Dr. Ji Chen and Dr. David R. Jackson, for their guidance and support throughout this endeavor and their numerous invaluable contributions to this dissertation.

My special thanks goes to the faculties of the electromagnetic group. The knowledge and skills I learned in the antenna class given by Dr. Stuart A. Long and the numerical-methods class given by Dr. Donald R. Wilton inspired me for many ideas in this dissertation.

I am grateful to Dr. Marina Y. Koledintseva (formerly with the EMC lab in Missouri S&T) for the conductor surface roughness measurements. I am also appreciative of Dr. Yuancheng C. Pan (formerly with Huawei Technologies) for the sponsorship of the high-speed interconnect project.

Many thanks to the committee members of my dissertation: Dr. George Zouridakis, Dr. Driss Benhaddou, and Dr. Daniel Onofrei, for their great suggestions to my dissertation.

I would also like to thank the colleagues and friends in the Applied Electromagnetic Lab (AEL). Thank you Lintong Li for your encouragement and your unwavering love. Thank you Shi Feng for the support and help you provided at all times. Thank you Dr. Zubiao Xiong for the discussions and for being patient and resourceful. Thank you Xin Huang and Dawei Li for the meaningful suggestions for my research and life. Also many thanks to Xinyu Liu, Qingyan Wang, Kuang Qin, Qi Zeng, Mengna Yang, Jingshen Liu, Yanxiang Yu, Shurun Tan, Sohini Sengupta, Dr. Jianfeng Zheng, Dr. Yan Liu, Dr. Cong Gao and Dr. Minshen Wang for their technical efforts and suggestions, without which this research would never have come to fruition.

Last, but certainly not least, my deepest gratitude goes to my parents for their constant encouragement and total support towards the attainment of my goal.

ADVANCED ELECTROMAGNETIC NUMERICAL MODELING TECHNIQUES FOR VARIOUS PERIODIC AND QUASI-PERIODIC SYSTEMS

An Abstract

of a

Dissertation

Presented to

the Faculty of the Department of Electrical and Computer Engineering

University of Houston

In Partial Fulfillment

of the Requirements for the Degree

Doctor of Philosophy

in Electrical Engineering

by

Xichen Guo

December 2014

Abstract

This dissertation is mainly concerned with several advanced electromagnetic modeling techniques for practical complex systems, which involve periodic analyses. The focus is to reveal the physics of the electromagnetic wave interaction with the complex structures, and also to arrive at improved computational algorithms.

This dissertation consists of three self-contained parts, each discussing one modeling technique. Examples presented in this dissertation include (a) an analysis of conductor surface-roughness effects, (b) a novel model for vertical interconnects (vias) and (c) a leaky-wave study of a Fabry-Pérot resonant cavity antenna.

The first part investigates conductor surface roughness effects for stripline. An equivalent rough-surface-impedance is extracted using a periodic full-wave analysis and is then used for the modification of the transmission line per-unit-length parameter.

The second part proposes a semi-analytical analysis for massively-coupled vias with arbitrarily-shaped antipads, based on the reciprocity theorem. The use of reciprocity yields simple design formulas and is seen to greatly improve the computational efficiency, due to the fast-converging mode-matching calculation.

The third part presents a leaky-wave study of a Fabry-Pérot cavity antenna made from a patch array. The patch current densities are calculated using the array scanning method. Based on this, a "leaky-wave current" is defined and calculated using residue integration. In addition, the radiation properties of a large finite-size array (truncation effects) are evaluated.

All three proposed models are verified by full-wave simulations and/or measurements. Numerical results prove the effectiveness and accuracy of these models.

Table of Contents

List of Figures

List of Tables

Chapter 1

Introduction

1.1 Background

Electromagnetic analysis has changed the practice of electrical engineering in recent years. Electromagnetic theory is well-established with Maxwell's equations and a complete solution to Maxwell's equations can expedite many design processes for electrical systems. Using computationally efficient approximations to Maxwell's equations, or electromagnetic modeling, one can solve Maxwell's equations to obtain a better understanding of a complex system.

This dissertation is mainly concerned with some advanced electromagnetic modeling techniques for practical complex systems, especially those possessing a periodic or quasi-periodic feature. The focus is to reveal the physics of the electromagnetic wave interaction with complex structures, and thus to bring in physical insights, and finally to arrive at an improved algorithm. Examples presented in this dissertation include (a) an analysis of conductor surface roughness effects on stripline transmission lines, (b) a model to estimate the radiation and coupling effects of vertical interconnects (vias) and (c) a leaky-wave study of a Fabry-Pérot resonant cavity antenna using a two-dimensional patch array.

The canonical problem in example (a) and example (c) involves a periodic/quasi-periodic structure. Periodic numerical methods are used to analyze the electromagnetic fields on these two structures. In example (a), the quasi-periodic rough conductor surface is exposed to plane-waves, and the periodicity is preserved by applying a periodic boundary condition (phase-delay walls). In example (c), the periodic patch array is excited with a non-periodic source (a horizontal electric dipole), and the

periodicity of each space harmonic is accounted for by a periodic Green's function. Example (b) solves the fields among a via array, a truncated periodic structure. However, the proposed analysis is not limited by this periodicity and can handle any arbitrary layout of vias.

1.1.1 Interconnect Modeling for High-Speed Circuits

Example (a) and (b) fall into the category of interconnect modeling for high-speed integrated circuits. Figure 1.1 is a diagram of a typical high-speed link consisting of horizontal interconnects (transmission lines) and vertical interconnects (vias).

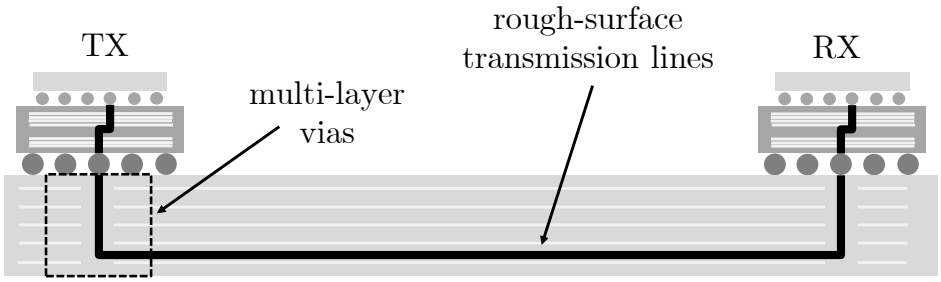

Figure 1.1. A typical high-speed link consisting of rough-surface transmission lines and massively-coupled multi-layered vias [1].

High clock speed has given rise to serious signal integrity issues. Signal distortions, i.e., attenuation, reflection, mode conversion, etc., are likely to occur when transmitting through a stripline transmission line or a via interconnect. The signal-to-noise-ratio is substantially lowered, making the links inappropriate for signal transmission. In order to raise the throughput of such noisy links, active-circuit compensation techniques, e.g., pre-emphasis and equalization [2], [3], are therefore used to flatten the roll-off of the channels' frequency responses. However, an optimum design of these signal processing circuit blocks strongly relies on the behavior of the passive links themselves. Therefore, an accurate, efficient and parametric model for the interconnect system is highly demanded as a design tool.

1.1.1.1 Conductor Surface Roughness Effects

During the printed circuit board (PCB) fabrication processes, the conductor foils used to laminate the transmission lines, e.g., striplines, are usually roughened to enhance the adhesion to the dielectric substrates. The theory of signals propagating on a smooth stripline transmission line is classical [4]–[6]. In the absence of surface roughness, dielectric loss scales with frequency and conductor loss scales with the square root of frequency [7]. However, when the conductor surface is roughened, the currents become concentrated into the roughness and have a longer path length, creating a more lossy and dispersive system. These effects are not predicted by the conventional skin-depth formula and they become significant for the high-frequency components of a signal and have been shown to greatly degrade the signal [8]–[10]. Extensive studies on the extra losses and dispersion due to the conductor surface roughness effects exist [11]–[16].

1.1.1.2 Massively-Coupled Vias

Vias provide vertical interconnections between stacked PCB layers with much shorter and denser connectivity compared to conventional horizontal and bondwire interconnects [17], [18]. A via presents one of the most significant impedance discontinuities of an interconnect system. In the low frequency region, a via behaves like an inductor. As the signal frequency increases, the radiation from the via barrels (conducting pins) and the antipads (apertures) becomes strong and the accuracy of using the simple inductor model starts to deteriorate [7].

For vias with circular antipads, the radiation and coupling mechanisms have been studied extensively [19]–[33]. However, only a few papers address the arbitrarily-shaped antipads [34]–[38]. For antipads with an irregular shape, the aperture field is usually complicated and requires expensive numerical evaluation.

1.1.2 Leaky-Waves on a Fabry-Pérot Antenna

Example (c) presents a leaky-wave study of a Fabry-Pérot resonant cavity antenna made from patch arrays. In this dissertation, it is established that this Fabry Pérot antenna is a good leaky-wave antenna because of a leaky-wave dominance.

The Fabry-Pérot resonant cavity antenna is used to obtain directive beams with a simple source excitation, and a design using a periodic patch array is given in Figure 1.2, radiating a pencil beam at broadside. The design considered in this dissertation is also referred to as a "quasi-uniform" structure since it radiates through the lowest-order space harmonic. The canonical problems addressed in the largest part of the relevant literature are the interaction between periodic patches and plane waves, and the determination of the dispersion features of the Bloch modes supported by the periodic structure in the absence of sources [39]–[41]. However, the studies of the non-periodically-excited periodic structures, as in the case of the Fabry-Pérot antenna given in Figure 1.2, are scarce.

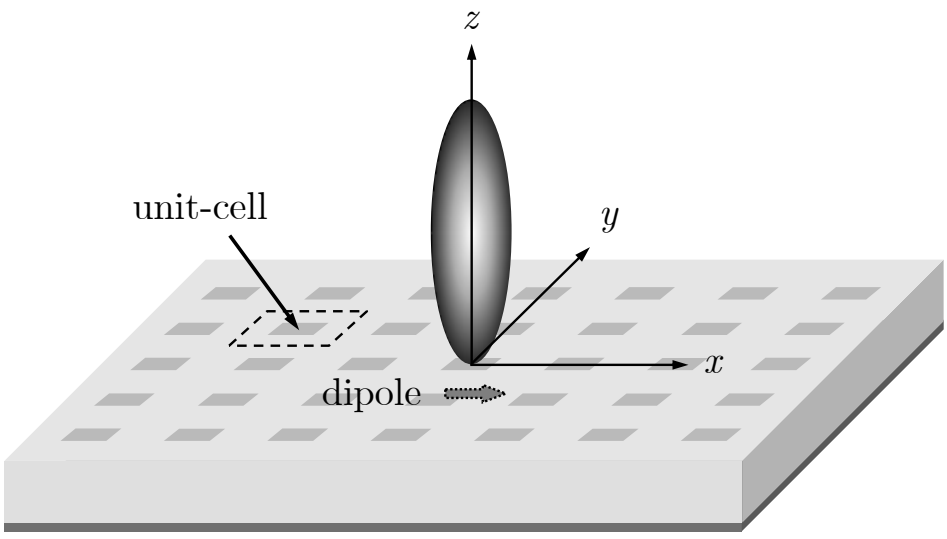

Figure 1.2. A Fabry-Pérot resonant cavity antenna made of a periodic patch array. This antenna is excited by a single x-directed electrical dipole inside the substrate.

Historical studies have shown that the Fabry-Pérot resonant cavity antenna operates as a leaky-wave antenna [42]–[44]. The leaky-wave theory gives compact and elegant explanations on the fundamental radiation mechanism, as well as antenna's near-field properties, e.g. currents, input impedance, etc.. In addition, for a leaky-wave-dominant antenna, one can estimate the "truncation effects" of a large patch antenna array.

1.2 Scope and Contributions of the Dissertation

In this dissertation, we present three novel electromagnetic models for the aforementioned structures. The structures discussed include (a) a stripline transmission line with a rough conductor surface, (b) a multilayer PCB with densely packed vias and (c) a Fabry Pérot resonant cavity leaky-wave antenna.

1.2.1 A Model for Rough-Surface Stripline

We propose a model for a stripline transmission line with periodically roughened conductor surfaces. The conductor surface roughness effects on signal propagation, including signal attenuation and phase-delay, are analyzed.

A periodic structure model is introduced to approximate the surface roughness, which in turn is represented in terms of an equivalent surface impedance due to the size difference between the period and the wavelength. Two models, a periodic cavity and a long waveguide, both of which can simulate an infinite periodic roughened conductor surface, are proposed. The wavenumber for the fundamental Floquet mode is extracted to calculate the equivalent surface impedance for the rough surface.

The equivalent surface impedance, which accounts for the rougher sides of the conductors, is used to modify the per-unit-length transmission line parameters. Results have shown that as the amplitude of the conductor surface roughness increases, the conductor loss increases significantly, and the effective dielectric constant also increases noticeably.

1.2.2 A Model for Vias with Arbitrarily-Shaped Antipads

We propose a semi-analytical model for a dense layout of vias in an infinite parallel-plate environment. An arbitrarily-shaped antipad configuration is addressed.

The network parameters for the multi-via structure are calculated based on the reciprocity theorem, where a unit-strength magnetic testing ring frill is used to compute the currents flowing on the surfaces of the via barrels. The motivation for using reciprocity is to bypass the sophisticated computation of the radiation from the irregular-shaped antipad aperture; instead, a much simpler field from the reciprocal testing source is formulated. Also, the higher-order parallel-plate mode radiation from this testing frill is highly localized and hence there is little interaction among vias through higher-order modes. This rapidly-decaying field makes the mode-matching computation converge very fast. Furthermore, the testing frill radiates an omnidirectional reactive near field that can be expressed in a closed-form, making the method computationally efficient. Numerical examples demonstrate the efficiency and accuracy of the proposed algorithm.

1.2.3 A Leaky-Wave Study on a Fabry-Pérot Antenna

We present a leaky-wave study on a Fabry-Pérot resonant cavity antenna using a patch array. A definition of a leaky-wave current is proposed as a residue integration that corresponds to a leaky-wave pole on the "improper" Riemann sheet.

In order to study the leaky-wave dominance of this antenna, the surface current densities — both the total currents and those due to leaky-wave radiations — are computed, using the array-scanning method (ASM). ASM is favorable for the problem of non-periodic excitations on a periodic structure. The non-periodic source is first expanded in terms of its spacing-harmonic counterparts, and then synthesized through a spectral integration.

The leaky-wave contribution is extracted by deforming the path into the complex

plane to capture the residues corresponding to the leaky-wave poles on the "improper" Riemann sheet. An asymptotic formula is thus derived using the method of steepest descent. The leaky-wave current is shown to be dominant among the total current, and hence the Fabry-Pérot antenna discussed in this dissertation turns out to be a good *leaky-wave antenna*.

The calculation of the patch current then allows us to investigate the radiation properties of a finite-size leaky-wave antenna assuming an "ideal absorber" is placed at the array boundaries, and hence no reflection arising from the truncation. The "truncation effects" are studied and radiation patterns are computed.

1.3 Dissertation Outline

This dissertation has three self-contained parts, each addressing one of the three aforementioned periodic or quasi-periodic structures. The rest of this dissertation is organized as follows.

Chapter 2 discusses the conductor surface roughness effects with the application to stripline interconnects. We begin this chapter with a historical review of some existing research. Next, we analyze the conductor surface roughness effects using a periodic analysis, introducing two possible structures — a periodic cavity and a long waveguide — to extract an equivalent rough surface impedance. This surface impedance is then used to modify the per-unit-length $RLGC$ parameters. At the end of this chapter, we validate the proposed approach using numerical comparisons with full-wave simulations and also measurements.

Chapter 3 presents a semi-analytical model for a vias with arbitrarily-shaped antipads. We begin this chapter with a historical review of the existing models for via interconnects. Next, we introduce the methodology using reciprocity, where the port current formula is first derived by introducing a "testing" frill, followed by the computation of the radiation from the testing frill that appears in the formulation.

The efficiency of the proposed algorithm is then discussed and a closed-form expression for the testing frill radiation is given. At this end of this chapter, numerical results are compared with those from full-wave simulations.

Chapter 4 presents a leaky-wave study on a Fabry-Pérot resonant cavity antenna with a two-dimensional patch array implementation. We begin this chapter with a historical review of the existing research on the two-dimensional Fabry-Pérot leaky wave antenna. Next we introduce the ASM formulation to compute the antenna currents (the total currents), based on which a leaky-wave current is defined and computed using a leaky-pole residue integration. Two asymptotic formulas for the leaky-wave currents are then derived. Using the patch current densities, radiation patterns are then calculated and the contribution of the leaky wave is evaluated. The "truncation effects" under the "ideal absorber" assumption are next studied and the radiation patterns from truncated patch arrays are computed.

Chapter 5 gives a summary of the main conclusions for the models presented in this dissertation. In the end, we present some recommendations of the future works.

Chapter 2

Conductor Surface Roughness Effects

Chapter 2 discusses the conductor surface roughness effects on signal propagation on a stripline transmission line. The stripline is laminated using copper foils having surface roughness. When the roughness on the copper foil is morphologically close to a periodic structure, computing the voltage/current wave propagating on the transmission line becomes a canonical problem in calculating the plane-wave interaction with a periodic structure.

According to Floquet theory, a plane-wave incidence on a periodic structure excites an infinite numbers of Floquet modes (space harmonics). When the periodicity of the structure is substantially smaller than the wavelength of the incoming plane wave, as in the case of copper foils used to make stripline transmission lines, the 0^{th}-order Floquet mode becomes dominant. The plane-wave-like 0^{th}-order mode allows us to replace the rough surface by an equivalent surface impedance boundary condition enforced on a flat surface, so as to avoid the heavy computation of the fields on a corrugated surface.

There are mainly two approaches to compute the fields on an infinite periodic structure (from which the wavenumber of the 0^{th}-order Floquet mode can be extracted). The first approach is to apply periodic boundary conditions, using the fact that a field on a periodic structure due to plane-wave excitation is also periodic. In the first approach, the structure naturally extends to infinity because of the periodic boundary conditions. The second approach is to use a finite yet large structure to "brute force" the results for an infinite periodic structure.

We begin this chapter by a historical review of the existing research on the surface roughness effects in Section 2.1. Section 2.2 discusses the analysis of the

conductor surface roughness effects using a periodic analysis, introducing two possible structures used to extract an equivalent rough surface impedance. In Section 2.3, the rough surface impedance is used to modify the per-unit-length $RLGC$ parameters. Section 2.4 validates the proposed approach using a numerical comparison with full-wave simulations and also measurements. Section 2.5 provides some conclusions and comments on the proposed model.

2.1 Introduction

Printed circuit board (PCB) fabrication involves intensive laminating processes, and the inner-layer adhesion between the metal foils and the substrate should be strong enough to tolerate the arising thermal stresses. In order to enhance this adhesion effect, the metal foils used to laminate the PCB substrates are intentionally roughened. The roughness treatment usually creates foils having tooth-like protrusions and the root-mean-square (RMS) of the "tooth" height varies from several to tens of micrometers. This tooth height largely exceeds the skin-depth of the interconnect metal, and indicates that the penetrating currents will be flowing inside the "teeth." Consequently, the currents become concentrated into the roughness and have a longer path length, creating a more lossy and dispersive system. These effects are not predicted by the conventional skin-depth formula. Therefore, a modification is required in order to accurately analyze the conductor surface roughness effects.

Extensive studies on the effects of conductor surface roughness exist. One of the most well-known methods is the one proposed by Hammerstad and Jensen [11], introducing a multiplicative correction term to the attenuation constant of a smooth conductor. It is based on Morgan's model [45], where the author studied the increased current path length on a corrugated surface with two-dimensional roughness. The Hammerstad and Jensen formula and the Morgan's model are considered to be accurate only when the RMS value of the roughness is small (less than approximately 2 μm [7]),

and is less applicable for PCB traces with a much rougher surface (up to 10 μm). Also, these methods predict a saturation limitation that the maximum value of the multiplicative factor is two, which is a non-physical effect.

Another category of research relies on the small perturbation theory (SPT). A systematic research has been done in [46]. It was first introduced to the conductor surface roughness analysis by Sanderson [12], using a 2-D periodic profile along the direction of propagation. Gu et al. [13] then utilize SPT based on power spectrum density (PSD) for a randomly roughened surface. The same SPT analysis is also applied to calculate the surface impedance on the dielectric-conductor interface as proposed by Holloway et al. [14], [47], and a metal-dielectric-dielectric interface, as proposed by Koledintseva et al. [48]. However, these approaches require both the amplitude and the slope of the roughness profiles to be small. This limitation makes them less suitable to analyze the surface roughness effects for copper foils used to laminate a stripline transmission line, where the dendritic profiles usually have large slopes.

Ball-shape models are morphologically closer to the real-world PCB surface roughness, as proposed by Hall et al. [15] where the protrusions are modeled as periodic hemispheroids, and by Huray et al. [16] using the "snow-ball" model (multi-stage spheres). A systematic study can be found in [49]. These models are based on purely analytic methods, computing the scattering from a sphere with an impedance surface. They are efficient to implement, but they both lack consideration of the mutual coupling from the neighboring spheres, therefore underestimating the attenuation effects of the surface roughness.

Besides the extra conductor loss that increases the attenuation, previous researchers have also discovered that the surface roughness has influence on the phase constant. Horn et al. [50] found that the effective dielectric constant increases due to the existence

of conductor surface roughness, corresponding to a change in the surface reactance. This extra surface reactance due to the surface roughness raises the measurement error of the substrate dielectric property of the laminating substrate with the presence of the conductor surface roughness effects. In order to correct the measured dielectric properties, one can use the differential measurement technique [51].

2.2 Surface Impedance for Rough Conductors

2.2.1 Periodic Surface Roughness Parameters

In reality, the conductor surface roughness possesses a quasi-periodic morphology (see Figure 2.1) with the periodicity, roughness shape, and roughness amplitude being random variables. Here the term "quasi-periodic" indicates a small deviation from a strictly-periodic structure, or a perturbed periodic structure. The interaction of the roughened conductor with a plane wave, therefore, is a random process. In order to extract the mean response of this random process, the conductor surface is taken to be the unperturbed periodic structure.

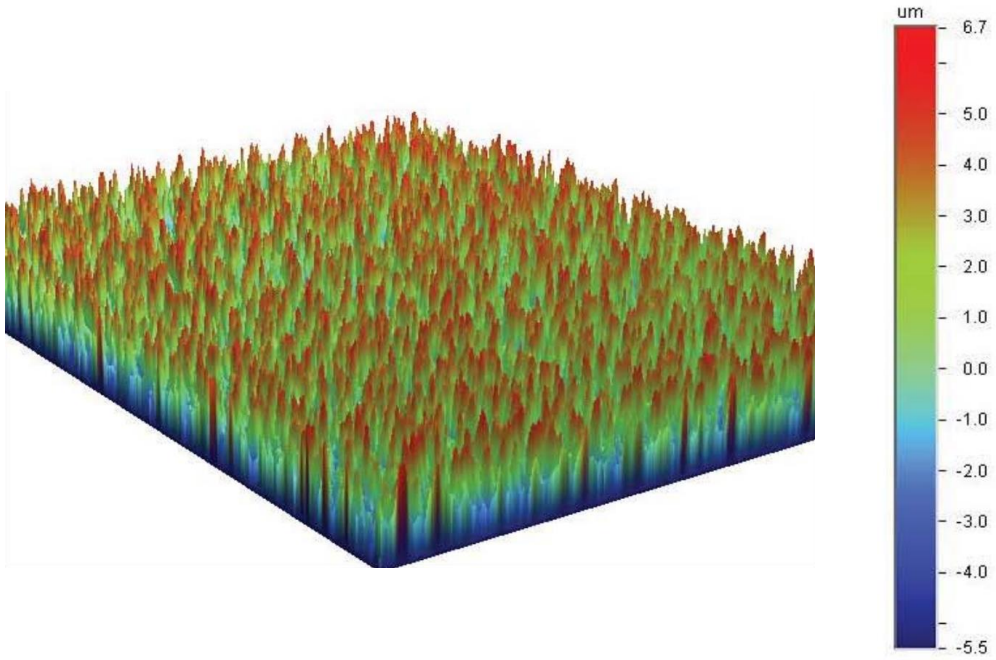

Figure 2.1. Wyko optical profiler surface morphology and roughness measurements of a treated half-ounce-copper foil [52].

As can be seen from Figure 2.1, the copper foil roughness treatment procedure creates a granular dendritic profile that is modeled as a periodic array of hemispheroids. Figure 2.2 shows the periodic structure involved and the parameters required to describe the periodic structure: the period Λ_r, the peak-to-valley roughness amplitude (the hemispheroid height) A_r and the base radius r_{base}. These parameters are measured using the scanning electron microscopy (SEM) on a slice of transversely-cut stripline transmission line. The mean values of these parameters are obtained using the SEM pictures taken on several samples. The conductivity of the hemispheroids and the semi-infinite layer below them is taken as pure copper, with a conductivity of $\sigma = 5.8 \times 10^7$ S/m. Practically the semi-infinite layer would be truncated to a finite copper slab with thickness d of several skin-depths.

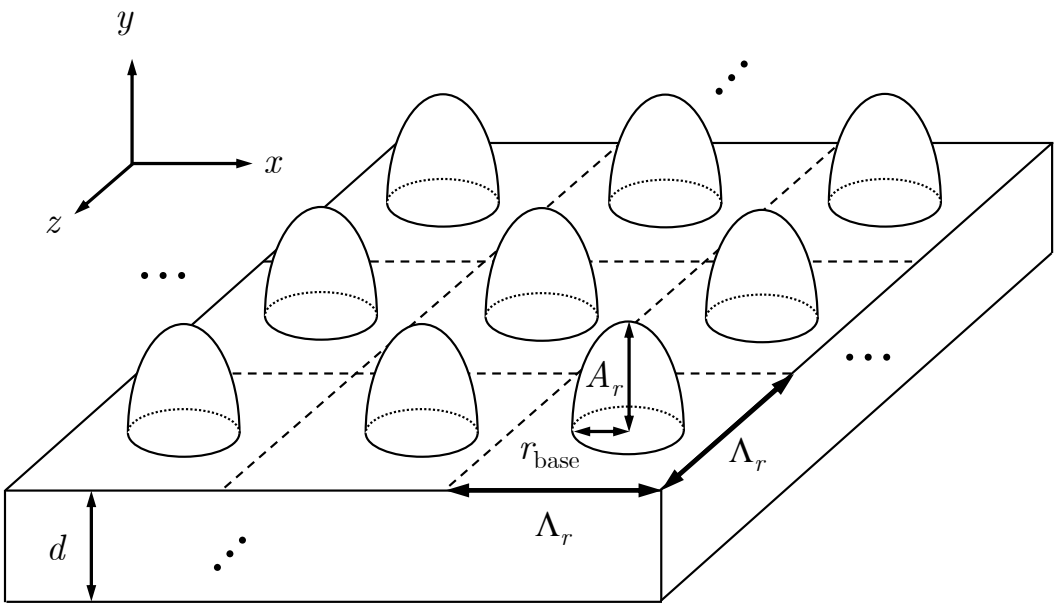

Figure 2.2. An infinite periodic structure used to represent the conductor surface roughness.

Different copper foils are categorized by their roughness level, e.g., there are STD–standard, VLP–very-low-profile, and HVLP–hyper-very-low-profile foils. Figure 2.3 shows a sample of the cross-sectional SEM picture for a stripline made with STD foil. More detailed geometry dimensions for PCBs with various foils are listed in Table 2.1.

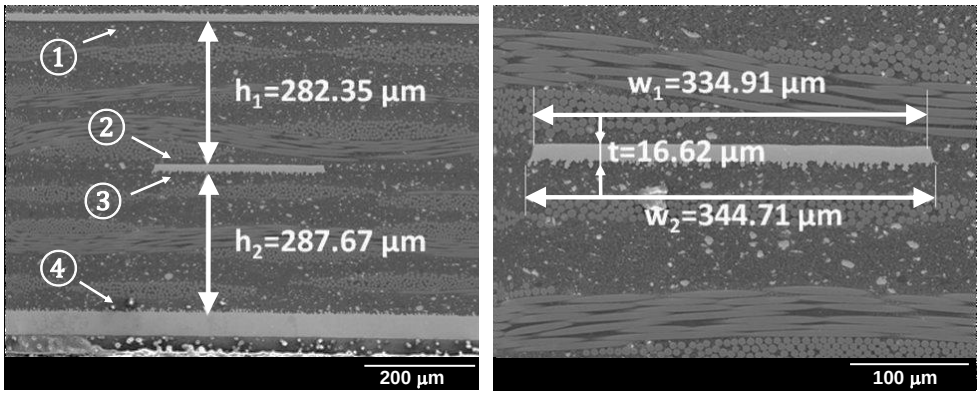

Figure 2.3. SEM images for a stripline with STD foils, showing a cross-sectional view of each stripline structure (left) and an expanded view of the central strip conductor (right).

The roughness parameters obtained from SEM pictures of the test boards are listed in Table 2.2. The standard roughness parameters [53] R_z (the average height difference between the five highest peaks and the five lowest valleys in the roughness profile) and R_{rms} (the root-mean-square average of the departures of the roughness profile from the mean line) are also included.

Table 2.1. Macroscopic profile parameters of striplines with different copper foils.[1]

Foil type	w_1	w_2	t	h_1	h_2
STD	334.91	344.71	16.62	282.35	287.67
VLP	364.02	368.84	15.38	297.79	275.73
HVLP	327.27	331.71	15.42	290.44	292.64

[1] All length units are in micrometers.

Table 2.2. Roughness parameters for different foils[1]

Foil type	A_r	Λ_r	r_{base}	R_z	R_{rms}
STD	7.975	10.62	3.54	8.41	1.91
VLP	3.353	7.275	2.43	4.19	0.92
HVLP	1.604	4.685	1.56	2.29	0.44

[1] All length units are in micrometers.

The multilayer PCB laminating procedure uses two types of dielectric material: the "core" and the "prepreg," forming the lower and upper half of the substrate respectively, as shown in Figure 2.3. The metal foils are chemically roughened on surfaces (3) and (4) indicated in Figure 2.3 for adherence in the lamination process. The peak-to-valley roughness amplitude A_r and period Λ_r are used on the rougher side of the conductors [surface (3) and (4) in Figure 2.3], where the ratio of $A_r/\Lambda_r > 0.3$. On the opposite smoother side of the foil [surfaces (1) and (2) in Figure 2.3], this ratio is significantly smaller (typically $A_r/\Lambda_r < 0.1$), and the roughness contribution from this side will be neglected.

2.2.2 Rough Surface Impedance

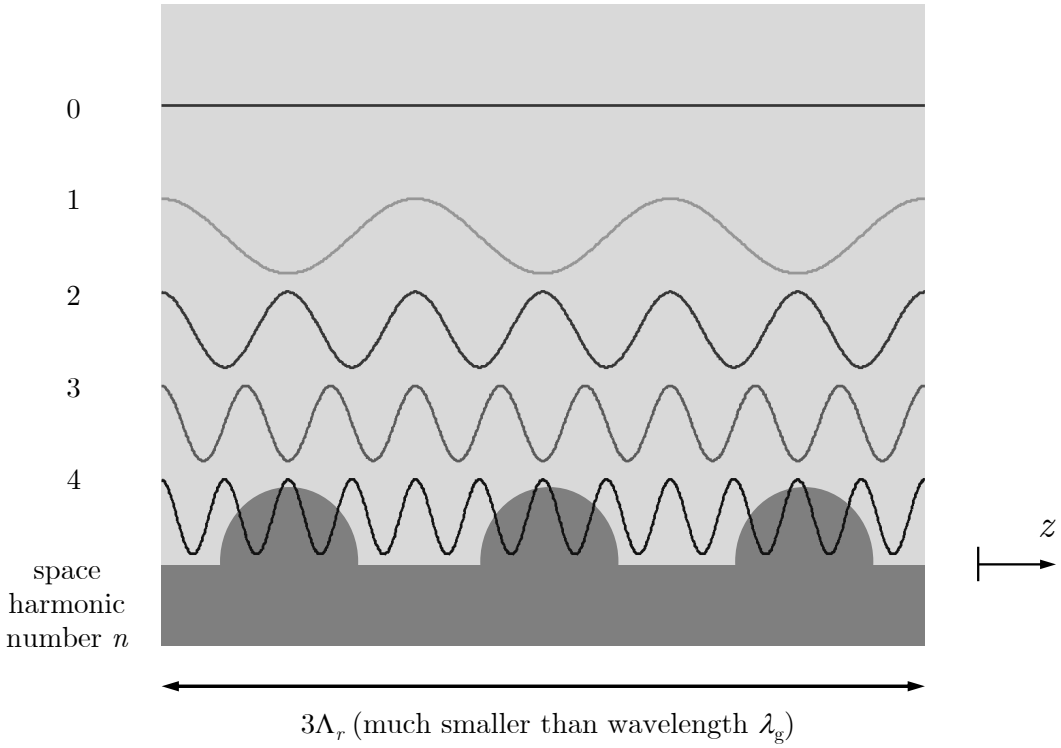

Figure 2.4. Space-harmonics supported by a periodic structure with period Λ_r. The n^{th}-order space harmonic has a z-variation of $e^{-jk_{zn}z}$ and a wavenumber of $k_{zn} = k_{z0} + 2\pi n/\Lambda_r$.

According to Floquet theory [54], an infinite numbers of space harmonics (Floquet modes) exist on a periodic structure (see Figure 2.4). The n^{th}-order space harmonic

has a z-dependence of $e^{-jk_{zn}z}$, where

$$k_{zn} = k_{z0} + \frac{2\pi n}{\Lambda_r}, \tag{2.1}$$

and the wavenumber in y-direction is given by

$$k_{yn} = \sqrt{k^2 - k_{zn}^2}, \tag{2.2}$$

since all unit cells are in phase along the x-direction ($k_{x0} = 0$). It should be noted that all higher-order variations along the x-direction with $k_{xm} = 2\pi m/\Lambda_r$ are ignored.

In the copper surface roughness problem where the period Λ_r is much smaller than the guided-wave wavelength λ_g in the frequency range of interest, k_{yn} is almost pure imaginary except when $n = 0$. That is, all high-order Floquet modes are evanescent except for the fundamental 0^{th}-order Floquet mode. The field would only consist of the fundamental mode and behave like a plane wave if the observation point is sufficiently far away from the rough surface. Hence we can replace the corrugated surface by proper enforcement of a *flat* impedance-type of boundary condition at the rough interface to avoid expensive numerical computation of the microscopic electromagnetic fields.

The transverse resonance technique (TRT) [5] can then be applied to calculate the equivalent surface impedance. This can be done by introducing a piece of perfect electrical conductor (PEC) and placing it parallel to the base of the rough surface. The distance from the PEC surface to the base of the rough surface is s, and the value of s is chosen so that the PEC insert is in the "plane-wave region."

The y-variation of the fundamental Floquet wave can be treated as a section of transmission line with length s as shown in Figure 2.5. The electric field of the dominant mode is a TM_y mode (non-zero E_y component), and hence the characteristic

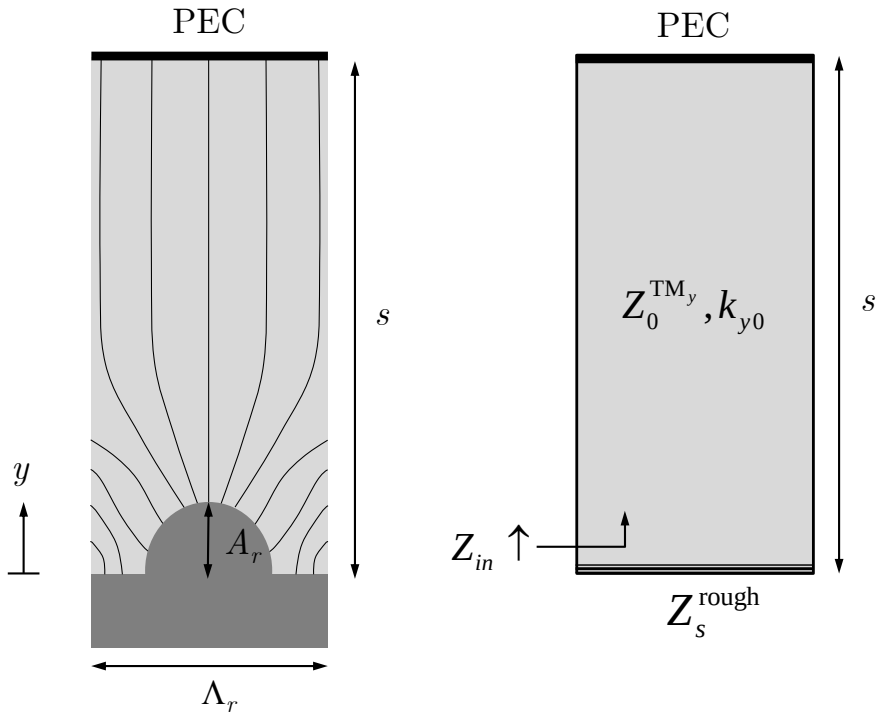

Figure 2.5. Transverse-resonant equivalent circuit used to compute the equivalent rough surface impedance. The y-variation of the fields is accounted for by a transmission line with $Z_0^{\mathrm{TM}_y}$ and k_{y0}.

impedance of this transmission line is the same as the TM_y wave impedance. In the TRT analysis, the rough surface impedance is the negative of the input impedance looking up from the plane that coincides with the base of the roughness. It is therefore given as

$$Z_s^{\mathrm{rough}} = R_s^{\mathrm{rough}} + jX_s^{\mathrm{rough}} = -jZ_0^{\mathrm{TM}_y} \tan(k_{y0}s), \tag{2.3}$$

where $k_{y0} = \sqrt{k^2 - k_{z0}^2}$ and $Z_0^{\mathrm{TM}_y} = k_{y0}/(\omega\epsilon)$. k_{z0} is the extracted 0^{th}-order Floquet wavenumber.

It should be noted that the distance s from the rough surface can be much smaller than the actual substrate thickness of the actual stripline, due to the evanescent behavior of the higher-order Floquet waves. This small s helps reduce the simulation domain dramatically. The minimum height of s can be calculated by limiting the

magnitude of the first-order Floquet wave to a specific low threshold, e.g., e^{-16}, after a y-directed round-trip, which gives

$$e^{-2jk_{y1}(s-A_r)} \leq e^{-16}, \tag{2.4}$$

where $k_{y1} = \sqrt{k^2 - (2\pi/\Lambda_r)^2} \approx -j2\pi/\Lambda_r$, so that

$$s \geq \frac{4\Lambda_r}{\pi} + A_r. \tag{2.5}$$

2.2.3 Fundamental Wavenumber k_{z0} Extraction

2.2.3.1 A Periodic Cavity

With proper periodic boundary conditions enforced, a periodic cavity can be used to compute the wavenumber k_{z0} of the 0^{th}-order Floquet mode. Figure 2.6 shows the structure of such a cavity.

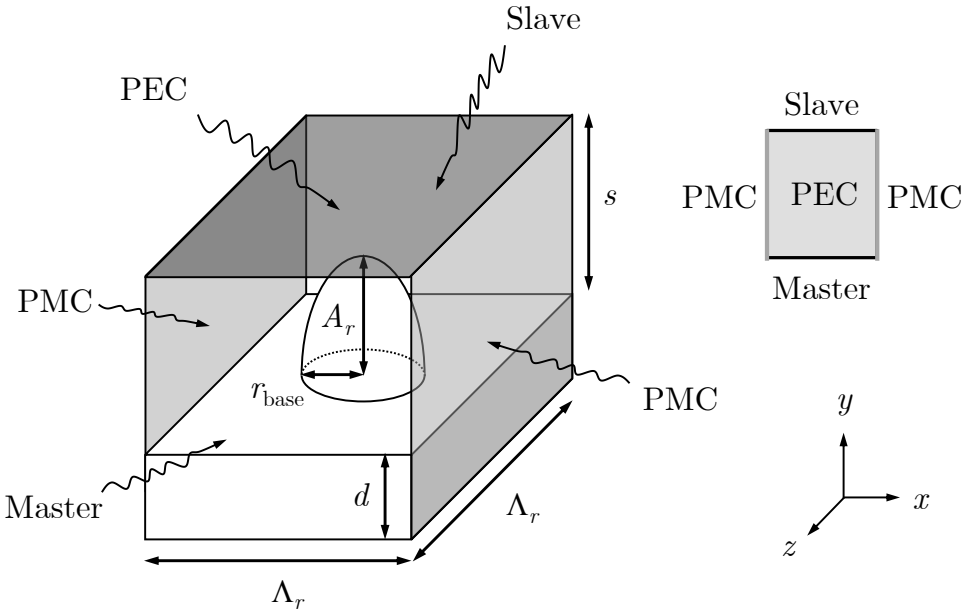

Figure 2.6. A periodic cavity used to extract the wavenumber k_{z0} with a top view showing the boundary condition assignments. The z-directed periodicity is accounted for by $\mathbf{E}_{\text{slave}} = \mathbf{E}_{\text{master}} e^{-j\beta\Lambda_r}$.

The bottom wall of the cavity is taken as one unit-cell of the periodically roughened conductor surface, with one hemispheroid copper ball residing on a copper slab. The top wall of the cavity is made from PEC. The side walls are made from perfect magnetic conductors (PMC), providing images of this single unit cell to create an infinite periodic structure along the x-axis. The front wall is assigned as a master boundary condition, and the rear wall is assigned as a slave boundary condition. The fields on the master and slave walls satisfy the periodic relation $\mathbf{E}_{\text{slave}} = \mathbf{E}_{\text{master}} e^{-j\beta\Lambda_x}$, with β as a *real* number and a given priori. The complex wavenumber is then given by $k_{z0} = \beta - j\alpha$, where α is the unknown attenuation constant.

This structure is also referred to as a transmission line resonator [5]. The quality factor Q of this resonator is given by $Q = \beta/(2\alpha)$. Therefore, at the resonant frequency $f = f' + jf''$, the wavenumber k_{z0} can be calculated as

$$k_z = \beta\left(1 - j\frac{1}{2Q}\right), \tag{2.6}$$

where the numerical value of f and Q can be obtained using a eigenmode solver. In theory, the periodic cavity has an infinite number of eigenmodes. The 0^{th}-order Floquet mode should be the one having the smallest f'.

2.2.3.2 A Long Waveguide

Practically speaking, it is also possible to use a long waveguide structure with appropriate boundaries to "brute force" the infinite periodic structure. Figure 2.7 shows the geometry of such a waveguide.

The waveguide has the same structure and boundary condition assignments as the periodic cavity, except it has no periodic boundary conditions (master and slave boundary conditions). Being a finite structure, the reflection due to the aperiodic-periodic-transition is inevitable. Therefore, instead of having only one unit-cell modeled as in the periodic cavity structure, there are n unit-cells along the z-axis in

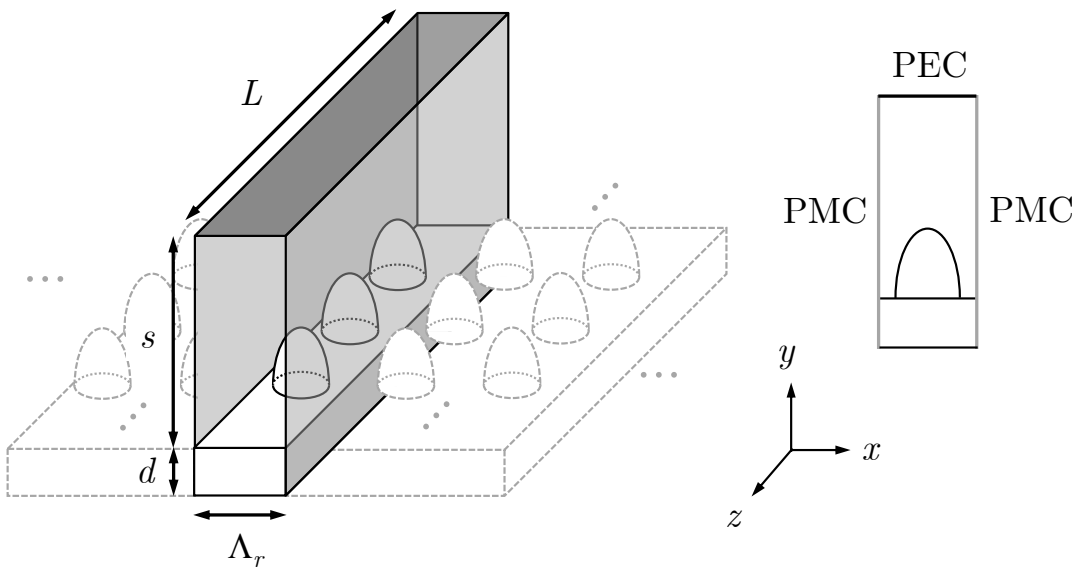

Figure 2.7. A waveguide structure used to extract the wavenumber k_{z0} with a side view showing the boundary condition assignments. There are n unit-cells in the z-direction.

the waveguide, and the length of the waveguide is $L = n\Lambda_r$. When n gets large, e.g., $n = 10$, so that the reflection due to the aperiodic-structure discontinuity is negligible, the fields inside this finite-length waveguide can be used to approximate those in an infinite periodic waveguide.

This long waveguide is then excited using two rectangular waveguide ports on the front (Port 1) and rear (Port 2) walls. We can extract the 0^{th}-order Floquet wavenumber k_{z0} by performing a full-wave simulation on this waveguide and evaluating the scattering parameters at these ports. If Port 2 is short-circuited (rear wall made of PEC), the reflection coefficient at Port 1 will be -1 (from the short circuit at Port 2) multiplied by a round-trip propagation factor $\exp(-jk_{z0}2L)$ that accounts for the length L. Indeed, this is equivalent to a waveguide having length of $2L$. The wavenumber can be calculated from the reflection coefficient (S_{11} parameter) as

$$k_{z0} = j\frac{\ln(-S_{11})}{2L}. \tag{2.7}$$

It should be noted that the placement of the PEC and PMC walls ensures a quasi-TEM mode in the waveguide that has E_y and H_x components, and this is the mode that is incident from Port 1. Also, several Floquet modes propagate in the waveguide and the reflection coefficient S_{11} actually accounts for all these modes. In order to extract the 0^{th}-order Floquet mode, the waveguide should be tall enough so that all the other modes have, compared to the fundamental Floquet mode, negligible contribution to the total fields. This height s is usually larger than the minimum value characterized by Eq. (2.5).

2.2.3.3 Rough Surface Impedance Comparisons

Figure 2.8 shows the equivalent surface resistance $R_s^{\text{rough}} = \Re\{Z_s^{\text{rough}}\}$ for various copper foils, namely HVLP, VLP and STD. Their roughness parameters are given in Table 2.2. As the roughness amplitude increases, the surface resistance also increases, making the foil more lossy.

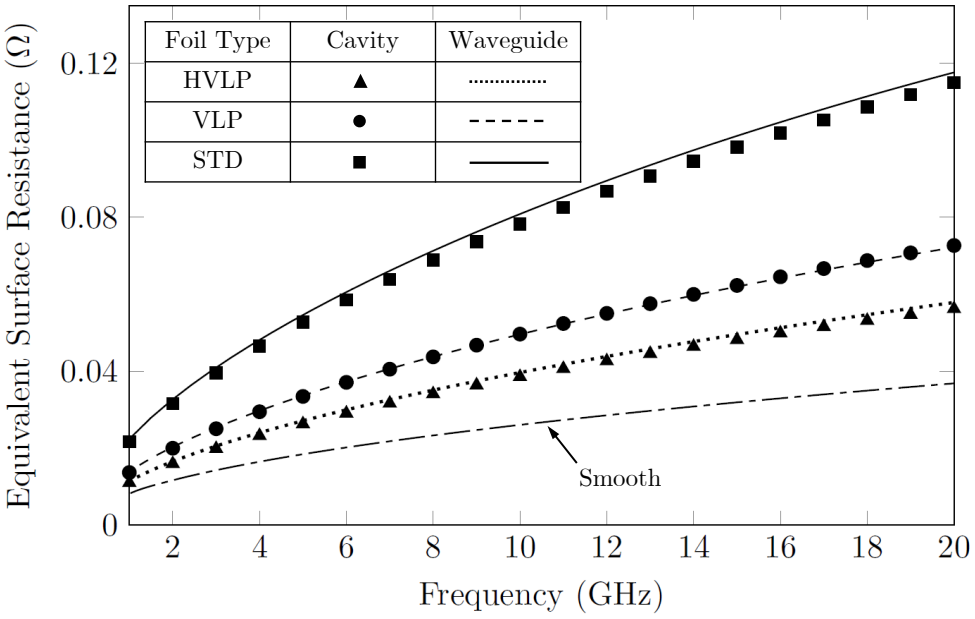

Figure 2.8. Equivalent surface resistance for various copper foils with different surface roughness using two structures, namely a periodic cavity and a long waveguide.

In Figure 2.8, the numerical results using the periodic cavity and the long waveguide

structure agree well with each other. However, the computational cost of the latter approach is theoretically more than that of the former one. The cavity has only one unit cell of the periodic structure, yet the waveguide has n unit-cells along z-direction. Also, the height s of the waveguide is chosen larger than that of the cavity to reduce (a) the reflection arising from the aperiodic-periodic-discontinuity and (b) the propagation of the higher-order Floquet modes. Therefore, the periodic cavity model is preferred over the long waveguide model as long as an eigenmode solver is available.

2.3 Per-Unit-Length Parameters Modification

From a macroscopic point of view, the real-world stripline structure with a rough surface is the same as an ideal lossless stripline structure with smooth conductors, except that the conductor surface is replaced by the equivalent rough surface impedance. Therefore, the fields for the rough-surface stripline can be obtained by solving the ideal structure first and then modifying the results corresponding to the surface impedance boundary conditions.

2.3.1 Per-Unit-Length Parameters RLGC — Ideal Model

A multi-conductor transmission line (MTL) refers to a system containing $(n+1)$ conductors with the extra one being the return path of the n conductors. Figure 2.9 shows a multi-conductor stripline transmission line structure, where n strip conductors run between two infinite ground planes in the z-direction and are separated from the grounds by dielectric substrate layers. For convenience, the ground planes are labeled as the 0^{th}-conductor. The port voltage V_i is defined as the potential difference from the ground to the i^{th}-conductor. The port current I_i is defined as the current flowing into the i^{th}-conductor $(1 \leq i \leq n)$.

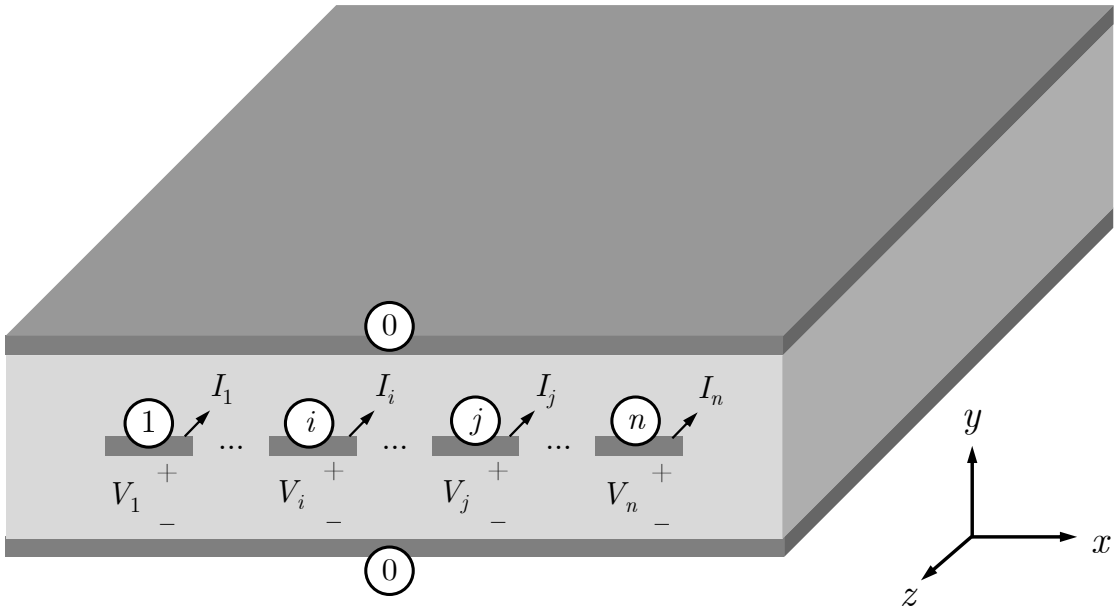

Figure 2.9. Definition of port voltage and current for a multi-conductor stripline transmission line structure. The ground planes are labeled as the 0^{th}-conductor.

The classical Telegraphers equations for a MTL, using matrix notations, is

$$\begin{cases} \frac{\partial}{\partial z}[V](z,t) = -[R][I](z,t) - [L]\frac{\partial}{\partial t}[I](z,t), \\ \frac{\partial}{\partial z}[I](z,t) = -[G][V](z,t) - [C]\frac{\partial}{\partial t}[V](z,t), \end{cases} \tag{2.8}$$

where $[V_n]$ and $[I_n]$ are terminal voltages and terminal currents, respectively. Note that the indices start from 1, because the 0^{th}-conductor is the reference conductor and $I_0(z,t) = -\sum_{i=1}^{n} I_n(z,t)$.

The $[R]$, $[L]$, $[G]$ and $[C]$ are the per-unit-length (PUL) parameter matrices of size $(n \times n)$. The equivalent circuit within an infinitesimal distance Δz is shown in Figure 2.10. The same equivalent circuit for a single-ended transmission line is shown in Figure 2.11. The parameters can be derived using the integral form of Maxwell equations [6], from which the propagation mode for a stripline transmission line can be solved. Details of the propagation mode computation are discussed in Appendix B.

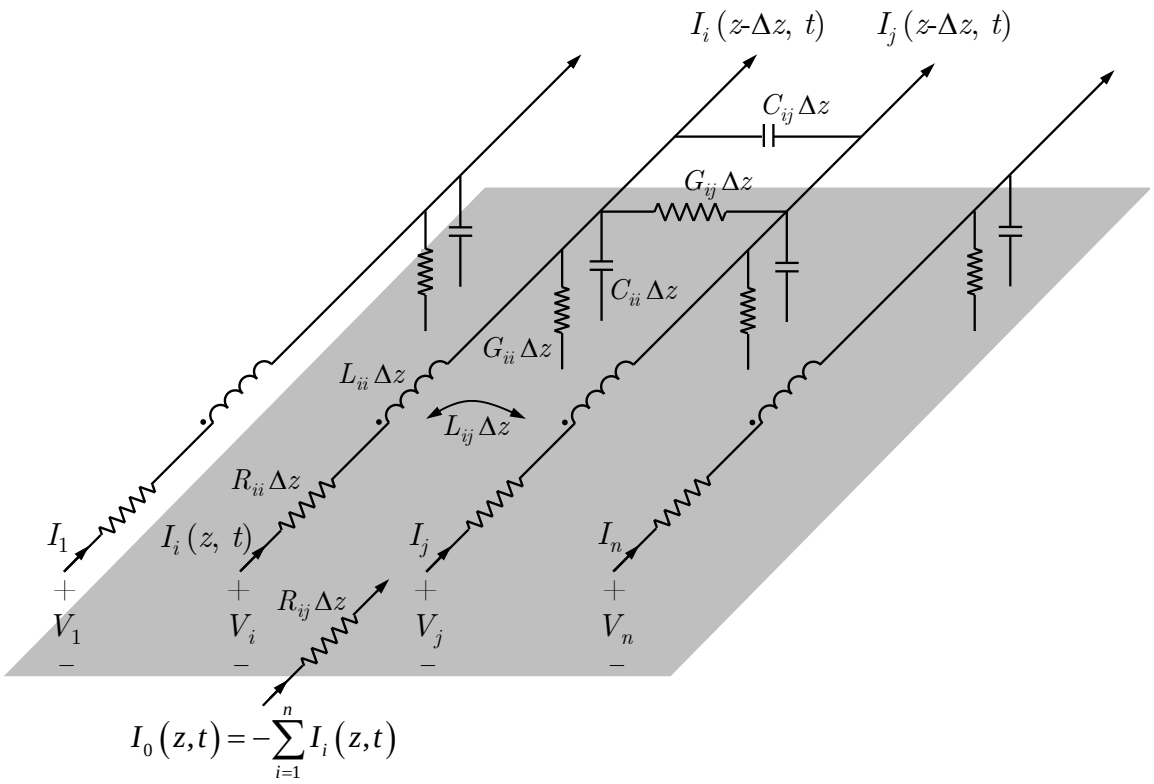

Figure 2.10. The per-unit-length equivalent circuit model for a $(n+1)$ conductor stripline transmission line system. It is made of the per-unit-length $RLGC$ matrix parameters.

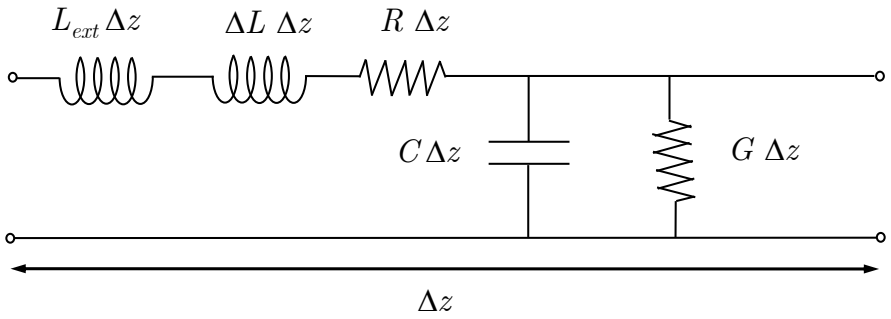

Figure 2.11. The per-unit-length equivalent circuit model for single-ended transmission line.

2.3.1.1 Per-Unit-Length Parameters LGC

The capacitance $[C]$ matrix accounts for the electric energy stored in the substrate, and is obtained by applying static potentials (voltages) and solving for the charges on each conductor as

$$C_{ij} = \left.\frac{Q_i}{V_j}\right|_{V_{k\neq j}=0}, \tag{2.9}$$

where Q_i is the total surface charge on the ith conductor when the jth conductor has a voltage of V_j and all the other conductors are short-circuited. Referring to Figure B.2, the total charge on the ith conductor is obtained using $Q_i = \oint_C \rho_s dl$, where ρ_s is from a static MoM solution as shown in Appendix B.

The inductance $[L]$ matrix accounts for the magnetic energy stored in the substrate and can be found from capacitance matrix as

$$[L] = \mu_0 \mu_r \epsilon_0 [C_0]^{-1}, \tag{2.10}$$

where $[C_0]$ is the capacitance matrix using an air substrate.

The conductance $[G]$ matrix accounts for the loss from the displacement current in the substrate. It can be computed from capacitance matrix $[C]$ parameter as

$$[G] = \omega \tan\delta [C]. \tag{2.11}$$

2.3.1.2 Per-Unit-Length Parameters R and ΔL

The resistance $[R]$ matrix accounts for the conductor loss and is directly calculated from the Telegraphers equation as

$$R_{ij} = -\Re\left[\frac{\partial V_i/\partial z}{I_j}\right]\Bigg|_{I_{k\neq j}=0}. \tag{2.12}$$

Since only the power dissipation is considered, the real part of the voltage loop integral shown in Figure 2.12 should give zero (the reactive magnetic flux though is not zero).

In Figure 2.12, currents are only driven into the j^{th} conductor, and all the other conductors (excluding the ground 0^{th}-conductor) have zero current flow. The same amount of currents flow out through the 0th conductor, but with opposite direction, that is, $I_0(z) = -I_j(z)$.

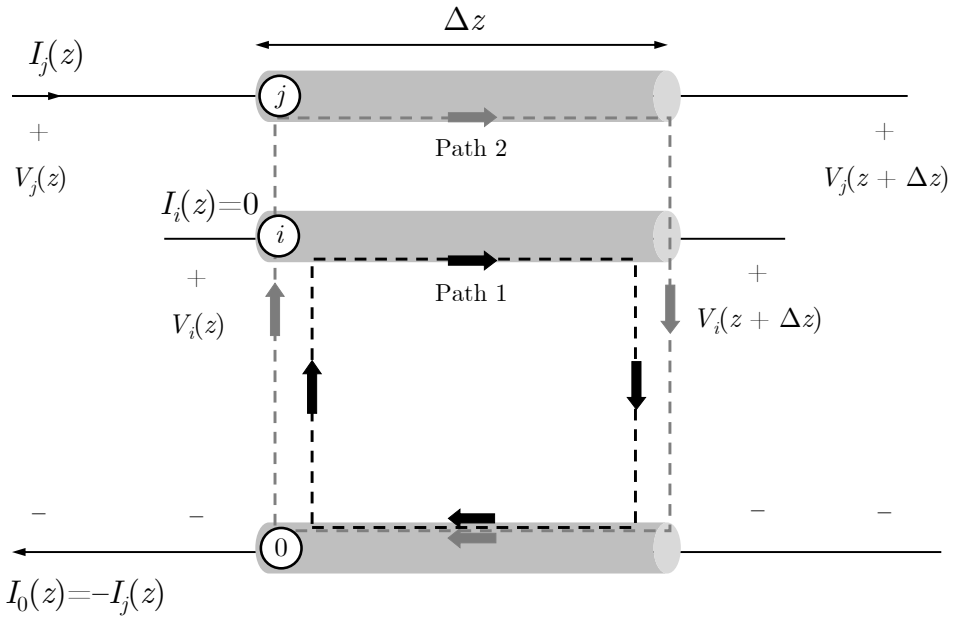

Figure 2.12. The integration path used to find the per-unit-length resistance from the Telegrapher's equation. The system is driven such that the only non-zero excitation is I_j.

Referring to Figure 2.12, using the loop integral in the darker color (path 1) to compute R_{ij}, since there are no conduction loss along the ith conductor, R_{ij} is simply given as the ground resistance R_{gnd}. Using the loop integral in the lighter color (path 2) to compute R_{jj} and the conduction loss is from both the jth conductor (R_{strip}) and the ground. Hence, the expression for the elements in the PUL resistance $[R]$

matrix is

$$R_{ij} = \begin{cases} R_{\text{strip}} + R_{\text{gnd}}, & i = j, \\ R_{\text{gnd}}, & i \neq j. \end{cases} \tag{2.13}$$

The resistance for the strip R_{strip} and the ground planes R_{gnd} can be computed from the perturbation formula. Using Figure 2.13, based on the small perturbation theory (SPT), the complex power entering the conductor PUL is

$$P = \frac{1}{2} \oint_C Z_s |J_{sz}|^2 dl, \tag{2.14}$$

where C is conductor surface boundaries. Z_s is the surface impedance of the conductor, defined by the ratio of the tangential E and H components. J_{sz} is the surface current density on the conductors and can be computed from the surface charge density ρ_s as

$$J_{sz}\hat{\mathbf{z}} = \hat{\mathbf{n}} \times \mathbf{H}_t = \frac{1}{\eta}\hat{\mathbf{n}} \times \hat{\mathbf{z}} \times \mathbf{E}_t = \frac{\rho_s}{\eta\epsilon}\hat{\mathbf{z}}. \tag{2.15}$$

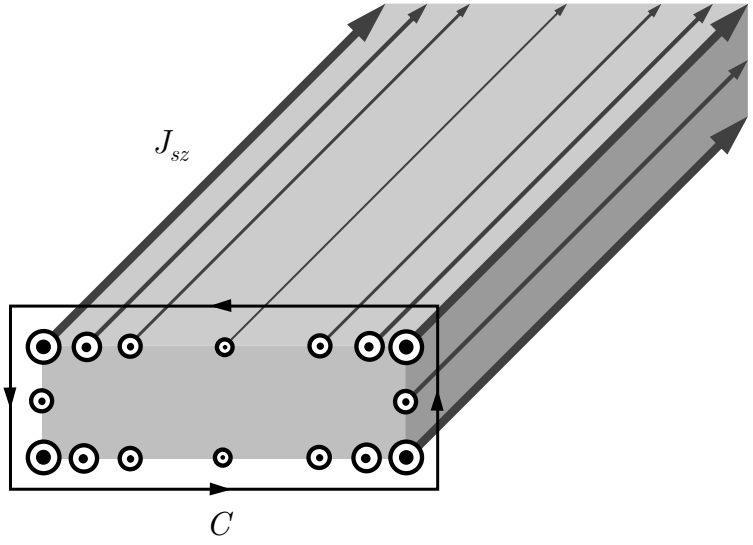

Figure 2.13. Surface current J_{sz} on the strip and the integration path C along the strip boundaries.

The power dissipated and trapped to the conductor region within Δz from the equivalent $RLGC$ circuit (see Figure 2.11) is

$$\begin{aligned} P &= \frac{1}{2}(R + j\omega\Delta L)|I|^2 \\ &= \frac{1}{2}(R + j\omega\Delta L)\left|\oint_C J_{sz} dl\right|^2, \end{aligned} \tag{2.16}$$

where ΔL is the internal inductance that accounts for the stored magnetic energy *inside* the conductors. The total inductance parameter L is then the sum of the internal inductance and the external inductance calculated using Eq. (2.10), and that is $L = L_{\text{ext}} + \Delta L$.

Equating Eq. (2.14) and Eq. (2.16) and using the relation between J_{sz} and ρ_s gives

$$R + j\omega\Delta L = \frac{\oint_C Z_s|\rho_s|^2 dl}{\left|\oint_C \rho_s dl\right|^2}. \tag{2.17}$$

Strictly speaking, Z_s is variant along the integral path C. However, when the conductivity σ of the metal is sufficiently high that the electromagnetic wave penetrates only a negligible distance, the value of Z_s becomes weakly dependent on location, and the conductor can be assumed to have an infinite extent. Based on this assumption, the surface impedance can be computed using the classical skin-depth formula,

$$Z_s^0 = \sqrt{\frac{\pi f \mu}{\sigma}}(1 + j). \tag{2.18}$$

The superscript "0" denotes the conductor is assumed to be smooth and infinite and the value is obtained using the normal skin-depth formula.

2.3.2 Per-Unit-Length Parameters Modification

As can be seen from the Figure 2.3, half of the conductor surfaces are rough and the rest are smooth. Macroscopically, J_{sz} is evenly distributed on the rougher and the smoother surfaces of the conductors. Based on this, we can define an effective surface impedance as

$$Z_s^{\text{eff}} = 0.5 Z_s^{\text{rough}} + 0.5 Z_s^0, \tag{2.19}$$

where Z_s^0 is the surface impedance of a smooth conductor as given by Eq. (2.18). Z_s^{rough} is the equivalent rough surface impedance given by Eq. (2.3).

Plugging the value of Z_s^{eff} into Eq. (2.17) and then we can obtain the modified R and ΔL (the internal inductance). Table 2.3 lists the values of internal inductance ΔL for stripline with various copper foils, as well as the internal inductance ΔL_0 for a stripline with a smooth conductor. The external inductance L_{ext} of the stripline (accounting for the magnetic flux external to the conductor, i.e., in the substrate) is also shown, which is calculated from the static field solver. The total inductance $L = L_{\text{ext}} + \Delta L$) and the ratio of internal inductance to external inductance is also included. It should be noticed that the internal inductance for the rough surface is much larger than that for the smooth surface, thus creating a noticeable alteration in the phase velocity.

Table 2.3. Comparison of inductances

Foil type	ΔL[1]	ΔL_0[1]	$\Delta L/\Delta L_0$	L_{ext}[1,2]	$\Delta L/L_{\text{ext}}$
STD	13.13	0.71	18.40	274.91	4.78%
VLP	5.51	0.68	8.14	272.33	2.02%
HVLP	3.33	0.72	4.28	293.38	1.14%

[1] The inductance units are nH/m.

[2] L_{ext} is computed by solving the static potential integral equation using MoM (See Appendix B). The values of L_{ext} are slightly different because the dimensions of the three striplines are different.

The frequency dependency of the G and C parameters are automatically accounted for using the real-world substrate dielectric properties ϵ_r and $\tan\delta$. The R and ΔL parameters will lose accuracy at low frequency, since the conductors can no longer be characterized with a surface impedance. For the internal inductance ΔL at low frequency, the method discussed in [55] is applied to calculate the value at DC. The surface roughness has negligible effects at DC and is simply ignored, so the R parameter at low frequency is taken as the DC value of a stripline with smooth surfaces. At DC the resistance comes only from the strip conductor (since the infinitely wide ground planes have zero resistance at DC), and the resistance per unit length is given by the usual DC wire formula ($R = 1/(\sigma A)$, where A is the cross-sectional area of the strip conductor). A simple linear interpolation in frequency is used to connect the DC values of R and ΔL with the values at 73 MHz [56], in order to determine the values at an in-between frequency. For frequencies over 73 MHz, the high-frequency values are used.

The frequency-dependent transmission line per-unit-length $RLGC$ parameters are used to calculate the real-valued total attenuation constant α_T as given by

$$\alpha_T + j\beta = \sqrt{(R + j\omega L)(G + j\omega C)}, \tag{2.20}$$

and they can be also used to compute the effective dielectric constant ϵ_r^{eff} as given by

$$\epsilon_r^{\text{eff}} = \left(\frac{\beta}{k_0}\right)^2. \tag{2.21}$$

The numerical value of α_T and ϵ_r^{eff} calculated from the $RLGC$ parameters extracted using the approach presented in this chapter are referred to as the "proposed method" in the results.

2.4 Numerical Results and Discussions

In order to validate the proposed approach, comparisons have been made using a numerical full-wave simulation as well as using several measurements. In comparison with the full-wave simulation, a 2-D roughness structure is chosen with no z-variation, since 3-D roughness profile is not calculable. In comparison with measurements, striplines are laminated with practical copper foils having 3-D roughness.

2.4.1 Comparison with Full-Wave Simulations

In order to validate the rough surface impedance, we carried out full-wave simulations on a pair of edge-coupled inhomogeneous striplines, where the dielectric constant for the "prepreg" is 3.3 and for the "core" is 3.5. The detailed dimensions and associated electromagnetic parameters are given in Figure 2.14. The differential characteristic impedance Z_0^{diff} is 100 Ohms.

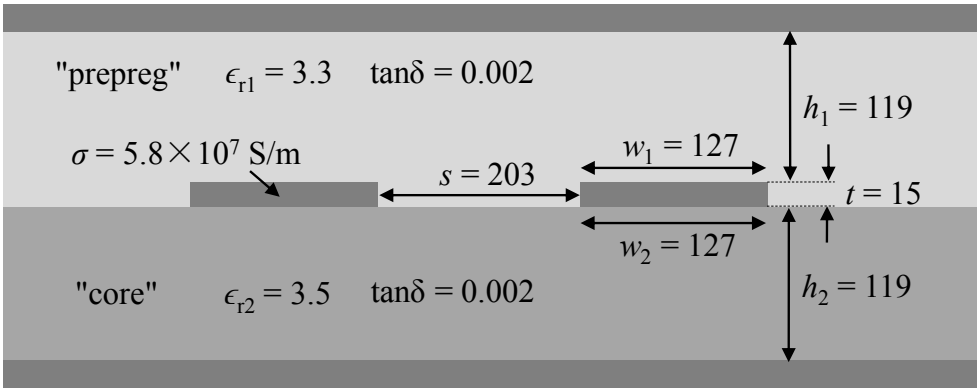

Figure 2.14. Cross-sectional dimensions and substrate dielectric properties for a pair of edge-coupled striplines. The length unit used here is μm.

The entire cross-sectional plane is modeled in Ansys HFSS 15.0 for the full-wave calculation, including the fine texture of the conductor surface roughness. The numerical results will be compared against that using the proposed approach. Due to the limitation of mesh density, we assumed that the ground planes are perfect conductors and besides that, we performed a port solution (a 2-D solution) in HFSS. And to be consistent with the chosen solution type, we used a 2-D "cylinder-like"

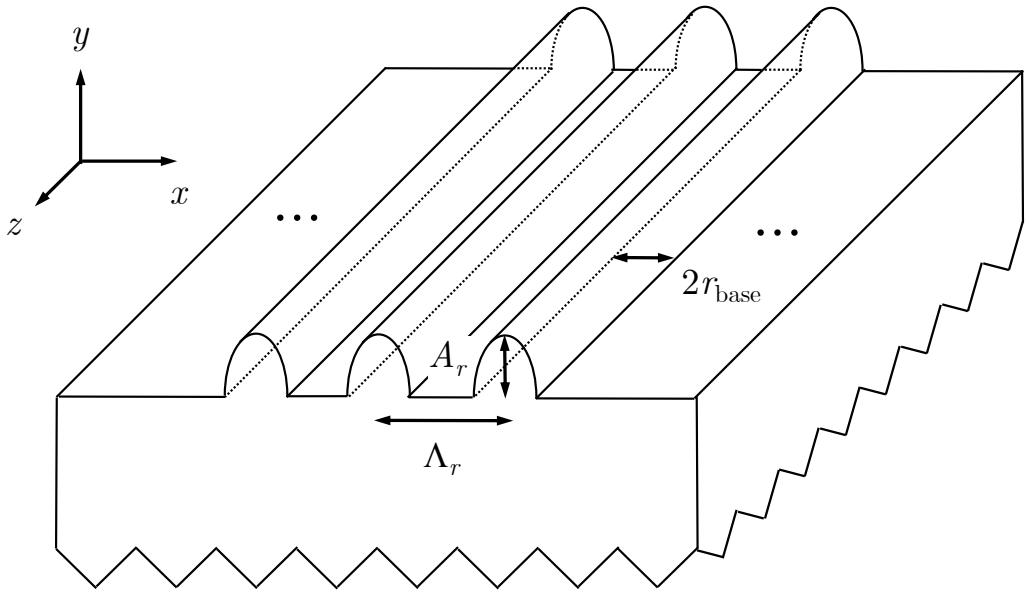

Figure 2.15. The artificial "cylinder-like" roughness profile used in the HFSS port-solution-type simulation.

roughness (see Figure 2.15); that is, the periodic cylinders are aligned along the z-axis and periodic only along the x-axis. The current therefore is flowing parallel to the grooves. Although this is not a realistic roughness, it serves as a good validation of the proposed technique for treating the surface roughness problem. The roughness parameters are chosen to be $\Lambda_r = 1\ \mu m$, $A_r = 1\ \mu m$, and $r_{\text{base}} = 0.25\ \mu m$.

In the full-wave simulation, a total number of 128 periodic elements are modeled on the surface of the trace, and within each period, the hemispherical cylinder representing the roughness is meshed. There are overall 81797 tetrahedrons in the mesh and the memory consumption for the "matrix assembly" is 4.25 GB. The average mesh size inside the conductor is 1.21 μm and the total CPU time to run this simulation is 34 min/frequency point. These meshing data for the 2D solution actually predict that if we want to run a 3D simulation for the same stripline, the total required memory will become computational prohibitive. The memory and time consumption for a 3D simulation will become even much more if the ground planes are also rough conductors. In the proposed approach, on the other hand, the memory requirement

for the surface impedance calculation using the periodic cavity is 33.7 MB while the CPU time is only 2 seconds per frequency.

In the numerical test, we used two types of trace profiles: a matte (roughness) on one side, and a matte on both sides of the trace. For the single-sided matte profile, the effective surface impedance is the average of the smooth and rough surface impedance as indicated by (Eq. (2.19)). For the double-sided matte case, it is simply the rough surface impedance as given by (Eq. (2.3)).

Figure 2.16 shows the comparison of the attenuation constants, where the propagation constant γ at the port from HFSS provides the full-wave result. The proposed method provides consistent results with HFSS full-wave simulation and has the less than 0.2 Np/m error for the attenuation constant.

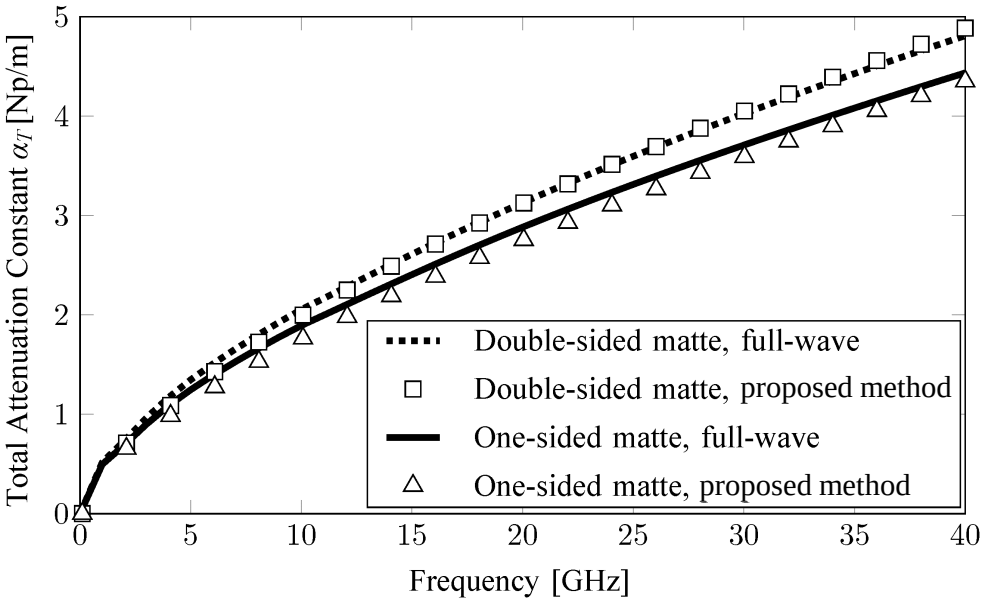

Figure 2.16. The total attenuation constant α_T comparison of the stripline with two trace profiles, full-wave simulation vs. proposed method.

2.4.2 Comparison with Measurements

Three set of test vehicles are manufactured to validate the proposed method. They have almost identical dielectric properties and similar cross-sectional geometries, with different copper foils. The cross-sectional SEM picture for the PCB test vehicles is

given in Figure 2.3, and the geometrical data is given in Table 2.1. The length L of all the traces is 39.14 cm (15.41 inches).

Appendix C summarizes the method used to extract the substrate dielectric properties in the presence of the conductor surface roughness. The dielectric constant ϵ_r, or Dk, is extracted using the traveling wave transmission-line method from the S-parameters of the smoothest foil (HVLP). The frequency dependence of the dissipation factor $\tan\delta$, or Df, is extracted using the differential extrapolation method [51]. The extracted dielectric properties of the substrate material are shown in Figure C.2.

Note that the "Dk" value appearing in Figure C.2 is directly calculated from the phase-delay information of the PCBs with HVLP foil. It is actually an effective dielectric constant ϵ_r^{eff} for this specific stripline laminated with HVLP foil. It averages over the substrate cross section and is "contaminated" by the effects of surface roughness for the HVLP foil. Hence the measured value is slightly greater than the true ϵ_r value for the PCB substrate.

For maximum accuracy we need to pre-process the measured dielectric constant Dk before using this to calculate the C parameter. This pre-processing step is referred to as a "cleaning" of the Dk data. It removes the HVLP roughness effect, which changes the phase velocity caused by the imaginary part of the effective surface impedance Z_s^{eff} of the HVLP foil. Hence, the "cleaned" Dk value is obtained by matching the calculated ϵ_r^{eff} (obtained from the proposed approach applied to the stripline that was used in the HVLP measurements of [51], using the calculated surface impedance of the HVLP foil) to the measured Dk value data (identical to the [51]-extracted Dk). This "cleaned" Dk can then be used for all of the foils. Figure 2.17 shows the extracted Dk and Df data, both before and after the "cleaning" process given.

Figure 2.18 and Figure 2.19 show the roughness effects on the signal losses and dispersion, respectively. The PCB with STD foil is used as an example. The "cleaned"

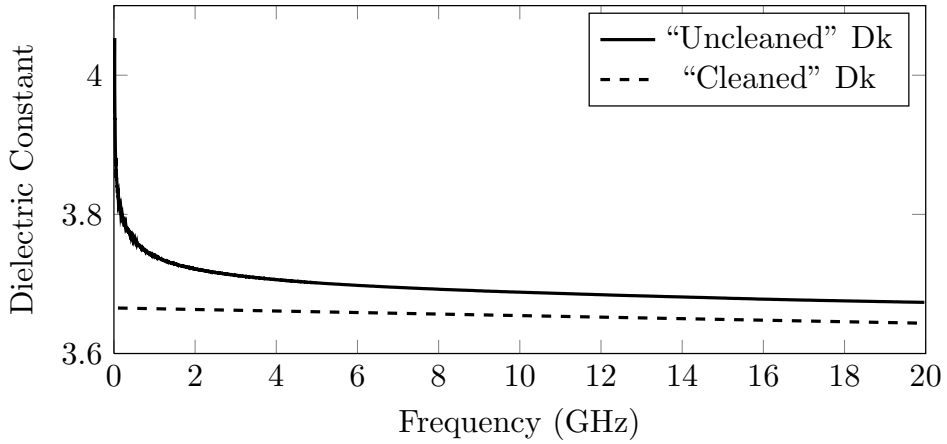

(a) Dielectric constant ϵ_r, or Dk. The solid line is obtained using the traveling wave transmission-line method from the S-parameters of the smoothest foil (HVLP). The dashed line is the "cleaned" data by subtracting the surface roughness effects of a HVLP foil.

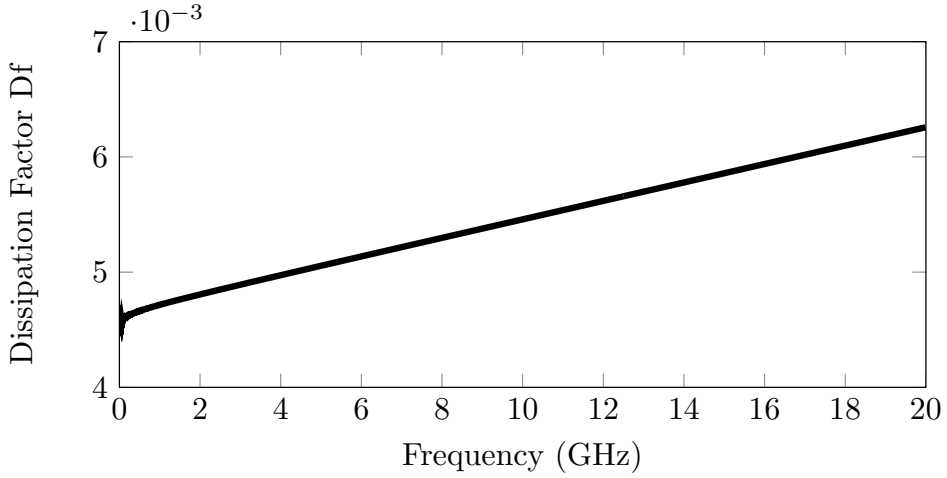

(b) Dissipation factor $\tan\delta$, or Df, extracted using the differential extrapolation method [51].

Figure 2.17. Dielectric properties of the PCB test board substrate material.

Dk, along with α_T corresponding to smooth conductors, are added for comparison. As expected, the ϵ_r^{eff} values obtained from the proposed method agree well with the values that are directly measured for the STD foil since it accounts for both the intrinsic substrate dielectric properties and the roughness of the STD foil.

It can be observed that the existence of the conductor surface roughness increases the effective dielectric constant, which is consistent with the argument in [50]. For a stripline built with rough foils like STD ($R_z = 8.41$ μm), the roughness increased ϵ_r^{eff}

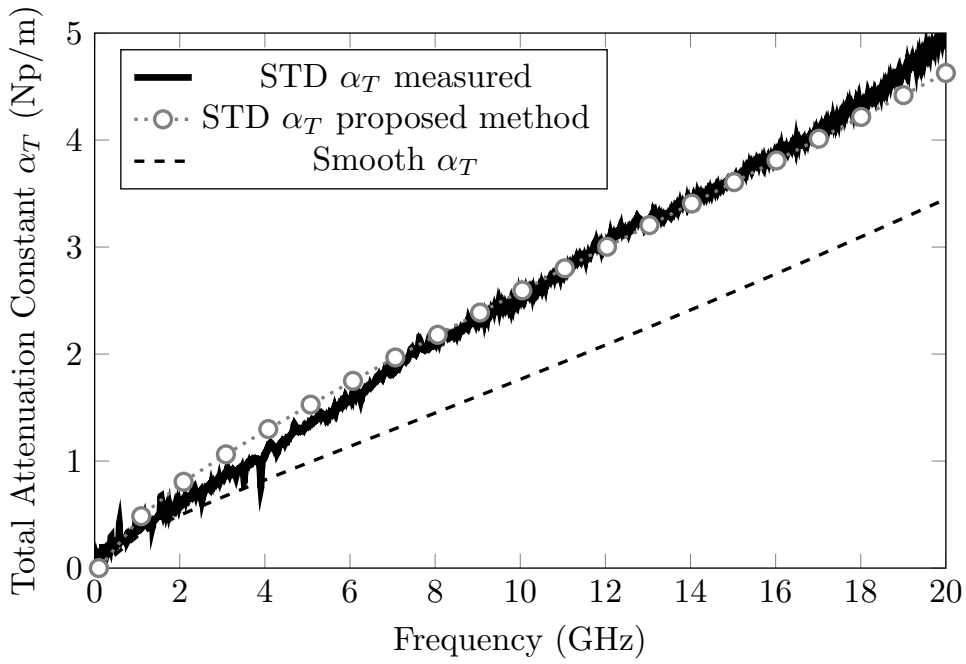

Figure 2.18. The total attenuation constant α_T for a single-ended stripline with STD foil.

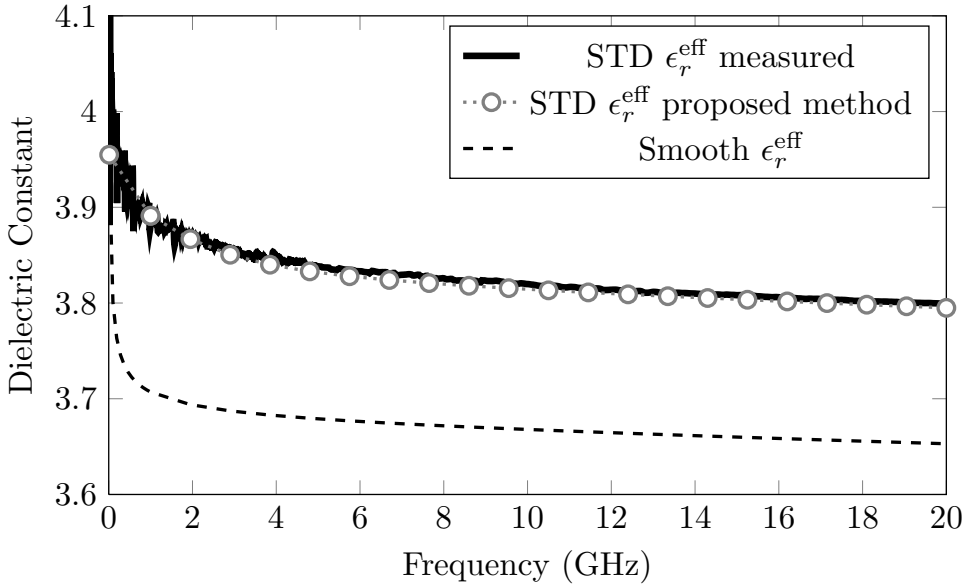

Figure 2.19. The effective dielectric constant ϵ_r^{eff} for a stripline with STD foil.

by about 5% compared to the cleaned substrate Dk. The cleaned Dk value is almost frequency independent, unlike the value taken directly from measurements with the STD foil. The roughness also increased α_T by 0.33 dB/in (1.5 Np/m), compared to

that of a stripline with smooth conductors.

Figure 2.20 illustrates the comparison of the calculated attenuation constant with measurement. The measured attenuation constant is extracted from the insertion loss using $ABCD$ parameters. For these single-ended striplines, the calculated attenuation constant agrees with measurement to within 0.2 Np/m.

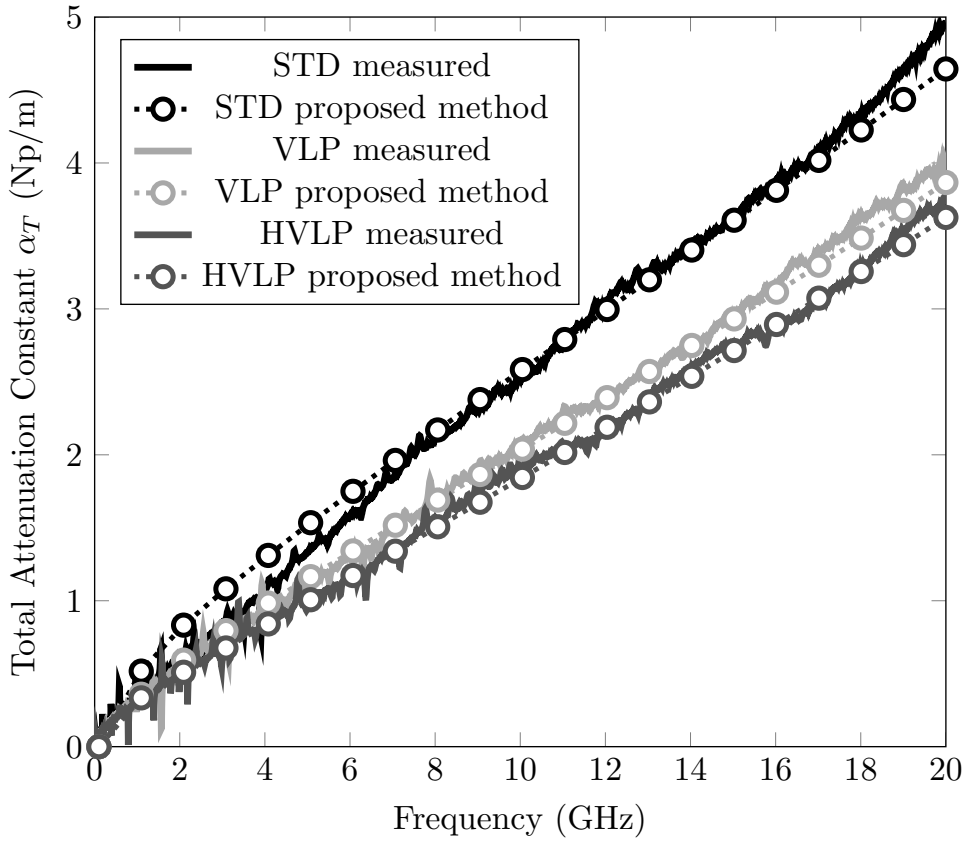

Figure 2.20. Total attenuation constant α_T. Proposed method vs. measurement.

2.5 Conclusions

In this chapter, a numerical method for a periodically roughened stripline transmission line was given. The conductor surface roughness effects on signal propagation, including signal attenuation and phase-delay, have been analyzed.

A periodic structure model was introduced to approximate the surface roughness, which in turn was represented in terms of an equivalent surface impedance due to the

size difference between the period and wavelength. Two models, a periodic cavity and a long waveguide that can simulate an infinite periodic roughened conductor surface, were proposed. A full-wave simulation was performed on these two specially-designed models built from the periodic structure, and the fundamental Floquet wavenumber was extracted to calculate the equivalent surface impedance for the rough surface.

The effective surface impedance, which accounts for both the rougher and the smoother sides of the conductors, was used to modify the per-unit-length transmission line parameters. Results have shown that as the amplitude of the conductor surface roughness increases, the conductor loss increases significantly, and the effective dielectric constant also increases noticeably.

Chapter 3

Modeling of Vias with Arbitrary-Shaped Antipads

Chapter 3 presents a semi-analytical model for densely-packed vias with arbitrarily-shaped antipad. Vias are widely used for vertical miniaturization and integration in multilayer printed circuit boards (PCBs) and packages [18]. A typical via consists of a conducting pin (barrel) running vertically through layers, with apertures (antipads) on each power/ground plate producing the isolation (see Figure 3.1). Each of the two ends of a via perpendicularly contacts the signal traces or the power/ground planes.

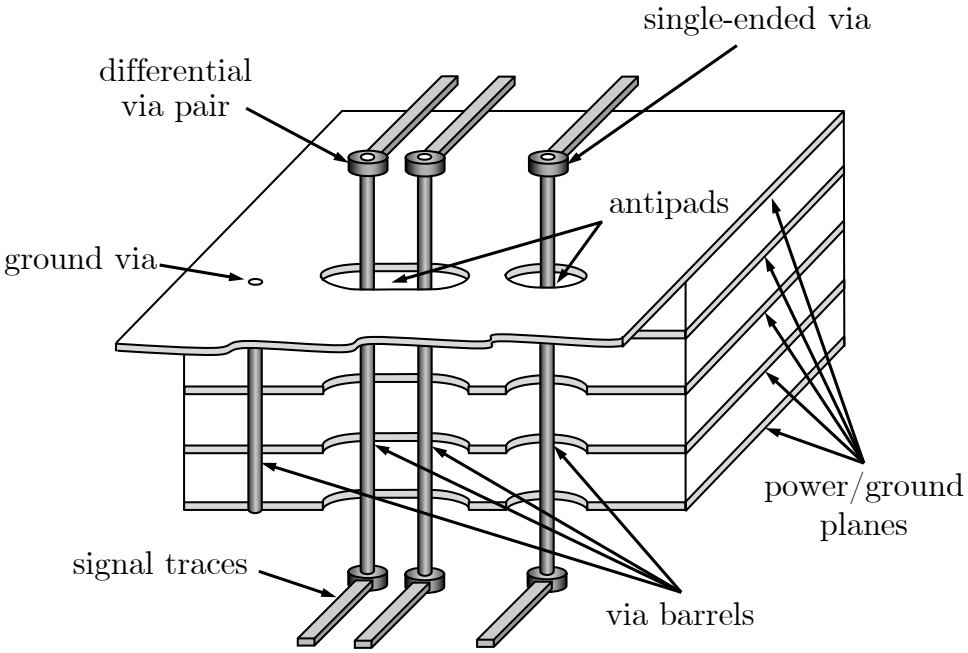

Figure 3.1. A vertical cut of a six-layer PCB board with vias connecting signal traces from the top to the bottom layer.

In practical design, the vias are placed in a periodic fashion to form a via array, some of which are signal vias and the rest are grounding vias. This type of design helps to reduce the crosstalk between vias by introducing closer return paths for the currents on the signal barrels. It should be noted that the proposed via model is able

to handle an arbitrary layout of vias, although a periodic arrangement is common.

We begin this chapter by a historical review of the existing models for via interconnects in Section 3.1. Section 3.2 introduces the methodology using reciprocity, where the port current formula is first derived. Next, the computation of the radiation from the testing frill that appears in the port current formulation is given is Section 3.3. The efficiency of the proposed algorithm is then discussed and a closed-form expression for the testing frill radiation is given in Section 3.4. In Section 3.5, numerical results are compared with those obtained using HFSS and the integral-equation approach. Section 3.6 gives conclusions for the proposed semi-analytical model for dense vias with arbitrarily-shaped antipads.

3.1 Introduction

In the past, a via discontinuity [see Figure 3.2(a)] has usually been modeled as a π-network circuit with lumped elements [see Figure 3.2(b)]. Quasi-static analyses were applied to extract these elements [21], [29]–[31], [57]–[59] However, the accuracy of this circuit model deteriorates as the frequency increases [60], since the via barrels and the antipads become good radiators as they excite the propagating parallel-plate modes. This unintentional radiation becomes more significant in the higher frequency region and generates serious electromagnetic interference (EMI) and gives rise to signal integrity (SI) issues [61]. The lumped-element circuit model is inadequate for analyzing these effects.

A hybrid-circuit model, also known as the "physical-based" model, was then developed to study the high-frequency radiation/coupling mechanism [22], where a frequency-dependent parallel-plate-impedance $Z_{\rm pp}$ replaces the inductance to capture the behavior of the parallel-plate modes (see Figure 3.2(c)). A methodology review is given in [62], [63]. A similar idea can be found in [64], [65]. A via-plate capacitance $C_{\rm via}$ extraction based on higher-order vertical modes was introduced in [19], [26], [36].

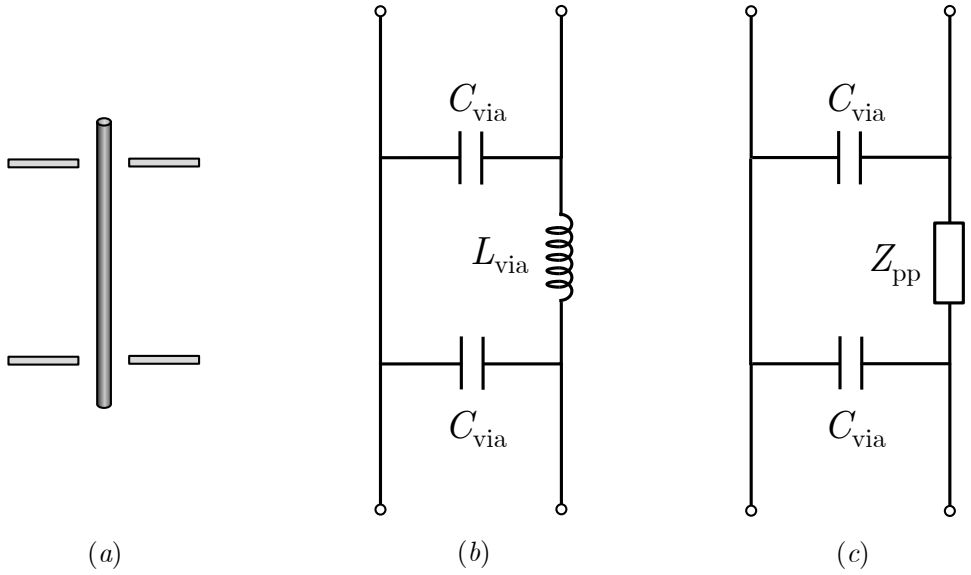

Figure 3.2. Existing models for a via discontinuity. The via traversing a pair of plates shown in (a) is modeled with the lumped-element circuit (b) and a "physical-based" hybrid-circuit (c).

Although this hybrid-circuit model does not consider the coupling of the antipad apertures and is thus less accurate for densely packed via structures, it is flexible enough to handle the edge reflection of finite-size parallel-plate pairs [66] and is convenient to use in both frequency and time domain analyses with friendly interfaces to SPICE-like solvers. Accuracy issues of this model are considered in [67], [68]. System-level applications can be found in [69], [70].

A rigorous scattering approach was also used to analyze the high-frequency effects for via structures [20], [27], [28], [34], [35], [38], [71]–[76]. A progress review of this category of methods can be found in [77]. In this set of approaches, the electric-field-integral-equation (EFIE) is enforced on the surfaces of the via barrels: the incident field from the antipad aperture radiation should cancel the scattered field from the barrels and thus the induced via currents are computed. Due to the complexity of the aperture radiation, many vertical and azimuthal modes are required for convergence, especially when an antipad is located close to the barrels.

In [78], we proposed a novel approach that takes advantage of reciprocity to bypass the antipad aperture radiation calculation, with preliminary results given. A reaction [79] is used to determine Y_{ij}, the element of the $[Y]$ matrix corresponding to ports i and j in the via layout as shown in Figure 3.3, where the short-circuit current at port i is "measured" using a unit-voltage magnetic ring frill at port i. The reaction between the antipad aperture source on port j and the testing frill on port i is equal to the negative of the current at the ring location on port i [80], which directly gives Y_{ij}. From reciprocity this reaction is equal to the field of the testing frill integrated over the aperture source on port j. Similar to the calculations in [34], [35], this can be reduced to a line integral containing the surface charge density ρ_s at the port j antipad.

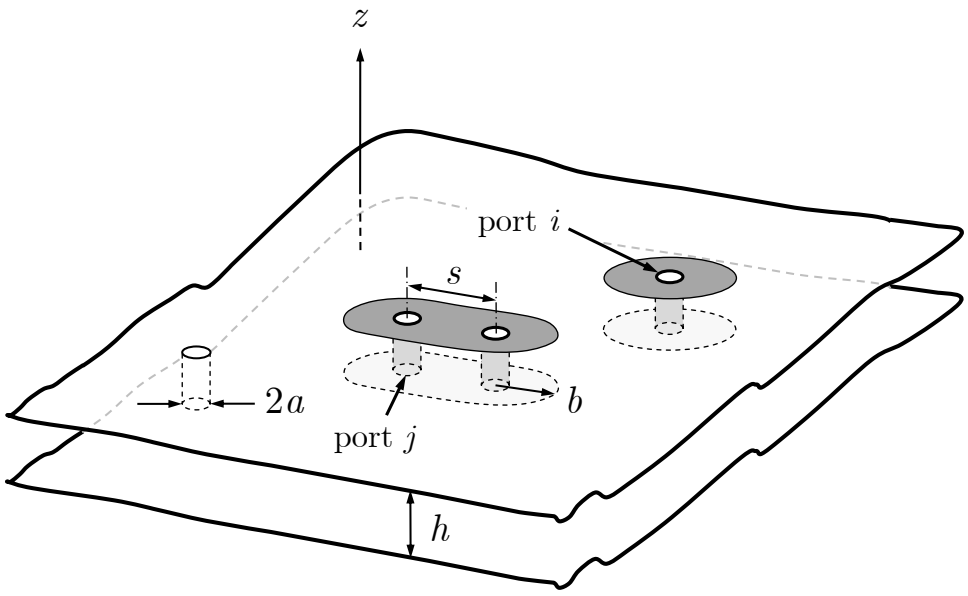

Figure 3.3. Multiple via structure. The configurations include differential/single-ended signal vias as well as ground vias.

It is observed that the radiated field from the testing frill decays much faster than that from the antipad aperture and only a couple of modes are enough for convergence, even when the testing ring is close to the barrel. Based on this observation, we derive a closed-form expression to compute the via coupling through the higher-order parallel-

plate modes, which significantly increases the efficiency of the proposed algorithm. It is also seen that the use of the reciprocity theorem is beneficial because the numerical integration over the antipad is separated from solving the EFIE. Instead, it becomes a post-processing step: this integral appears after an *analytical* calculation (radiation due to the testing frill). This one-time numerical integral also helps to accelerate the computation.

3.2 Port Current Formulation using Reciprocity

Consider a one-layer multi-via structure as depicted in Figure 3.3. Assume that the power/ground plates have infinite extent and are perpendicular to the z-direction and all metals are perfect electric conductors (PECs).

The radius of all via barrels is a and the substrate layer thickness is h. For a shared-antipad, the outer radius is b and the separation between the center of the two barrels (the pitch) is s. The substrate material is homogeneous with permittivity ϵ and permeability μ.

We define ports on the antipads corresponding to barrels for the network parameter Y_{ij} computation. These are ideal ports where a transverse-electromagnetic (TEM) field excitation is assumed to exist in the aperture of the antipad. Hence, the exterior feed network is effectively decoupled from the interior parallel-plate via system. For practical structures where the vias are excited by microstrip/stripline traces (see Figure 3.1), we can estimate the scattering parameters by shifting the reference plane from the antipad to the transmission line input. For cases where the coupling and radiation from the exterior feed network become important (or the TEM-port assumption becomes inaccurate), the exterior feed network will need to be included in the analysis of the system.

Y_{ij} is found by computing the port i current I_i when the voltage at port j is $V_j = 1$ V, and all ports other than j are short-circuited. For port j, the aperture

field is substituted by a magnetic surface current $\mathbf{M}_s$ in the antipad region and the aperture is closed with a piece of perfect conductor using the equivalence principle. This magnetic surface current is referred to as source A, namely $\mathbf{M}_{sA}$. It should be noted that the shape of the antipad aperture is arbitrary, including single-ended vias and multiple vias sharing the same antipad.

The scheme using the concept of reaction [79] is shown in Figure 3.4. A unit-amplitude magnetic ring frill $K = 1$ V is used for the "measurement" of the current I_i. This ring source is referred to as source B, namely $\mathbf{K}_B$. As it plays a similar role as a "testing function" or "weighting function" in the method of moments (MoM) formulation [81], it is also called a "testing" source. This testing frill B encircles the barrel at port i along a path C_B, where the subscript A or B is used to denote source A or B, respectively.

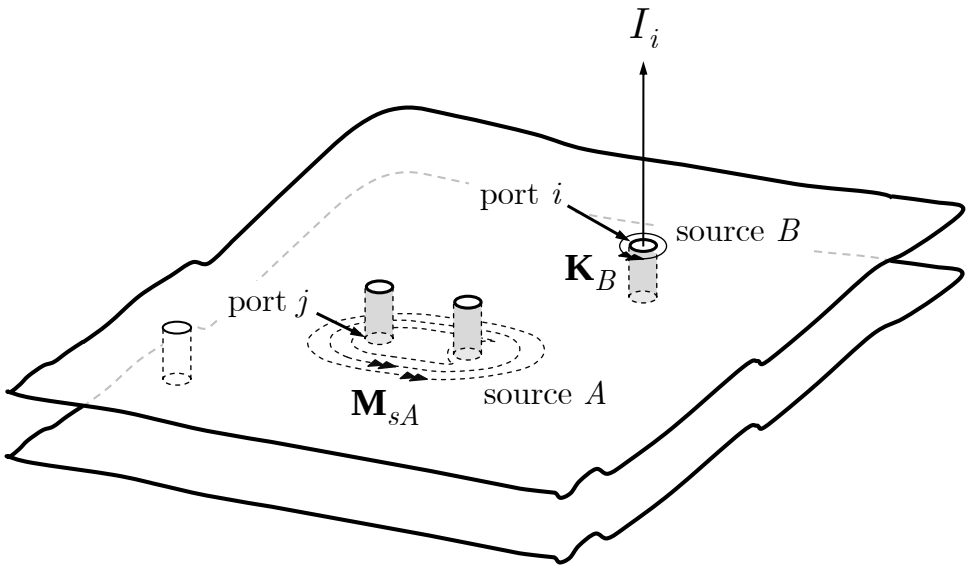

Figure 3.4. The current "measurement" scheme using the circuit reaction. I_i is "measured" by a unit-amplitude magnetic ring source $\mathbf{K}_B$ that encircles the barrel at port i.

From Ampere's law and using $K_B = 1$ V,

$$I_i = \oint_{C_B} (\mathbf{H}_A \cdot \mathbf{dl}) = K_B \oint_{C_B} (\mathbf{H}_A \cdot \mathbf{dl}) \tag{3.1}$$
$$= \oint_{C_B} (\mathbf{H}_A \cdot \mathbf{K}_B) dl = - < A, B >,$$

where the notation $< A, B >$ represents the reaction of source A onto source B.

From the reciprocity theorem,

$$< A, B > = < B, A > = - \iint_{S_A} (\mathbf{H}_B \cdot \mathbf{M}_{sA}) dS, \tag{3.2}$$

where S_A is the antipad aperture at source A. Note that in the reciprocal reaction $< B, A >$ the radiating source is B and the aperture at port j has been closed with PEC. The reactive near field from the higher-order parallel-plate modes due to source B (the 1-V testing ring frill) is omnidirectional and is also much more localized than that due to source A, and thus easier and faster to compute.

Assume the aperture field at port j is that of a TEM mode, which should be accurate for electrically small antipads that are used in practical designs. Using the equivalent magnetic current $\mathbf{M}_{sA} = \hat{\mathbf{z}} \times \nabla \Phi_A$, as well as $\mathbf{H}_B = (1/\mu) \nabla \times \mathbf{A}_B$,

$$I_i = \frac{1}{\mu} \iint_{S_A} (\nabla \times \mathbf{A}_B) \cdot (\hat{\mathbf{z}} \times \nabla \Phi_A) dS, \tag{3.3}$$

which is then reduced to

$$I_i = \frac{1}{\mu} \iint_{S_A} [\nabla \cdot (\mathbf{A}_B \times (\hat{\mathbf{z}} \times \nabla \Phi_A)) + A_{zB} \nabla^2 \Phi_A] dS, \tag{3.4}$$

where the last term in the resulting integrand is zero from the Laplace equation.

Applying the 2-D divergence theorem,

$$I_i = \frac{1}{\mu} \oint_{C_A} \hat{\mathbf{n}} \cdot [\mathbf{A}_B \times (\hat{\mathbf{z}} \times \nabla \Phi_A)] dl, \tag{3.5}$$

where C_A denotes the conductor boundaries at antipad A and $\hat{\mathbf{n}}$ is the horizontal unit normal vector for path C_A that points *outward* from the antipad region (towards the metal) at the boundaries.

The formula is further simplified to

$$I_i = -\frac{1}{\mu} \oint_{C_A} [A_{zB}(\hat{\mathbf{n}} \cdot \nabla \Phi_A)] dl, \tag{3.6}$$

where we recognize $\hat{\mathbf{n}} \cdot \nabla \Phi_A = (1/\epsilon)\rho_{sA}$. This yields the final formula for the port i current I_i as

$$I_i = -\frac{1}{\mu\epsilon} \oint_{C_A} A_{zB} \cdot \rho_{sA} dl, \tag{3.7}$$

where A_{zB} is the vector potential radiated by $\mathbf{K}_B$ (with all barrels present but all apertures shorted). It should be noted that an infinite parallel-plate environment is assumed for the A_{zB} calculation, though the analysis can be extend to consider the reflection from the boundary of the parallel-plate waveguide using the methods similar to those discussed in [27], [35], [66].

ρ_{sA} is the surface charge density on the boundaries of the antipad at port j when $V_j = 1$ V. In practical designs where there exist pads (in order for vias to connect to traces or other circuit components), the effects of the pads can be accounted for by the ρ_{sA} calculation. It is well known that ρ_{sA} is the solution to the static integral

equation

$$\Phi_A(\boldsymbol{\rho}) = -\oint_{C_A} \frac{1}{2\pi\epsilon} \ln|\boldsymbol{\rho} - \boldsymbol{\rho}'| \rho_{sA}(\boldsymbol{\rho}') dl', \tag{3.8}$$

and the Dirichlet boundary condition is enforced at the antipad metal boundary. The numerical results for ρ_{sA} are obtained from a static method of moments (MoM) [82] solution. The details of the MoM formulation and implementation can be found in Appendix B.

3.3 Radiation from the Testing Magnetic Ring Frill

The testing magnetic ring $\mathbf{K}_B$ on port i sets up currents on all of the barrels [83], [84]. In the coordinate system of any particular barrel p, a vertical modal expansion for the magnetic vector potential radiated between the parallel-plates by barrel p is expressed as

$$A_z^{p,p}(\rho, \phi, z) = \sum_{l=0}^{\infty} A_z^{p,p;l}(\rho, \phi) \cos(k_{zl} z), \tag{3.9}$$

where the index l corresponds to the order of the vertical mode and $k_{zl} = l\pi/h$ to match the PEC boundary conditions at the top/bottom plates. The superscript (p, q) before the semicolon denotes the fields observed in the coordinate system of barrel p due to the radiation from barrel q. Hence $A_z^{p,p;l}$ represents the l^{th}-order fields from self-radiation.

Allowing for all possible azimuthal modes of order n,

$$A_z^{p,p;l} = \sum_{n=-\infty}^{\infty} c_n^{p;l} H_n^{(2)}(k_{\rho l}\rho) e^{jn\phi}, \tag{3.10}$$

where $k_{zl}^2 + k_{\rho l}^2 = k^2$ and $H_n^{(2)}(\cdot)$ denotes the n^{th}-order Hankel function of the second kind. The unknown coefficient $c_n^{p;l}$ represents barrel p radiation into the $(n; l)$ mode

and is to be determined.

The Graf's addition theorem [85] is used to compute the mutual-radiation $A_z^{p,q;l}$. The theorem states that a displaced cylindrical harmonic is a linear superposition of the undisplaced cylindrical harmonics, which allows for translating the vector potential from the radiating barrel (displaced cylinder) to the observation barrel (undisplaced cylinder).

Referring to Figure 3.5 where the translation from the source barrel q to the observation barrel p is shown, in the coordinate system of barrel p with $\rho < \rho_{pq}$, with the appropriate formula of the addition theorem, the mutual-radiation from barrel q is

$$\begin{aligned} A_z^{p,q;l} &= \sum_{n=-\infty}^{\infty} c_n^{q;l} H_n^{(2)}(k_{\rho l}\rho') e^{jn\phi'} \\ &= \sum_{n=-\infty}^{\infty} c_n^{q;l} \sum_{m=-\infty}^{\infty} H_{n-m}^{(2)}(k_{\rho l}\rho_{pq}) J_m(k_{\rho l}\rho) e^{j(n-m)\phi_{pq}} e^{jm\phi}, \end{aligned} \tag{3.11}$$

where (ρ, ϕ) denotes the observation coordinate (barrel p); (ρ', ϕ') denotes the source coordinate (barrel q) and $\boldsymbol{\rho}' = \boldsymbol{\rho} + \boldsymbol{\rho}_{pq}$.

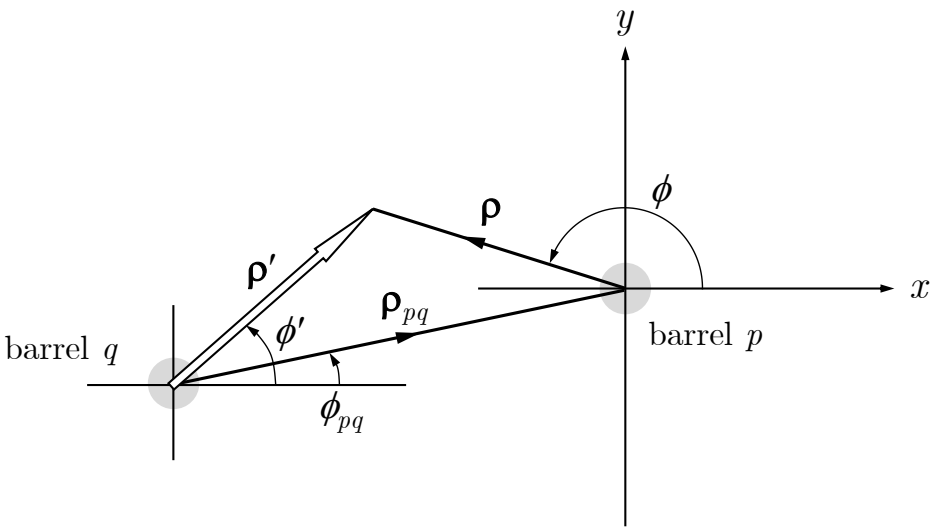

Figure 3.5. Translating the radiation from barrel q (ρ', ϕ') into the coordinate system of barrel p (ρ, ϕ).

Including all P barrels in the via system, the total radiation in the coordinate system of barrel p is then given by

$$A_z^{p;l}(\rho,\phi) = \sum_{q=1}^{P} A_z^{p,q;l} = A_z^{p,p;l} + \sum_{\substack{q=1 \\ q\neq p}}^{P} A_z^{p,q;l}. \tag{3.12}$$

The vector potential A_{zB} is zero on the surface of all barrels except the one with the testing magnetic ring current $\mathbf{K}_B$, which is labeled as barrel *test*. In the local coordinates of barrel *test*, a Fourier expansion of this 1-V source at $z = z'$ in terms of vertical harmonics is

$$\begin{aligned} M_{s\phi}^{\text{test}} &= \sum_{l=0}^{\infty} M_{s\phi}^{\text{test};l} \\ &= \sum_{l=0}^{\infty} \frac{2\cos(k_{zl}z')}{h(1+\delta_{l0})}\cos(k_{zl}z), \end{aligned} \tag{3.13}$$

where δ_{l0} is the Kronecker delta. Using $\mathbf{E}^{\text{test}} = \hat{\boldsymbol{\rho}} \times \mathbf{M}_s^{\text{test}}$, the vector potential on barrel *test* is

$$A_z^{\text{test};l} = \frac{j\omega\mu\epsilon}{k_{\rho l}^2} M_{s\phi}^{\text{test};l}. \tag{3.14}$$

Limiting the azimuthal variations ($-N < m, n < N$) and performing mode-matching on the surfaces of the barrels leads to a linear system for the unknown coefficients $c_n^{q;l}$ associated with all the barrels. Next, the ϕ-variation is removed by multiplying $e^{-jm'\phi}$ on both sides of the resulting linear system and integrating over any interval with length of 2π, and then dividing by 2π. This yields a matrix equation

$$[T_{m,n}^{p,q;l}][c_n^{q;l}] = [b_m^{p;l}], \tag{3.15}$$

as depicted in Figure 3.6.

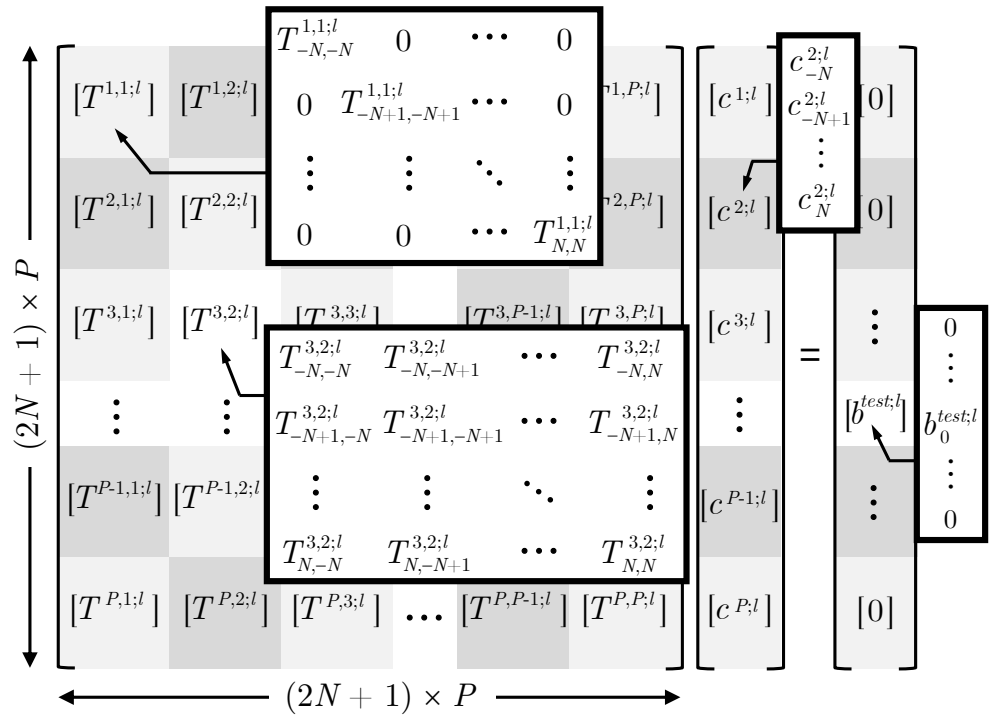

Figure 3.6. A graphical illustration of the linear system. The total system matrix/vector is tiled up using the sub-matrices/sub-vectors shown in the expanded views.

The $[T]$ matrix is used to translate the total vector potential among all the barrels. The size of $[T]$ is $((2N+1)\times P)\times((2N+1)\times P)$ where the non-zero elements are

$$\begin{cases} T^{p,p;l}_{m,m} = H^{(2)}_m(k_{\rho l}a), \\ T^{p,q;l}_{m,n} = J_m(k_{\rho l}a)H^{(2)}_{n-m}(k_{\rho l}\rho_{pq})e^{j(n-m)\phi_{pq}}. \end{cases} \tag{3.16}$$

A physical interpretation of $T^{p,q;l}_{m,n}$ is a translation of the ϕ-harmonics, from the n^{th}-order one on barrel q to the m^{th}-order one on barrel p, for the l^{th}-order vector potential component of A_{zB}.

The $[b]$ vector comes from the mode-matching boundary conditions. Since the testing frill excitation is omnidirectional, only the 0^{th}-order ϕ-harmonic on barrel *test*

is used, where

$$b_0^{\text{test};l} = \frac{2j\omega\mu\epsilon\cos(k_{zl}z')}{k_{\rho l}^2 h(1+\delta_{l0})}. \tag{3.17}$$

The unknown coefficient $c_n^{q;l}$ can be solved from $[c] = [T]^{-1}[b]$. The l^{th}-order vector potential component of A_{zB} is then computed by summing up the radiation from all barrels. The total radiation field for all vertical modes in the parallel-plate system is obtained by summing the fields for each l^{th}-order mode (each mode being independent of the others, as the vertical modes do not couple). Theoretically, the value of A_{zB} is calculable to any accuracy determined by the truncation of the vertical modes $l \leq L$.

3.4 Algorithm Advantages

The main difference in the proposed algorithm based on reciprocity from other existing methods is the sequential order of the numerical integration over the antipad aperture: we move this numerical integration from a step where we compute the incident field radiated by the aperture, as done in the usual EFIE approach, to a post-processing step in the reaction calculation. The advantages of doing so are summarized in the following.

3.4.1 Total-Field Formulation

The numerical integration over the source antipad is a part of the usual EFIE approach, where an incident/scattered-field formulation is often assumed. In fact, it appears in the calculation of the incident field from the antipad, and is re-computed for all barrels and for all vertical and azimuthal modes. This involves extensive evaluation of Bessel functions, i.e., $J_m(\cdot)$, $H_m^{(2)}(\cdot)$, making the computation time-consuming. An estimate of the number of calls of the Bessel functions required by an EFIE approach which uses 1-D discretization and integration along the antipad boundary can be found in Appendix E.

The proposed approach, on the other hand, is based on the *total-field* formulation.

The right-hand-side vector $[b_m^{p;l}]$ is simply computed from the total A_{zB} on the surfaces of the via barrels, which is zero for all barrels except for the one with the testing frill, and the nonzero entry for that barrel is given by Eq. (3.17). It is seen that the system matrix $[T_{m,n}^{p,q;l}]$ used here is identical to that from the 1D-EFIE approach, and therefore the main difference in computation cost compared to the EFIE approach arises from calculating A_{zB} along the antipad boundary, as is required by the post-processing step Eq. (3.7). It should be noted that we only need to calculate A_{zB} along the *outer* boundary of the antipad, because the values for A_{zB} along the inner boundaries are already computed when we built the linear system Eq. (3.15) (as a part of the right-hand-side vector evaluation). This highly reduces the amount of evaluations for the Bessel functions, especially for structures with multiple vias sharing the same antipad, where there are a lot of sampling points along the inner boundaries of the antipad.

3.4.2 Fast Convergence

Using reciprocity, the fields radiated from the testing frill (source B), rather than the antipad aperture (source A), is computed. A benefit of doing so is that the *higher*-order parallel-plate mode radiation from the testing frill is much more localized, and thus fewer parallel-plate modes are needed for convergence, compared to that from an antipad. This is because the antipad has a larger size and an irregular shape and is physically closer to the nearby barrels than the testing frill.

As a result, the testing frill "sees" fewer barrels than the antipad in terms of having weaker mutual coupling and thus needing fewer harmonics. For sufficiently higher-order vertical modes where the testing frill radiation is so localized that negligible currents are induced on the surrounding barrels, the testing frill radiates as if there are no other barrels present other than barrel *test*. It therefore produces an omnidirectional field which can be computed using a closed-form expression.

3.4.3 Closed-Form Expressions

When the radiation from the testing frill is much weaker at the antipad outer boundary than the inner one, the numerical integration in Eq. (3.7) can be approximated to that along the inner boundary only ($\rho = a$). Also, when the higher-order mutual-coupling between the testing frill and neighbor barrels is negligible, there is no need to solve for the mode-matching coefficients $c_n^{q;l}$ using the steps described in Section II-B to find the higher-order mode contribution to the field A_{zB}. Instead, an analytical formula is derived by retaining only barrel *test* in the via system. These situations arise when the antipad is on the same barrel as the testing frill. When the testing frill is on the bottom ground plane where $z' = 0$, the contribution from the higher-order parallel-plate modes (for l_1 and higher) is

$$A_{zB}^{\text{high}} \approx \frac{2j\omega\mu\epsilon}{h} \sum_{l=l_1}^{\infty} \frac{1}{k_{\rho l}^2}. \tag{3.18}$$

Kummer's transformation [85] is used to accelerate the convergence of the series. If $k_{zl} \gg k$, $k_{\rho l} \approx -jk_{zl} = -jl\pi/h$, and the following relation holds:

$$\begin{aligned} A_{zB}^{\text{high}} &\approx \frac{2j\omega\mu\epsilon}{h} \left[\sum_{l=l_1}^{\infty} \left(\frac{1}{k_{\rho l}^2} + \frac{h^2}{l^2\pi^2} \right) - \sum_{l=l_1}^{\infty} \frac{h^2}{l^2\pi^2} \right] \\ &\approx -\frac{2j\omega\mu\epsilon h}{\pi^2} \left(\frac{\pi^2}{6} - \sum_{l=1}^{l_1-1} \frac{1}{l^2} \right), \end{aligned} \tag{3.19}$$

where l_1 indicates the first higher-order mode. The value of l_1 is determined using the rule given in Appendix F. In Eq. (3.19) the last term appearing in the first line has been rewritten using $\sum_{l=1}^{\infty}(1/l^2) = \pi^2/6$, known as the Riemann $\zeta(2)$ function [86]. This infinite series converges very slowly, implying that a lot of vertical modes are required to get the result accurately.

A similar expression is obtained when $z' = h$. The sum of the lower- and higher-

order results will give the total radiation A_{zB}. The accuracy of Eq. (3.19) depends on the correctness of $k_{zl} \gg k$ and the small field at the antipad outer boundary: a thinner substrate, lower frequency, and larger antipad will make Eq. (3.19) a more accurate expression.

3.5 Numerical Results and Discussions

Several multi-via structures are studied to evaluate the accuracy and efficiency of the proposed method. A Matlab script is written based on the proposed algorithm. The via layout parameters include (in millimeters): barrel radius $a = 0.13$, pitch $s = 1.00$, antipad radius $b = 0.38$, layer thickness $h = 0.31$. These layout parameters are shown in Figure 3.7. The substrate has $\epsilon_r = 4.0$ and $\mu_r = 1.0$. The admittance matrix is estimated using the maximum number of vertical modes of $L = 10$ and a maximum azimuthal variation $N = 1$ (three azimuthal modes).

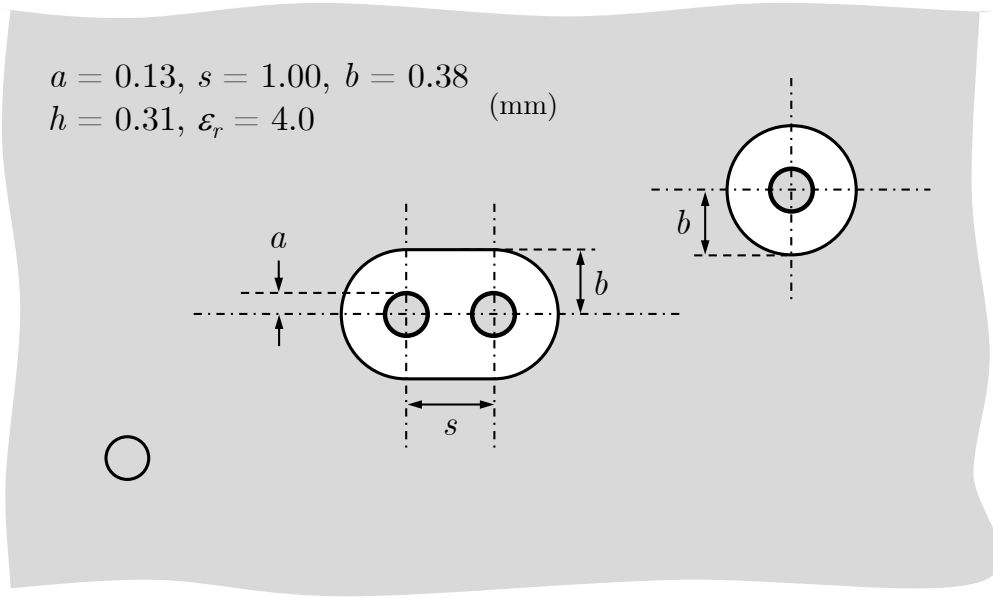

Figure 3.7. The layout parameters for a pair of differential vias, and single-ended via with circular antipad, and a grounding via.

The same structures are also analyzed using our implementation of the 1D-EFIE method. In the comparison with 1D-EFIE, we use the same number of vertical and azimuthal modes as in the proposed method. They are also analyzed using Ansys

HFSS 15.0 on a PC with an Intel Core i7 CPU and 8 GB memory. In HFSS, the infinite plates are modeled using a pair of circular parallel plates with a radius of 6.35 mm terminated by a "radiation-only" boundary condition. The average edge length for the tetrahedral mesh is 0.12 mm.

3.5.1 Single-Layer of Vias

3.5.1.1 Two Single-Ended Vias with Circular Antipads

For a single layer of two vias with circular antipads as shown in Figure 3.8, we compare the proposed method with both analytical formulas and the physical-based model [22]. The via-plate capacitance C_{via} is extracted based on [19]. The accuracy of the proposed closed-form expression Eq. (3.19) is also investigated. The mixed-mode S-parameter comparison is shown in Figure 3.9 and Figure 3.10. The differential port $\text{P}_\text{d}1$ is made of two single-ended port P1 and P3, with P1 being the positive end and P3 being the negative end, and the definition for the differential pair $\text{P}_\text{d}2$ is similar to $\text{P}_\text{d}1$.

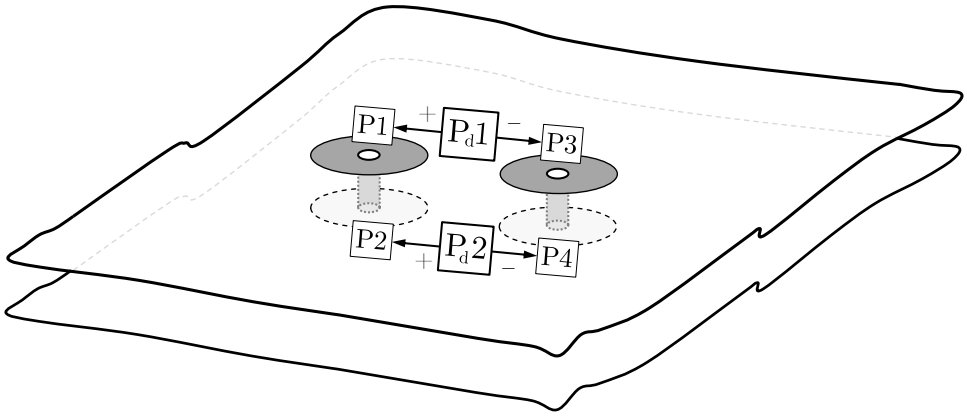

Figure 3.8. Two single-ended vias with circular antipads. Differential pair $\text{P}_\text{d}1$ comprises P1(+) and P3(-).

From Figure 3.9 and Figure 3.10, we can observe that the proposed approach produces consistent results with the analytical formulas [80]. This is expected since the only approximation in the proposed method (compared to analytical model) is

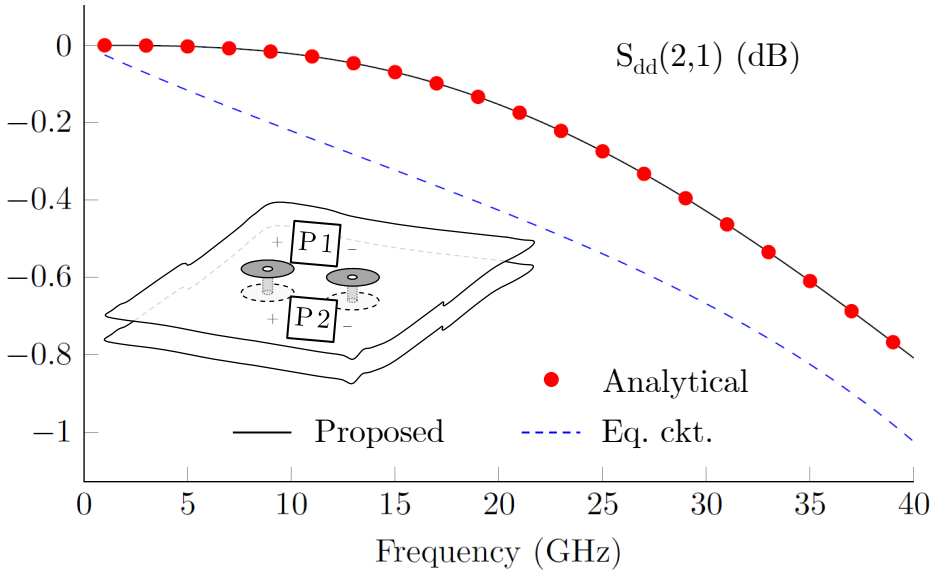

Figure 3.9. Insertion loss comparisons for differential mode signals: proposed method vs. analytical method vs. equivalent circuit model. The proposed method is using $L = 600$.

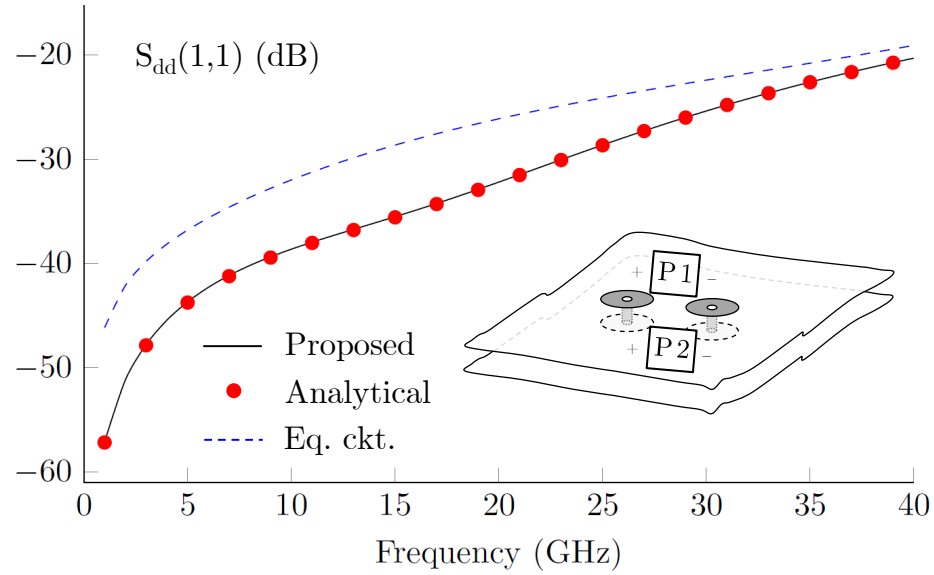

Figure 3.10. Reflection coefficient comparisons for differential mode signals: proposed method vs. analytical method vs. equivalent circuit model. The proposed method is using $L = 600$.

the numerical integral along the antipad boundary. In the proposed approach used to generate the results, the antipad outer boundary is uniformly discretized into 90 line segments. However, the equivalent circuit model gives results that deviates from the other two, because the equivalent circuit model ignores the radiation effects of the antipad.

3.5.1.2 Two Differential Pairs in a 5×5 Via Array

A single layer of vias with a layout of a 5×5 via array is shown in Figure 3.11. Four differential ports are shown, with the odd-numbered ports 1 and 3 on the top plate and the even-numbered ports 2 and 4 on the bottom plate. Port 2 is directly below port 1 and port 4 is directly below port 3. The S-parameters evaluated using the proposed method, the 1D-EFIE approach and HFSS are shown in Figure 3.12 and Figure 3.13, and the results using the closed-form expression Eq. (3.19) to accelerate the calculation are also shown. It is seen that the closed-form expression is accurate within the frequency range reported.

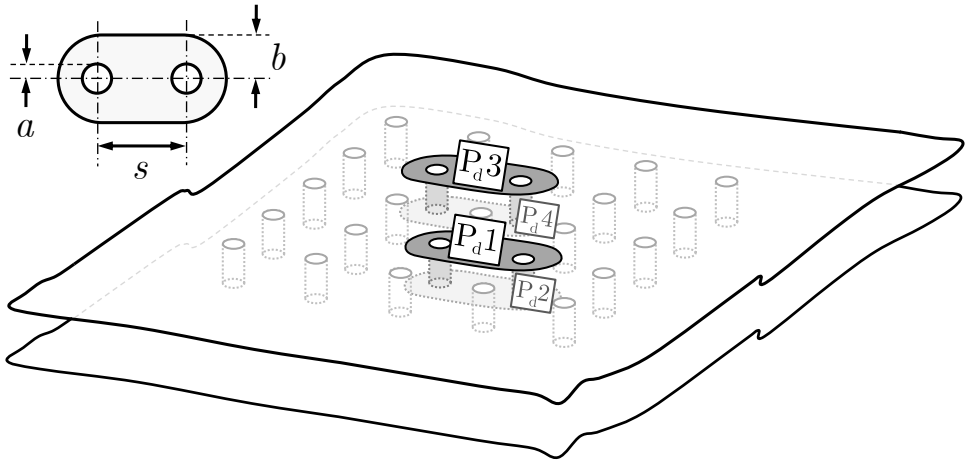

Figure 3.11. A 5×5 via array structure. Differential ports 1 and 3 are associated with the two shared-antipads on the top plate.

The convergence of the results with respect to the vertical mode upper bound L is shown in Figure 3.14. The percent relative error of the S-parameters is estimated using L up to 10. The reference for evaluating the relative error are the S-parameters

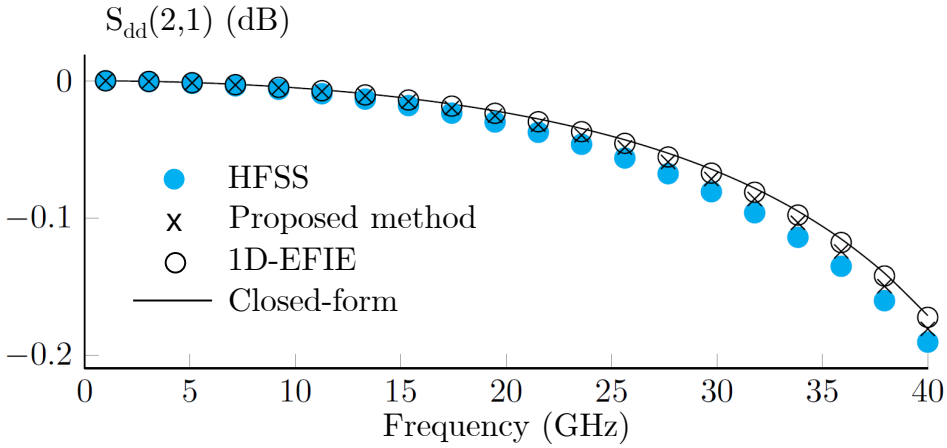

(a) Insertion loss amplitude comparison.

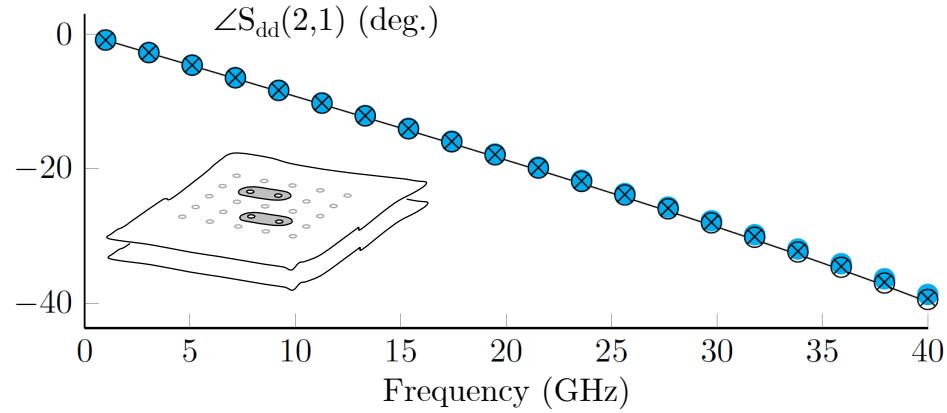

(b) Insertion loss phase comparison.

Figure 3.12. Insertion loss comparisons for differential mode signals: proposed method vs. HFSS vs. 1D-EFIE vs. closed-form Eq. (3.19).

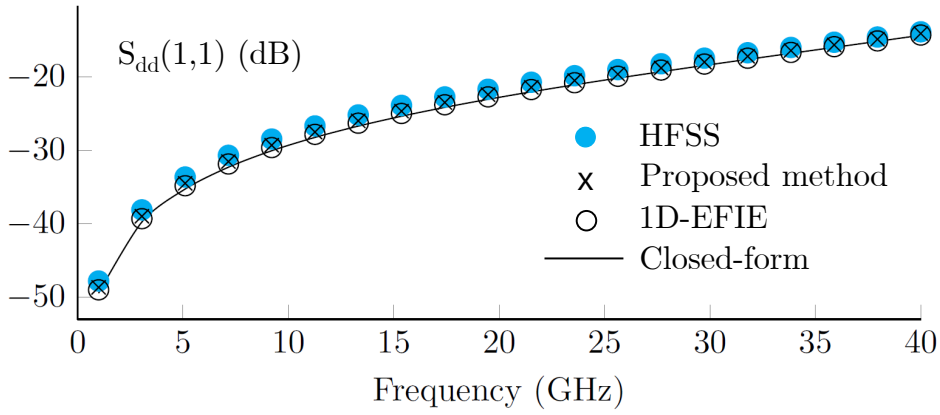

(a) Reflection coefficient comparison.

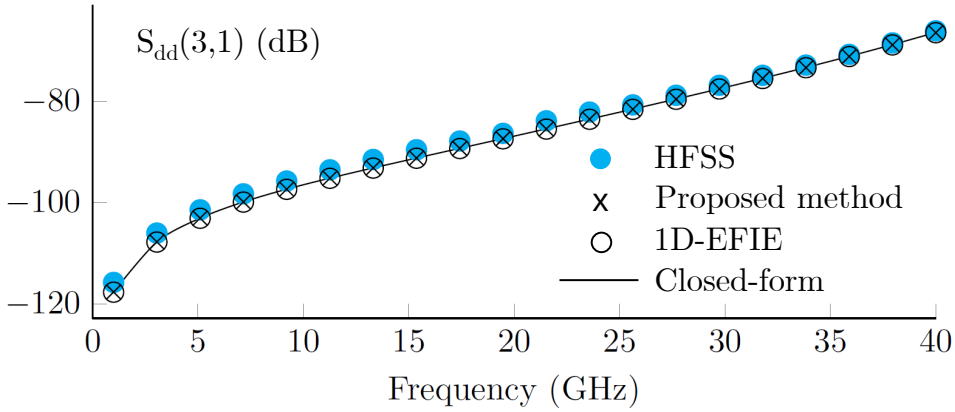

(b) Cross-talk comparison.

Figure 3.13. *S*-parameter comparisons for differential mode signals: proposed method vs. HFSS vs. 1D-EFIE vs. closed-form Eq. (3.19).

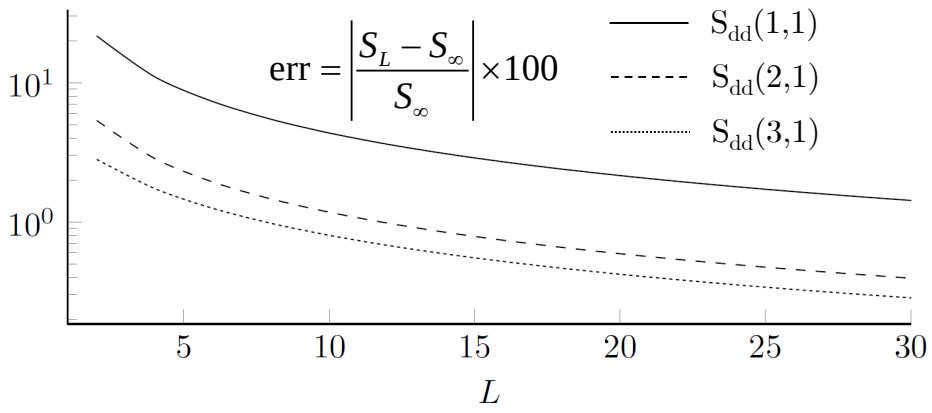

Figure 3.14. Percent relative error for S-parameters vs. L (the maximum number of vertical modes). S_∞ is the result when $L = 6000$.

calculated with $L = 6000$, labeled by S_∞. It is observed that the reflection coefficient converges much slower than the insertion loss and crosstalk. This is because the reflection coefficient is much smaller compared to the insertion loss and thus more vertical modes are required to achieve the same accuracy level. The crosstalk, on the other hand, is also very small, but it only requires a few vertical mode to compute because of the separation between the vias, which means that there is negligible interaction due to higher-order vertical modes beyond the first few.

3.5.1.3 Eight Differential Pairs in a 8×7 Via Array

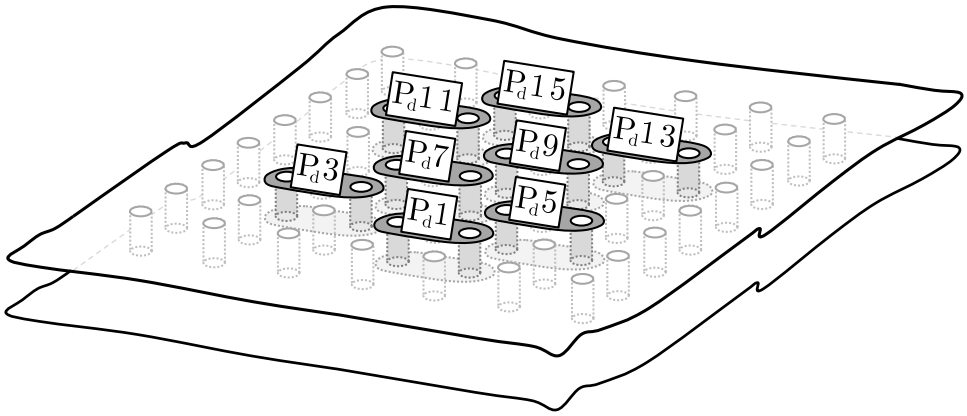

Figure 3.15. An 8×7 via array structure. Differential ports 1 through 16 are placed at the shared antipads. The even-numbered ports are placed on the bottom plate.

Figure 3.15 depicts a single-layer 8×7 via array structure. The corresponding differential S-parameter comparisons are shown in Figure 3.16 and Figure 3.17. Even for this more complicated structure, the results from the proposed method agree well with those obtained using HFSS and the 1D-EFIE method.

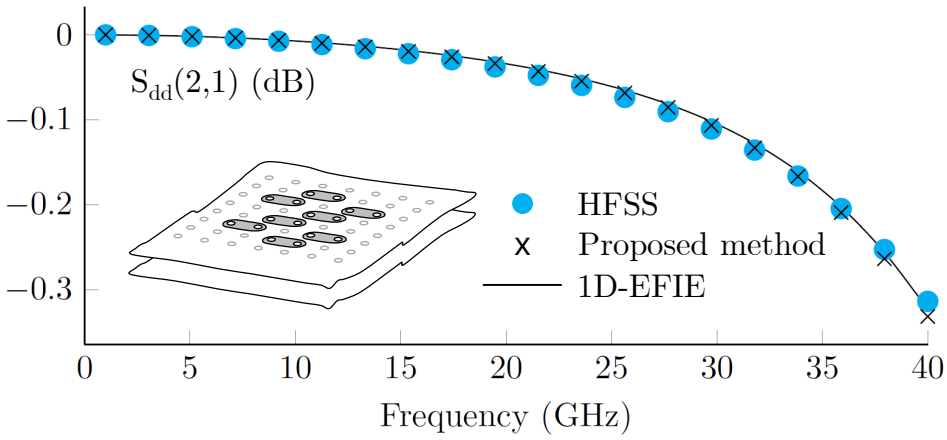

(a) Insertion loss comparison.

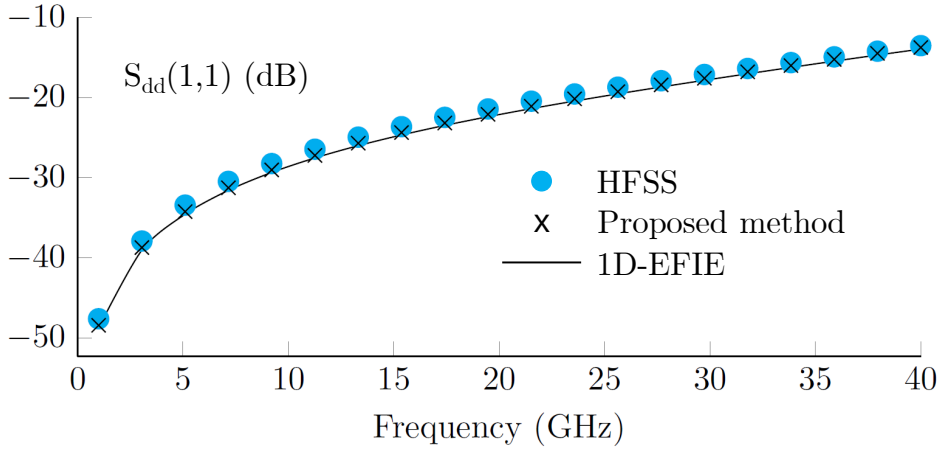

(b) Reflection coefficient comparison.

Figure 3.16. S-parameter comparisons for differential mode signals: proposed method vs. HFSS and 1D-EFIE. The structure is a single-layer 8×7 via array.

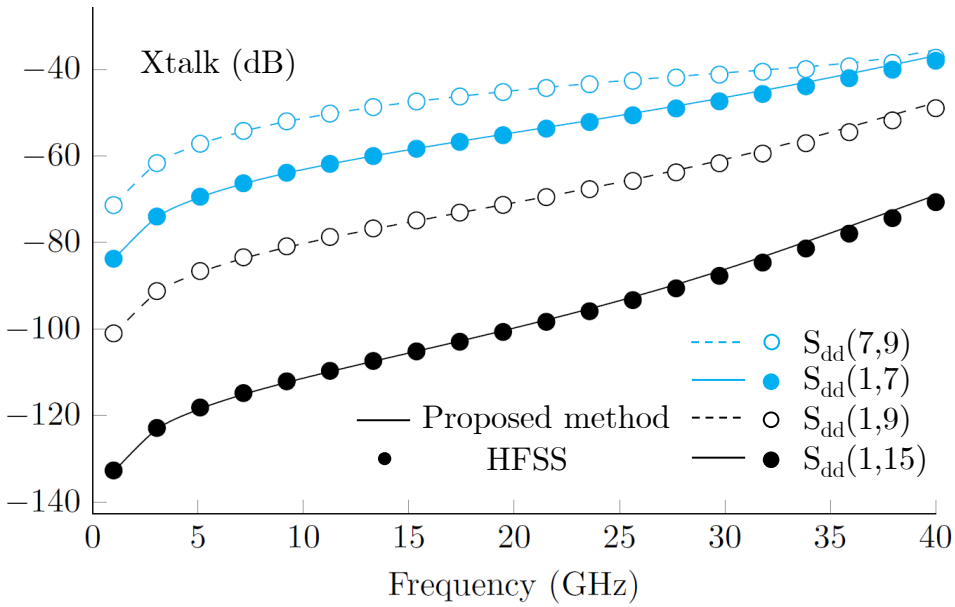

Figure 3.17. Cross-talk comparisons for differential mode signals: proposed method vs. HFSS and 1D-EFIE. The structure is a single-layer 8×7 via array.

3.5.2 Multiple Layers of Vias

3.5.2.1 Eight Differential Pairs in a 8×7 Via Array

A seven-layer 8×7 via array structure as shown in Figure 3.18 is analyzed next. Each layer is assumed to have identical thickness h. The behavior of a multi-layer via structure can be obtained by cascading the $ABCD$ matrix of each single layer. The corresponding S-parameters are plotted in Figure 3.19 and Figure 3.20. The agreement with HFSS is quite good, verifying that the proposed method can be used to treat multilayer structures through a direct cascading of the network parameters obtained for each layer.

A comparison of the computational cost of the proposed approach, the 1D-EFIE method and HFSS is given in Table 3.1. The recorded time is the average elapsed time for generating the full network S-matrix for a single frequency point. It is observed that the proposed method is very efficient compared to HFSS. It is also faster than the 1D-EFIE approach because of the use of reciprocity, which is explained by counting the number of calls of the Bessel functions.

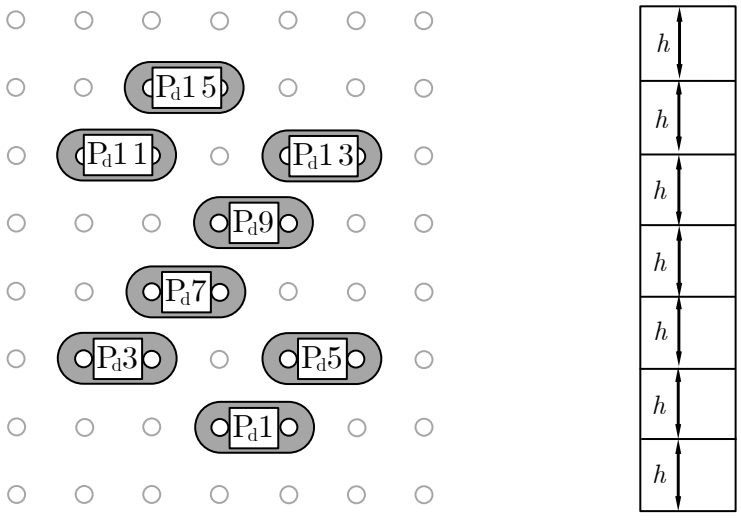

Figure 3.18. A 7-layer multi-via structure made by cascading the single-layer structure shown in Figure 3.15, showing (a) top view and (b) side view of the layers.

Table 3.1. Comparison of the computational costs

Pairs	**Array Size**	**HFSS Memory (MB)**	**HFSS Time[1](sec)**	**1D-EFIE Time[2](sec)**	**Proposed Time[1](sec)**
1	3×4	190	41	0.534	0.038
2	5×5	365	110	2.243	0.117
8	8×7	900	607	19.22	0.602

[1] The recorded time is the average elapsed time for generating the full network S-matrix for a single frequency point.

[2] The time consumed by the 1D-EFIE method is evaluated based on our own implementation of the method using Matlab.

The total number of calls of the Bessel functions required to compute the full network S-matrix of the 8×7 via array structure at a single frequency is 153168 for the proposed method, and 4771536 for the 1D-EFIE method. Among these, 120960 calls are consumed by each of the lower order modes for the proposed approach, and 433776 for the 1D-EFIE approach. These numbers agree with the formulas given in Appendix F. The efficiency and accuracy increases still further when using the closed-form expression Eq. (3.19) for all of the vertical modes.

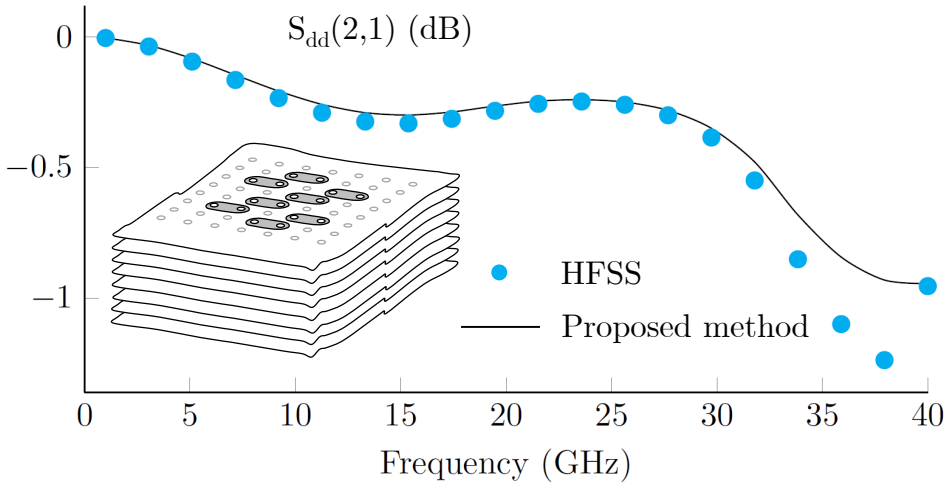

(a) Insertion loss comparison.

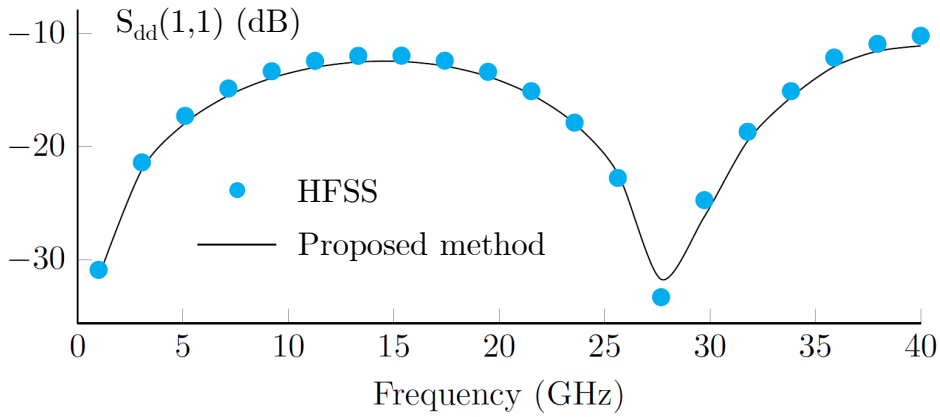

(b) Reflection coefficient comparison.

Figure 3.19. S-parameter comparisons for differential mode signals: proposed method vs. HFSS. The structure is a 7-layer 8×7 via array as shown in Figure 3.18.

3.6 Conclusions

In this chapter, an efficient analysis for vias with arbitrarily-shaped antipads in infinite parallel-plate structures was discussed using the reciprocity theorem.

The proposed network Y-parameter formulation was based on a reaction computation that converges very fast and is easy to formulate. The numerical integration over the antipad aperture was separated from the field calculation and was done only as a post-processing step. Using the divergence theorem, this surface integral was reduced

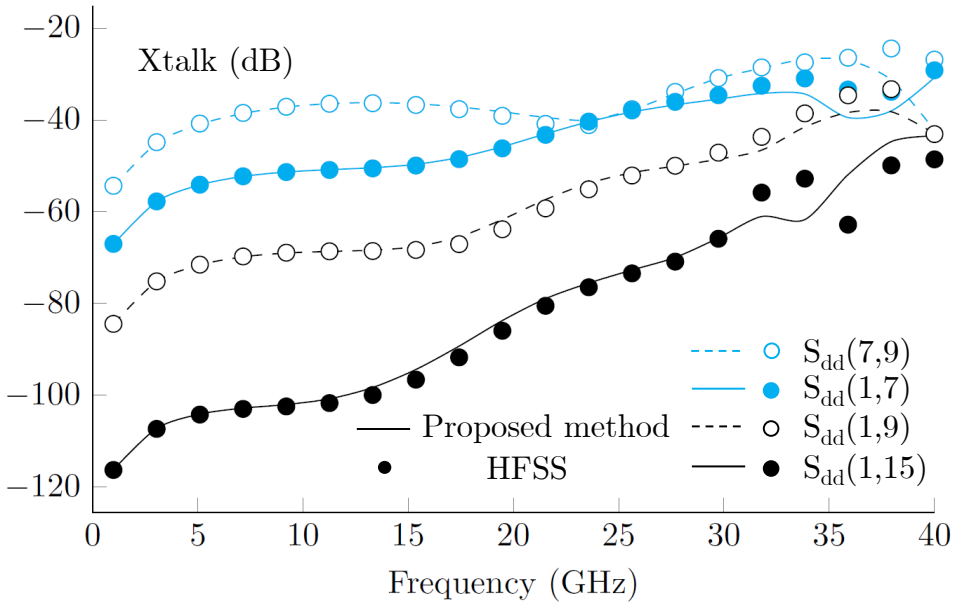

Figure 3.20. Cross-talk comparisons for differential mode signals: proposed method vs. HFSS. The structure is a 7-layer 8×7 via array as shown in Figure 3.18.

to a line integral along the antipad outer boundary.

The efficiency and convergence of the proposed algorithm was also discussed. It was shown that the use of reciprocity greatly improves the efficiency and provides faster convergence compared with the usual EFIE approach.

With this semi-analytical approach, the simulation time is reduced by a factor of over 1000 compared with HFSS and by a factor of over 20 compared with the 1D-EFIE approach, for the particular examples shown here.

Chapter 4

Leaky-Waves on a Fabry Pérot Cavity Antenna

In Chapter 4, we propose a leaky-wave study on a Fabry-Pérot resonant cavity antenna. The focus of this chapter is on examining the fundamental physics of the leaky waves propagating on this structure, and establishing that the principle of operation is indeed that of a leaky-wave antenna.

The structure considered in this chapter is a two-dimensional periodic patch antenna array excited by a single Hertzian dipole. The fields on the antenna decay slowly from the source and therefore a large number of patches are involved in the full-wave calculation, making the numerical evaluation of the patch currents expensive. To reduce the computational costs, we can use the array scanning method (ASM) [87].

ASM takes advantage of the fact that a non-periodic source can be expanded into a Fourier series, which conforms to the periodic structure. Since the response of a periodic structure to periodic sources is also periodic, it is possible to perform a unit-cell analysis, e.g., the integral-equation method using a periodic Green's function. Based on the ASM formulation, we can then estimate the contribution of leaky waves, which are defined by the residue integration corresponding to the leaky-wave poles.

Another topic this chapter is concerned with is the truncation effects of a finite-size leaky-wave antenna, as opposed to the infinite antenna where reciprocity can be used to compute the radiation pattern.

We begin this chapter by a historical review of the existing research on the two-dimensional Fabry-Pérot leaky wave antenna in Section 4.1. Section 4.2 introduces the ASM formulation to compute the antenna currents (the total currents), and based on this the leaky-wave currents are extracted in Section 4.3 using a residue integration of the leaky-wave poles. Two asymptotic formulas for the leaky-wave currents are

then derived. Using the antenna current densities, the radiation pattern is then evaluated in Section 4.4 and a leaky-wave dominance is observed. Section 4.5 discusses the "truncation effects" of a finite-size leaky-wave antenna using a patch array and radiation patterns are calculated. Section 4.6 concludes the analysis presented in this chapter.

4.1 Introduction

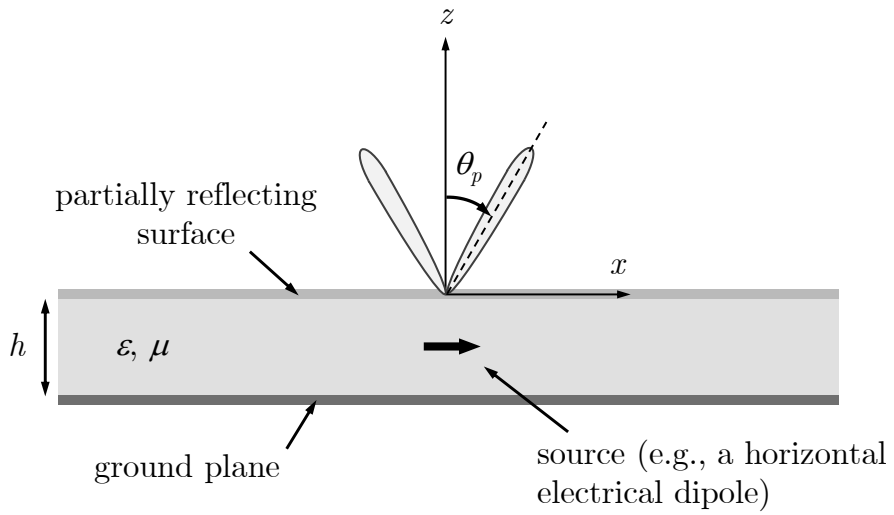

Figure 4.1. A Fabry-Pérot resonant cavity antenna excited by a x-directed electrical dipole inside the substrate. This antenna radiates a conical beam with a scan angle of θ_p.

The Fabry-Pérot resonant cavity antenna is used to obtain directive beams with a simple source excitation. Recently, this structure has attracted a lot of attention in the microwave and millimeter-wave region due to its low fabrication complexity. The name of the antenna comes from the Fabry-Pérot interferometer. A Fabry Pérot antenna typically consists of a grounded substrate and a partially reflective surface (PRS) on the top, and is excited with a single source, as shown in Figure 4.1. A resonant cavity region is formed between the ground plane and the PRS. The PRS exhibits an almost-total reflection which results in a small amount of power leakage to space along the PRS interface. This slowly-attenuating interface field produces a

large effective antenna aperture and hence such an antenna is capable of radiating a highly directive beam.

It is well established that the Fabry-Pérot resonant cavity antenna operates as a leaky-wave antenna, as the leakage through the PRS is attributed to leaky-wave propagation. Leaky waves are guided waves that can be characterized by complex wavenumbers, although the media involved are not necessarily lossy [42], [43]. The physics of a leaky-wave antenna were first investigated in [44] and historic background can be found in [88]–[90]. Although it is straightforward to use the reciprocity theorem to evaluate the antenna's far-field characteristics, the leaky-wave theory gives compact and elegant explanations of the fundamental radiation mechanism, as well as the antenna's near-field properties, e.g., currents and input impedance, whenever the leaky wave is dominant.

One of the historical limitations of leaky-wave antennas has been the inability to scan through broadside. For uniform or quasi-uniform leaky-wave antennas where the radiation occurs via the fundamental $n = 0$ mode, the leakage is from the guided mode and the beam can only point in the forward direction. The use of periodic structures helps to produce a beam that can point either in the backward or forward direction, and scans through broadside as the frequency changes. However, a stopband is normally encountered at broadside, where the beamwidth becomes very narrow and the radiated power drops significantly. This limitation can be overcome by introducing a novel metamaterial-inspired composite-right-hand-left-hand (CRLH) structure [91], [92] or other periodic structures [93].

Broadside radiation, on the other hand, was implemented much earlier than the concept of scanning through broadside, originating when the Fabry-Pérot leaky-wave antenna was invented in 1956 [94]. The Fabry-Pérot structure is capable of producing a broadside beam by exciting the structure in the middle, producing a radial leaky

wave. Essentially, the conical beam closes up to produce a single broadside beam. According to [95], maximum broadside radiation can be obtained when $\beta = \alpha$ and narrowest broadside beam occurs when $\beta = 0.518\alpha$. When $\beta > \alpha$, the beam will split to create a conical beam with a scan angle θ_p, as shown in Figure 4.1.

A periodic structure, also known as a frequency selective surface (FSS), is often used as a PRS for the Fabry-Pérot antenna. When the period is small so that the radiation occurs via the fundamental 0^{th}-order space harmonic (Floquet wave), it becomes a quasi-uniform structure and the analysis is similar to that of an antenna using a uniform PRS. An array of conducting metal patches (or slots in a conducting plane) is able to obtain similar behavior to that of a uniform PRS, near the resonant frequency. The design of such PRS made of periodic structures was introduced in [39]–[41], where the periodic structure is modeled as a sheet impedance in a transverse equivalent network (TEN) and the equivalent sheet impedance can be obtained using the reciprocity theorem.

The one-dimensional leaky wave has been studied extensively in the past [96]–[101]. A two-dimensional leaky-wave analysis, on the other hand, is generally considered challenging where omnidirectional radiation is often assumed [102] for modeling convenience. For a 2-D antenna made with FSS, the analysis becomes more difficult due to the complex Floquet modes supported by the periodic structures.

The canonical problems addressed in the largest part in the relevant literature on Fabry-Pérot cavity antennas with periodic structures are (a) the interactions with plane waves, e.g., radiation pattern calculation, and (b) the dispersion features of the Bloch modes in the absence of sources, e.g., the determination of the leaky-wave poles. However, studies of periodic PRS structures interacting with dipole sources, from which the patch current can be calculated, have been scare.

In [103], we proposed a leaky-wave analysis of a Fabry-Pérot cavity antenna with

patch array configuration using the array-scanning method (ASM), which is an ideal candidate to calculate the response of periodic structures from a single source. Based on the ASM formulation, the leaky-wave contribution to the total radiated fields can be extracted by a residue integration corresponding to the leaky-wave pole on the "improper" Riemann sheet.

4.2 Patch Current Calculation

Consider a Fabry Pérot leaky wave antenna using a 2-D patch array implementation as shown in Figure 4.2. The dimensions of this patch array include: the periodic spacing is a along the x-axis and b along the y-axis. The patch length is L and the patch width is W.

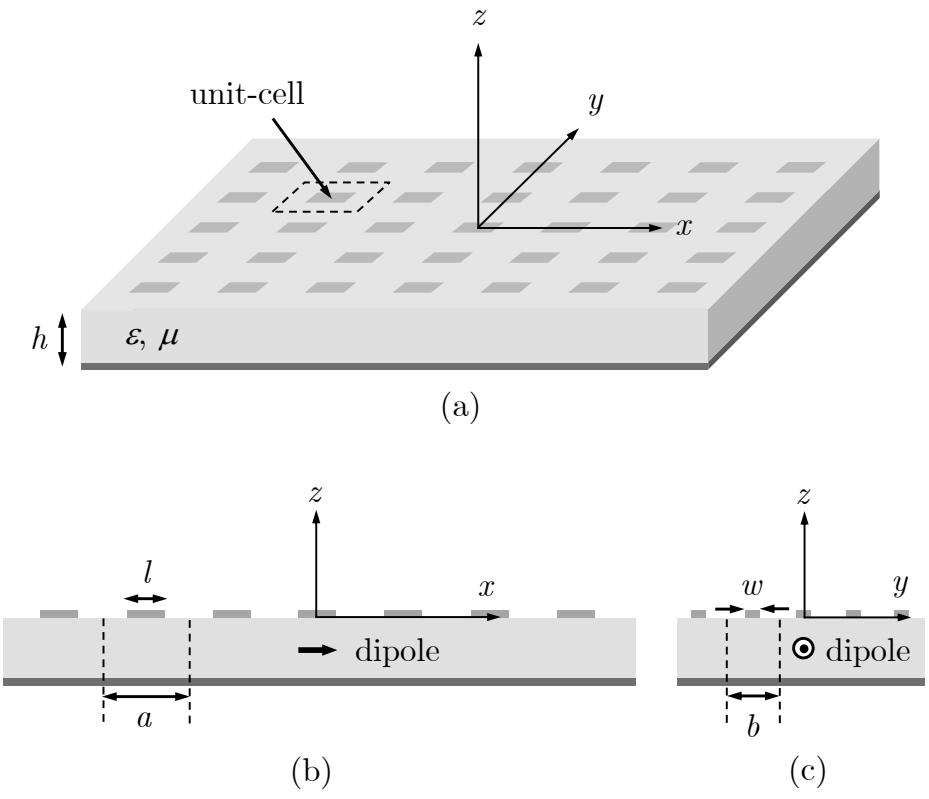

Figure 4.2. Fabry-Pérot resonant-cavity antenna using a periodic metal patch array as the PRS structure.

For a desired resonant frequency of $f_0 = 12$ GHz, on an air-substrate with $\epsilon_r = \mu_r = 1$, the patch length is chosen to be roughly one-half of a guided wavelength ($L = 12.5$ mm) in order to achieve significant reflection from the PRS. Narrow patches ($W = 1$ mm) are used here, assuring that the currents are almost entirely in the x-direction. The periods are then chosen as $a = 13.5$ mm and $b = 3$ mm. The value of the substrate thickness is chosen as $h = 13.33$ mm [39] so that $\beta \approx \alpha$ to have maximum power density radiated at broadside [95].

4.2.1 Array-Scanning Method

The array-scanning method (ASM) is numerically efficient for the analysis of periodic structures under non-periodic source excitation [104], especially when the observation point is vertically close to the source [105] as in the case of the Fabry Pérot cavity antenna depicted in Figure 4.2.

Unlike in the conventional spectral-domain approach [106] where plane-wave expansion is used, in ASM, the single dipole is synthesized by a phased-array of dipoles, with a phase difference of $(k_{x0}a + k_{y0}b)$, as shown in Figure 4.3. Hence, an auxiliary periodic phased-array problem is solved first using the periodic spectral-domain method of moments (MoM) approach.

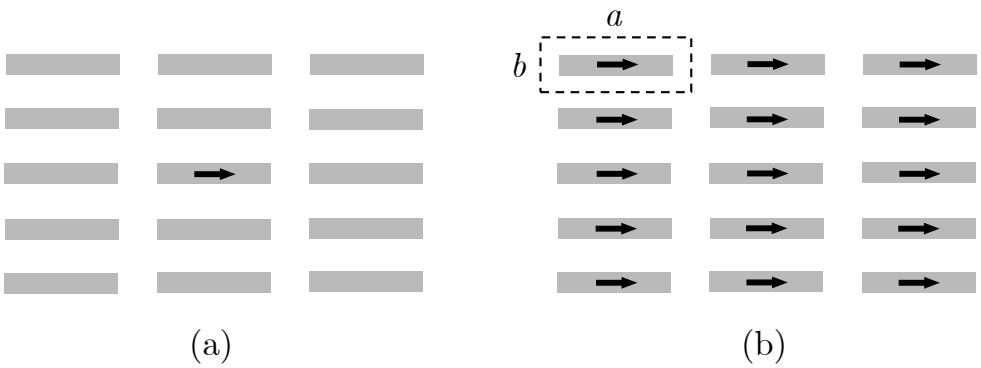

Figure 4.3. A top view of patches and dipole source(s) associated with them. The patch array is excited with (a) a single horizontal dipole and (b) a periodic phased-array of dipoles.

Once the auxiliary periodic problem is solved, a spectral integral is next used for the source synthesis. According to ASM, the relation between the aperiodically-excited fields Ψ [see Figure 4.3(a)] and the periodically-excited fields Ψ^{∞} with phasing (k_{x0}, k_{y0}) [see Figure 4.3(b)] is given by

$$\Psi(x,y,z) = \frac{ab}{(2\pi)^2} \int_{-\pi/b}^{\pi/b} \int_{-\pi/a}^{\pi/a} \Psi^{\infty}(k_{x0}, k_{y0}; x, y, z) dk_{x0} dk_{y0}, \tag{4.1}$$

where the superscript "∞" denotes the solutions to the auxiliary periodic phased-array problem. Here the integration area is referred to as the Brillouin zone [107].

4.2.2 Auxiliary Periodic Problem

Consider the auxiliary periodic problem where the single dipole underneath patch $(0,0)$ is replaced by a uniform phased-array of dipoles [see Figure 4.3(b)], with magnitude (Il) and a progressive phase shift of $-k_{x0}a$ along the x-direction and of $-k_{y0}b$ along the y-direction.

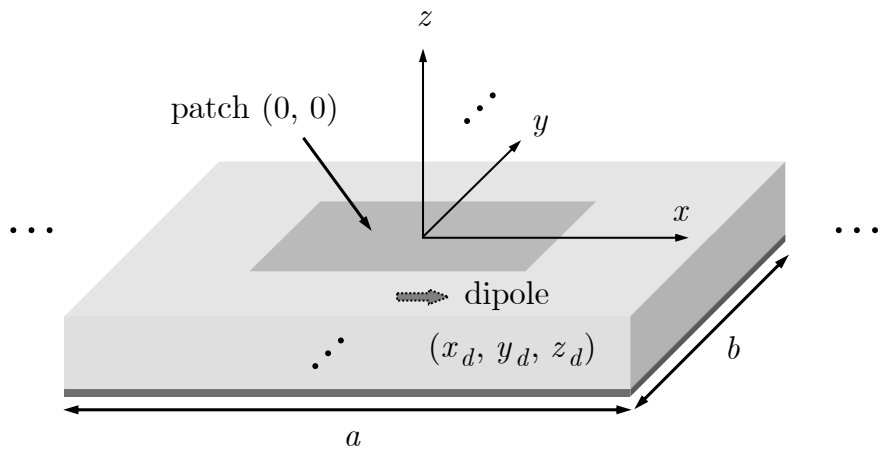

Figure 4.4. A unit cell of the periodic structure excited by periodic dipole excitations as shown in Figure 4.3(b). The unit cell corresponding to patch (0, 0) is shown.

The unit cell that contains the $(0,0)$ patch is shown in Figure 4.4. On the patch surface, the tangential E-field should vanish. For narrow patches ($W \ll L$), the patch

currents will be primarily in the-x direction. When the substrate is air, the E-field due to the x-directed radiation is also mainly polarized in the x-direction. Hence, on patch $(0,0)$, the electric-field-integral-equation (EFIE) becomes

$$-E^{\infty}_{x,\text{patch}} = E^{\infty}_{x,\text{dipole}}. \tag{4.2}$$

The periodic spectral-domain MoM is used to find the patch currents of the auxiliary periodic problem. We start from representing the unknown currents in terms of basis functions $B_i(x,y)$, such that

$$J^{\infty}_{sx,\text{patch}}(x,y) = \sum_{i=1}^{\infty} A^{\infty}_{00;i} B_i(x,y), \tag{4.3}$$

where $A^{\infty}_{00;i}$ is the magnitude of the surface current density at the center of the patch $(0,0)$. The basis function $B_i(x,y)$ is chosen as

$$B_i(x,y) = \cos\left(\frac{i\pi x}{L}\right) \cdot \frac{1/\pi}{\sqrt{(W/2)^2 - y^2}}, \tag{4.4}$$

so that the current density vanishes along the shorter edges and approaches infinity along the longer edges. The subscript i accounts for the x-directed sinusoidal variations. The corresponding spectral representation of this basis function is

$$\tilde{B}_i(k_{xp}, k_{yq}) = \frac{i\pi L \left(e^{-jk_{xp}L/2} + \cos(i\pi) e^{jk_{xp}L/2}\right)}{(k_{xp}L)^2 - (i\pi)^2} J_0\left(k_{yq}W/2\right), \tag{4.5}$$

where $J_0(\cdot)$ denotes the Bessel function of zero order. The tilde field $\tilde{\Psi}$ is the spectral counterpart of the spatial field Ψ.

The electric field on a periodic structure due to an x-directed surface current is

given by [96]

$$E_x^{\infty}(x,y,z) = \frac{1}{ab}\sum_{p=-\infty}^{\infty}\sum_{q=-\infty}^{\infty}\tilde{J}_{sx}^{\infty}(k_{xp},k_{yq}\tilde{G}_{xx}(k_{xp},k_{yq};z)e^{-j(k_{xp}x+k_{yq}y)}, \tag{4.6}$$

where a tilde over a variable denotes its spectral-domain counterpart. $\tilde{G}_{xx}$ is the Green's function inside the layer structure (with no patches present). Details regarding calculating the layered-medium Green's function can be found in Appendix D. The double sum for p and q accounts for the infinite number of Floquet modes supported by the periodic structure, having wavenumbers such

$$k_{xp} = k_{x0} + \frac{2\pi p}{a}, \quad k_{yq} = k_{y0} + \frac{2\pi q}{b}. \tag{4.7}$$

Applying a Galerkin testing scheme to Eq. (4.2), the EFIE is discritized into a matrix equation as

$$[Z_{ij}^{\infty}][A_{00;j}^{\infty}] = [R_i^{\infty}]. \tag{4.8}$$

The patch $(0,0)$ current is then solved from $[A_{00;j}^{\infty}] = [Z_{ij}^{\infty}]^{-1}[R_i^{\infty}]$. Details regarding generating the above linear system Eq. (4.8) can be found in Appendix D. It should be noted that although the EFIE is enforced only on the $(0,0)$ patch, it is automatically satisfied on all the other patches, due to the periodic electromagnetic fields.

4.2.3 ASM Integration

Using the phase-delay information of the scanned array, the current density on patch (m,n) in the auxiliary periodic problem is (subscript i is suppressed here and thereafter)

$$A_{mn}^{\infty}(k_{x0},k_{y0}) = A_{00}^{\infty}(k_{x0},k_{y0})e^{-j(k_{x0}ma+k_{y0}nb)}. \tag{4.9}$$

Once the auxiliary periodic solution A_{mn}^{∞} is obtained, one can refer to ASM [Eq. (4.1)] to find the solution under a single dipole excitation, as given by

$$A_{mn}^{\mathrm{ASM}} = \frac{ab}{(2\pi)^2} \int_{-\pi/b}^{\pi/b} \int_{-\pi/a}^{\pi/a} A_{mn}^{\infty}(k_{x0}, k_{y0}) dk_{x0} dk_{y0}, \tag{4.10}$$

where A_{mn}^{ASM} represents the total surface current density sampled at the center of patch (m, n), excited with a single dipole source.

It is observed that $B_i(x, y)$ is an even function of y regardless of i and an even function of x when i is odd, and vice versa. This yields a symmetry in the current density A_{00}^{∞}. The current density A_{00}^{∞} is an even function of k_{y0}, where

$$A_{00}^{\infty}(k_{x0}, -k_{y0}) = A_{00}^{\infty}(k_{x0}, k_{y0}), \tag{4.11}$$

and it can be even or odd depending on the number i of the x-directed basis functions, where

$$\begin{cases} A_{00}^{\infty}(-k_{x0}, k_{y0}) = A_{00}^{\infty}(k_{x0}, k_{y0}), & i \text{ is odd}, \\ A_{00}^{\infty}(-k_{x0}, k_{y0}) = -A_{00}^{\infty}(k_{x0}, k_{y0}), & i \text{ is even}. \end{cases} \tag{4.12}$$

This allows us to integrate over only the first quadrant of the Brillouin zone. Hence the total current density at the center of patch (m, n) from ASM is

$$A_{mn}^{\mathrm{ASM}} = \frac{ab}{\pi^2} \int_{0}^{\pi/b} \int_{0}^{\pi/a} A_{00}^{\infty}(k_{x0}, k_{y0}) \cos(k_{y0} nb) \cdot \begin{cases} \cos(k_{x0} ma) dk_{x0} dk_{y0}, & i \text{ is odd}, \\ -j \sin(k_{x0} ma) dk_{x0} dk_{y0}, & i \text{ is even}. \end{cases} \tag{4.13}$$

There exists an infinite number of branch points, each accounting for the sign

ambiguity of k_{z0pq} for the (p, q)-th space-harmonic, where

$$k_{z0pq} = \pm\sqrt{k_0^2 - k_{xp}^2 - k_{yq}^2}. \tag{4.14}$$

The integrand in Eq. (4.9) is evaluated such that the imaginary part of k_{z0pq} is always negative in order to satisfy the radiation condition as $z \to +\infty$. For an air-substrate structure with no surface-wave poles, the function A_{00}^{∞} is smooth and easy to integrate, as is shown in Figure 4.5.

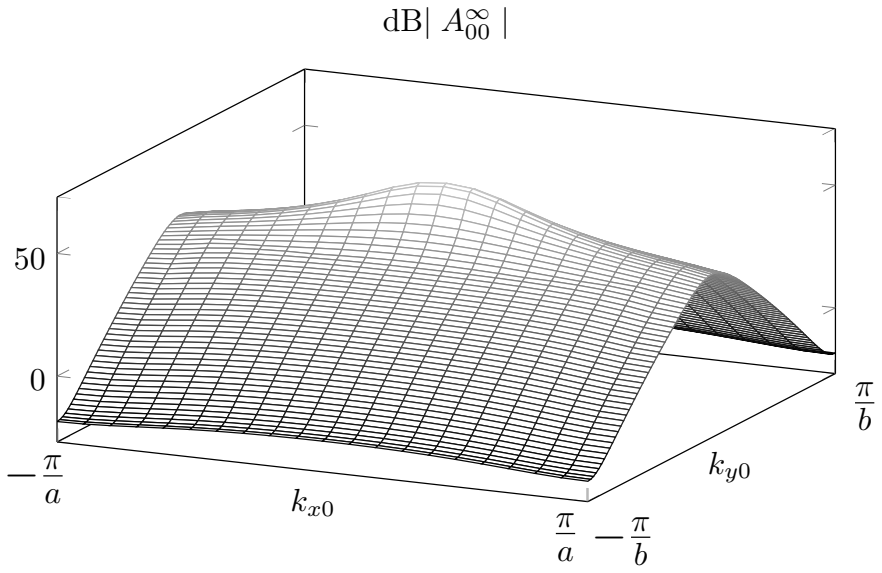

Figure 4.5. The amplitude of the ASM integrand A_{00}^{∞} within the Brillouin zone. For an air-substrate structure with no surface-wave poles, the function A_{00}^{∞} is smooth and easy to integrate.

4.3 Leaky-Wave Currents

4.3.1 Path Unfolding

The leaky-wave current is computed by deforming the original integration path (on the real axis of k_{x0} and k_{y0}) to capture the leaky-wave pole, which requires an infinite path. "Path unfolding" is used to extend the integration path from the bounded Brillouin zone to infinity.

We start from the Fourier expansion

$$A_{00}^{\infty}(k_{x0},k_{y0}) = \sum_{p=-\infty}^{\infty}\sum_{q=-\infty}^{\infty} a_{pq}^{\infty}(k_{x0},k_{y0}) = \sum_{p=-\infty}^{\infty}\sum_{q=-\infty}^{\infty} a_{00}^{\infty}(k_{xp},k_{yq}), \tag{4.15}$$

where a_{00}^{∞} is referred to as the fundamental Floquet function.

It is recognized that the integration interval got shifted right by $2\pi p/a$ after the integration variable is replaced by k_{xp},

$$\begin{aligned} &\int_{-\pi/a}^{\pi/a} a_{00}^{\infty}(k_{xp},k_{y0})dk_{x0} \\ &= \int_{-\pi/a}^{\pi/a} a_{00}^{\infty}(k_{x0}+2\pi p/a,k_{y0})dk_{x0} \\ &= \int_{-\pi/a+2\pi p/a}^{\pi/a+2\pi p/a} a_{00}^{\infty}(k_{x0},k_{y0})dk_{x0}, \end{aligned} \tag{4.16}$$

and a similar interval shift condition holds for k_{y0}.

Combining Eq. (4.10), Eq. (4.15) and Eq. (4.16), the integration path can therefore be extended to infinity, such that

$$A_{mn}^{\mathrm{ASM}} = \frac{ab}{(2\pi)^2}\int_{-\infty}^{\infty}\int_{-\infty}^{\infty} a_{00}^{\infty}(k_{x0},k_{y0})e^{-j(k_{x0}ma+k_{y0}nb)}dk_{x0}dk_{y0}. \tag{4.17}$$

4.3.2 Capturing Leaky-Wave Poles

For any given real-valued k_{y0}, there exist infinite numbers of branch-cuts, each dividing the complex k_{x0}-plane to a top Riemann sheet ($\mathrm{Im}\{k_{z0pq}\} < 0$, proper) and a bottom Riemaan sheet ($\mathrm{Im}\{k_{z0pq}\} > 0$, improper). The branch points of the unfolded

function $a_{mn}^{\infty}(k_{x0}, k_{y0})$ are periodically spaced, such that

$$(k_{xb} + \frac{2\pi p}{a})^2 + (k_{y0} + \frac{2\pi q}{b})^2 = k_0^2. \tag{4.18}$$

The branch-cuts emanating from these branch points are also periodically spaced. When $|k_{y0} + 2\pi q/b| < k_0$, k_{xb} is located on the real axis and the branch cuts are depicted in Figure 4.6. Otherwise, the branch points will be off the real axis and the corresponding branch cuts will lie along the vertical lines $k_{xb} = 2\pi p/a$. The original integration path C along the real axis is also shown.

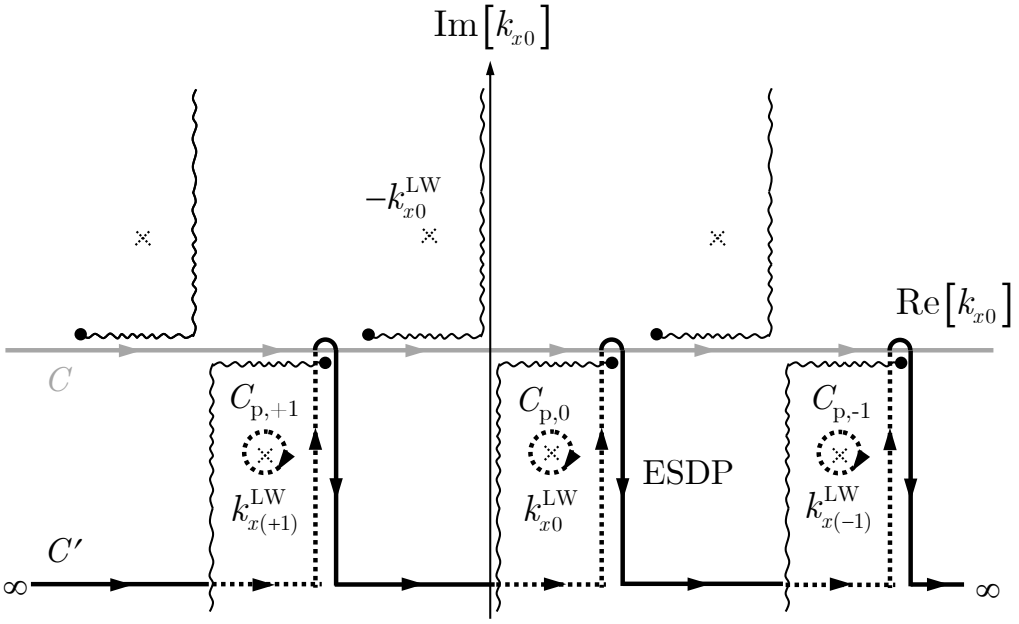

Figure 4.6. Periodically placed singularities and integration paths in the complex k_{x0}-plane. The dotted paths are on the bottom sheet.

In Figure 4.6, all Floquet harmonics with number p and q share a single top sheet, yet they each have an individual bottom sheet. The leaky-wave poles [42] of the integrand, unlike the surface-wave poles, are located on the bottom sheets. Each one bottom sheet has no more than one leaky-wave pole residing on it. These leaky-wave poles are also periodically placed.

Let $k_{\rho 0} = k_0 \sin\zeta$, $k_{x0} = k_{\rho 0}\cos\bar{\phi}$ and $k_{y0} = k_{\rho 0}\sin\bar{\phi}$. The steepest-descent path (SDP) [108] in the ζ-plane is then $\cos(\zeta' - \theta)\cosh\zeta'' = 1$, θ being the observation angle from the z-axis. On the metal patches where $\theta = \pi/2$, it becomes the extreme steepest-descent path (ESDP) [90]. For periodic function a_{mn}^{∞}, there are infinite number of ESDPs placed periodically. Connect these ESDPs at infinity to create a deformed path, and this path is referred to as path C' in Figure 4.6. According to Cauchy's theorem, we have $\int_C = \sum_{i=-\infty}^{\infty}\int_{C_{\mathrm{p},i}} + \int_{C'}$, where $C_{\mathrm{p},i}$ encircles the pole k_{xi}^{LW} clockwise.

Define the leaky-wave current A_{mn}^{LW} on patch (m,n) as the integrals along $C_{\mathrm{p},i}$, which is evaluated using residues,

$$A_{mn}^{\mathrm{LW}} = \frac{ab}{(2\pi)^2}\int_{-\infty}^{\infty}\sum_{i=-\infty}^{\infty}(-2\pi j)\,\mathrm{Res}\,a_{00}^{\infty}(k_{xi}^{\mathrm{LW}}, k_{y0})e^{-j(k_{xi}^{\mathrm{LW}}ma + k_{y0}b)}dk_{y0}. \tag{4.19}$$

Next, we change the order of the summation and the integration, and the result is "folded" back to that using A_{00}^{∞}. Note that going back to use A_{00}^{∞} also folds back the integration path of k_{y0} to within the Brillouin zone ($-\pi/b < k_{y0} < \pi/b$), so that

$$A_{mn}^{\mathrm{LW}} = -\frac{jab}{2\pi}\int_{-\pi/b}^{\pi/b}\mathrm{Res}\,A_{00}^{\infty}(k_{x0}^{\mathrm{LW}}, k_{y0})e^{-j(k_{x0}^{\mathrm{LW}}ma + k_{y0}nb)}dk_{y0}, \tag{4.20}$$

where the residue associated with the pole k_{x0}^{LW} is calculated as

$$\mathrm{Res}\,A_{00}^{\infty}(k_{x0}^{\mathrm{LW}}, k_{y0}) = \lim_{k_{x0}\to k_{x0}^{\mathrm{LW}}}(k_{x0} - k_{x0}^{\mathrm{LW}})A_{00}^{\infty}(k_{x0}, k_{y0}). \tag{4.21}$$

Theoretically, we can exchange the order of the $dk_{x0}dk_{y0}$ integration to obtain an

alternative definition for the leaky-wave current, and that is

$$A_{mn}^{\mathrm{LW}} = -\frac{jab}{2\pi} \int_{-\pi/a}^{\pi/a} \mathrm{Res}\, A_{00}^{\infty}(k_{x0}, k_{y0}^{\mathrm{LW}}) e^{-j(k_{x0}ma + k_{y0}^{\mathrm{LW}} nb)} dk_{x0}. \tag{4.22}$$

However, a certain order is preferable for numerical purposes especially when the observation point is close to the x-axis or the y-axis. For example when $m = 0$, we should use k_{x0} as the outer integration variable and compute the residues of k_{y0}^{LW}.

4.3.3 Leaky-Wave Pole Loci

The definition of leaky-wave current given by Eq. (4.20) requires us to determine the leaky-wave pole k_{x0}^{LW} in the complex k_{x0}-plane. For any given real-valued k_{y0}, the location of the pole $k_{x0}^{\mathrm{LW}}(k_{y0})$ is numerically computed from solving $\det[Z_{mn}^{\infty}(k_{x0}, k_{y0})] = 0$. The same step is used to evaluate $k_{y0}^{\mathrm{LW}}(k_{x0})$. The numerical values are obtained using the root-find algorithm named the secant method.

It is worthwhile to discuss the rule to determine the sign of k_{z0pq}, regarding the branch-cuts appearing in Eq. (4.14). In evaluating $Z_{mn}^{\infty}(k_{x0}, k_{y0})$ for k_{y0} that is continuously moving on the real-axis to search for the pole in the complex k_{x0}-plane, we apply the "continuous tracking" rule for k_{z0pq}. That is, we choose whichever sign of $k_{z0pq}(k_{y0}^{\mathrm{now}})$ is closer to the $k_{z0pq}(k_{y0}^{\mathrm{previous}})$, where k_{y0}^{now} is the continuous change from $k_{y0}^{\mathrm{previous}}$. The purpose of using this rule is to have a continuous loci of poles. Figure 4.7(a) shows the location of the leaky-wave poles as the outer variable changes.

On the other hand, the "physical wave" condition is used when computing a residue. According to [90], [109], a pole does not contribute to a physically-excited wave unless is captured when deforming to the SDP, or in the extreme case the ESDP as in Figure 4.6. This is equivalent to say the physical choice of k_{z0pq} is only improper when it is a fast forward wave; otherwise it is proper.

Figure 4.7(b) shows magnitude of the residues corresponding to the leaky-wave

poles as the outer integration variable moves on the real axis. It is interesting to observe that the region for k_{x0}^{LW} to be physical (has non-zero residue) is $|k_{y0}| < k_0$, and the region for k_{y0}^{LW} to be physical is $|k_{x0}| < 2\pi/a - k_0$. When $k_{y0} > k_0$, no space harmonic is improper and therefore the residue being captured is zero. When $k_{x0} > 2\pi/a - k_0$, on the other hand, $\beta_{y0}^{\mathrm{LW}} \approx 0$ shows a stop-band behavior. Inside this region, we are unable to locate a leaky-wave pole using the secant method ($\det[Z_{mn}^{\infty}(k_{x0}, k_{y0})] \neq 0$), and therefore a zero residue is observed.

Figure 4.8 and Figure 4.9 show the leaky-wave currents using the definition in Eq. (4.20) and in Eq. (4.22). The total current evaluated using ASM Eq. (4.10) is also added for comparison. It can be seen that the leaky-wave currents are approximately the same as the total currents on the centers of the patches along the x-axis (E-plane) and the y-axis (H-plane). This indicates the Fabry Pérot cavity antenna discussed here is a good leaky-wave antenna.

4.3.4 Asymptotic Formulas

We then derive an asymptotic formula for the leaky-wave currents. We start by converting Eq. (4.20) to polar coordinate where $k_{x0}^{\mathrm{LW}} = k_{\rho 0}^{\mathrm{LW}} \cos\bar{\phi}$, $dk_{y0} = k_{\rho 0}^{\mathrm{LW}} \cos\bar{\phi} d\bar{\phi}$ and $\operatorname{Res} A_{00}^{\infty}(k_{x0}^{\mathrm{LW}}, k_{y0}) = \operatorname{Res} A_{00}^{\infty}(k_{\rho 0}^{\mathrm{LW}}, \bar{\phi})/\cos\bar{\phi}$, and then

$$A_{mn}^{\mathrm{LW}} = -\frac{jab}{2\pi} \int_{-\infty}^{\infty} \operatorname{Res} A_{00}^{\infty}(k_{\rho 0}^{\mathrm{LW}}, \bar{\phi}) e^{-jk_{\rho 0}^{\mathrm{LW}} \rho_{mn} \cos(\bar{\phi} - \phi_{mn})} k_{\rho 0}^{\mathrm{LW}} d\bar{\phi}, \tag{4.23}$$

where (ρ_{mn}, ϕ_{mn}) represents the center of patch (m, n). The definition of the angles are depicted in Figure 4.10. In Eq. (4.23) the residue is now calculated in the $k_{\rho 0}$ plane.

It should be noted that the integration interval for $\bar{\phi}$ extends to infinity. This is analogous to the path we use for a simple homogeneous dielectric layer problem. A 0^{th}-order Hankel function of the second kind is involved where $H_0^{(2)}(z) =$

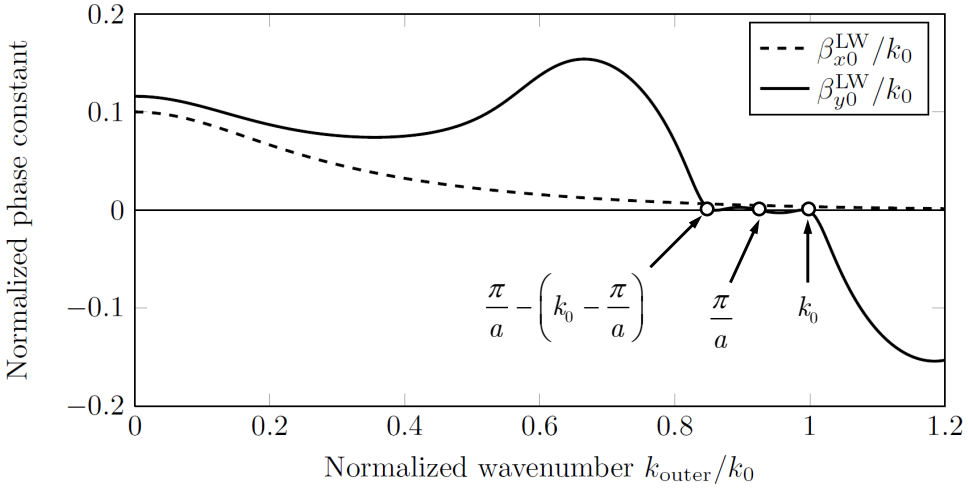

(a) Normalized phase constants of the leaky-wave poles.

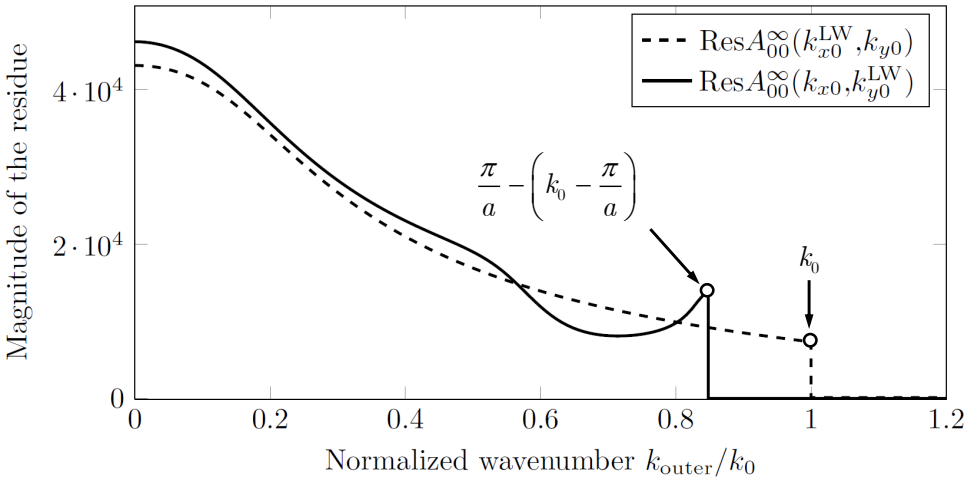

(b) The magnitudes of the residues evaluated with respect to corresponding leaky-wave poles.

Figure 4.7. Leaky-wave poles and corresponding residues.

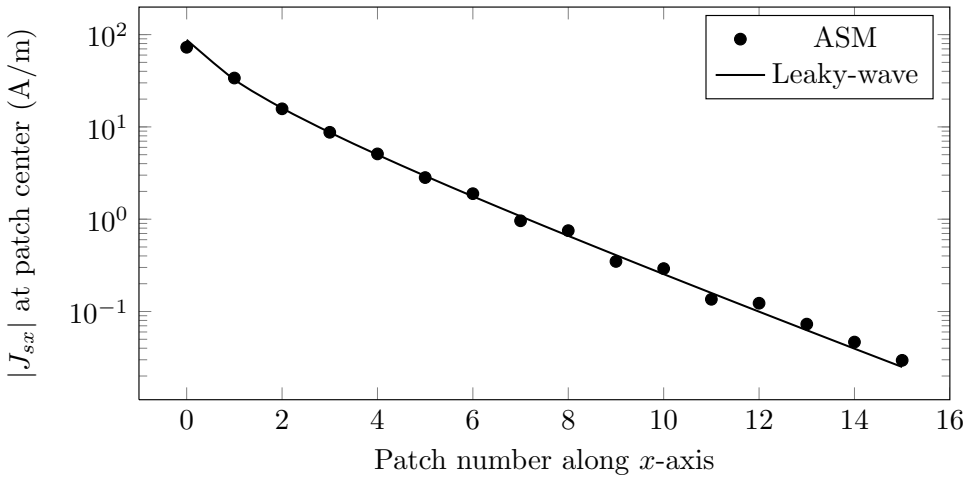

(a) Magnitude.

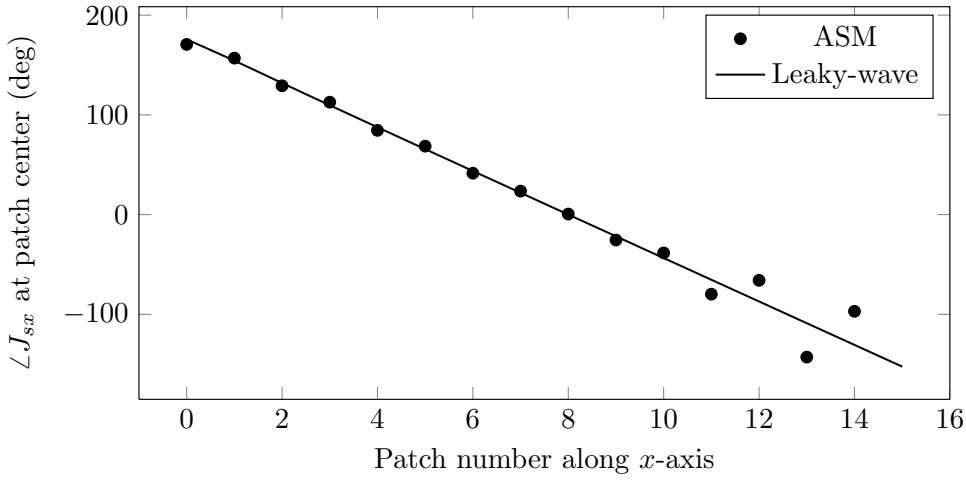

(b) Angle.

Figure 4.8. Comparison of currents at patch centers (along the x-axis): total (ASM) currents vs. leaky-wave currents using Eq. (4.20).

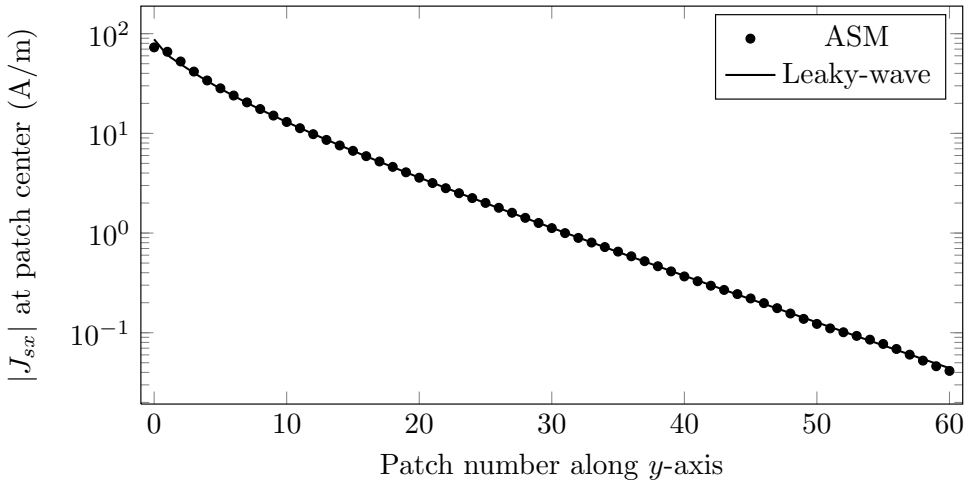

(a) Magnitude.

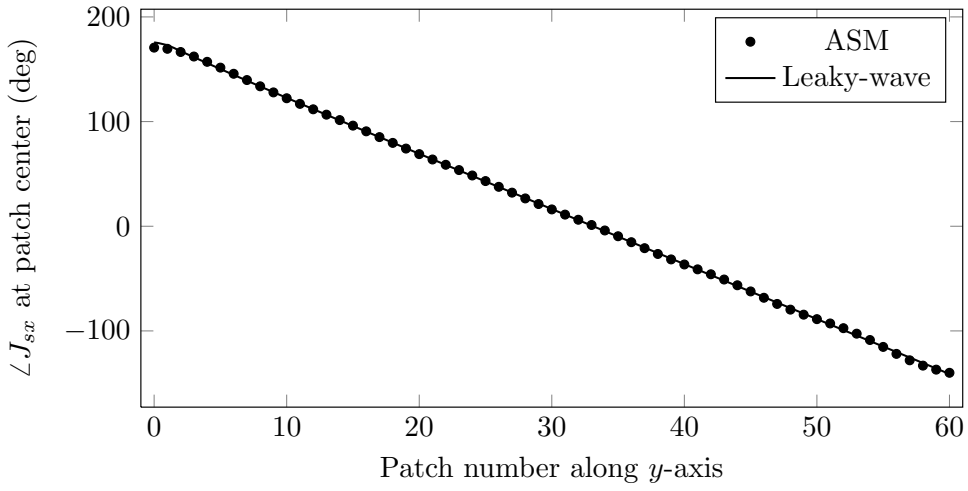

(b) Angle.

Figure 4.9. Comparison of currents at patch centers (along the y-axis): total (ASM) currents vs. leaky-wave currents using Eq. (4.22).

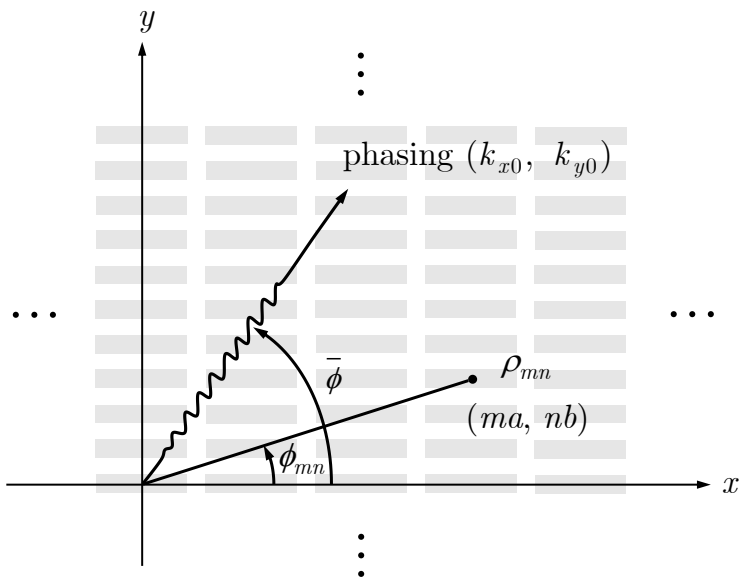

Figure 4.10. The cylindrical coordinate system used to derive the asymptotic formulas.

$(1/\pi)\int_C e^{-jz\cos(\bar{\phi}-\phi_{mn})}d\bar{\phi}$, and C is the path depicted in Figure 4.11. Hence we use the same path for the $\bar{\phi}$-integration in Eq. (4.23) and it is labeled as the "Hankel" path in Figure 4.11.

4.3.4.1 Method of Steepest Descent

An approximate leaky-wave current can be obtained in closed form by asymptotically evaluating the angular integral in closed form for large radial distances using the saddle-point approximation. Write the integral in Eq. (4.23) as

$$A_{mn}^{\mathrm{LW}} = \int_{-\infty}^{\infty} f(\bar{\phi})e^{\Omega g(\bar{\phi})}d\bar{\phi}, \tag{4.24}$$

where

$$\begin{cases} f(\bar{\phi}) = -\frac{jabk_{\rho 0}^{\mathrm{LW}}}{2\pi}\,\mathrm{Res}\,A_{00}^{\infty}(k_{\rho 0}^{\mathrm{LW}},\bar{\phi}), \\ \Omega = |k_{\rho 0}^{\mathrm{LW}}|\rho_{mn}, \\ g(\bar{\phi}) = -je^{j\angle k_{\rho 0}^{\mathrm{LW}}}\cos(\bar{\phi}-\phi_{mn}). \end{cases} \tag{4.25}$$

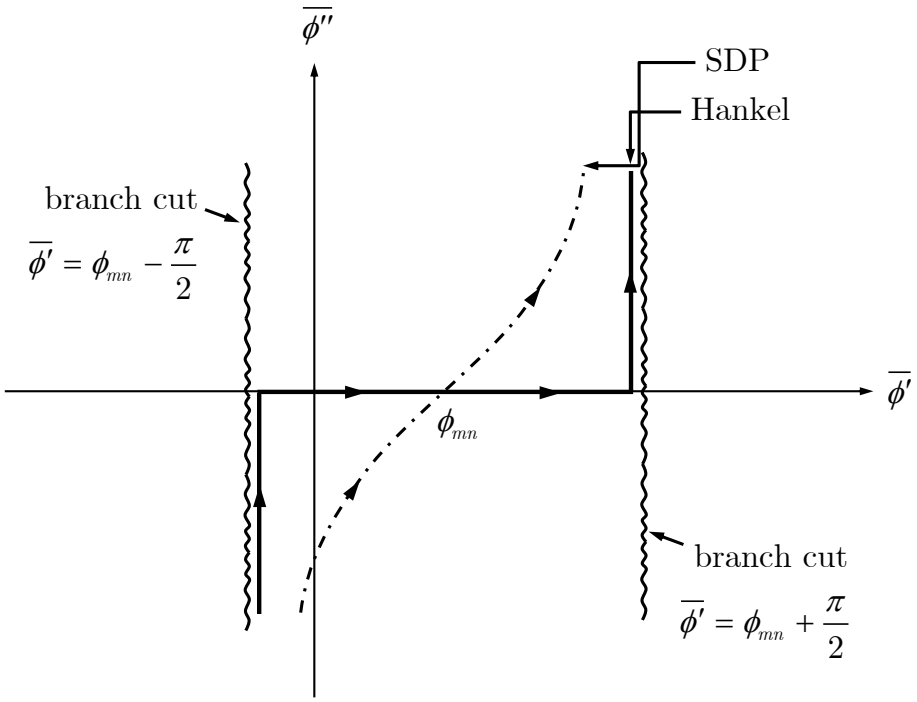

Figure 4.11. Integration path in $\bar{\phi}$-plane to compute the integral Eq. (4.23). It is similar to the integral form of a $H_0^{(2)}$ function and therefore a "Hankel" path is used.

The angular dependency of the components in $f(\bar{\phi})$ are shown in Figure 4.12. It can be observed that both $k_{\rho 0}^{\mathrm{LW}}(\bar{\phi})$ and the corresponding residue $\mathrm{Res}\, A_{00}^{\infty}(k_{\rho 0}^{\mathrm{LW}}, \bar{\phi})$ are slowly varying with respect to the angle $\bar{\phi}$. It is also noted that the only angular dependency is from the $\cos(\bar{\phi} - \phi_{mn})$ term in the $g(\bar{\phi})$ function.

Therefore, the saddle-point is found by setting $g'(\bar{\phi}) = 0$, so that $\bar{\phi}_{\mathrm{SP}} = \phi_{mn}$. The steepest-descent path, as shown in Figure 4.11, passes the the saddle-point with a departure angle

$$\theta_{\mathrm{SDP}} = -\frac{\angle g''(\bar{\phi}_{\mathrm{SP}})}{2} + \frac{\pi}{2} = \frac{\pi}{4} - \frac{\angle k_{\rho 0}^{\mathrm{LW}}}{2}. \tag{4.26}$$

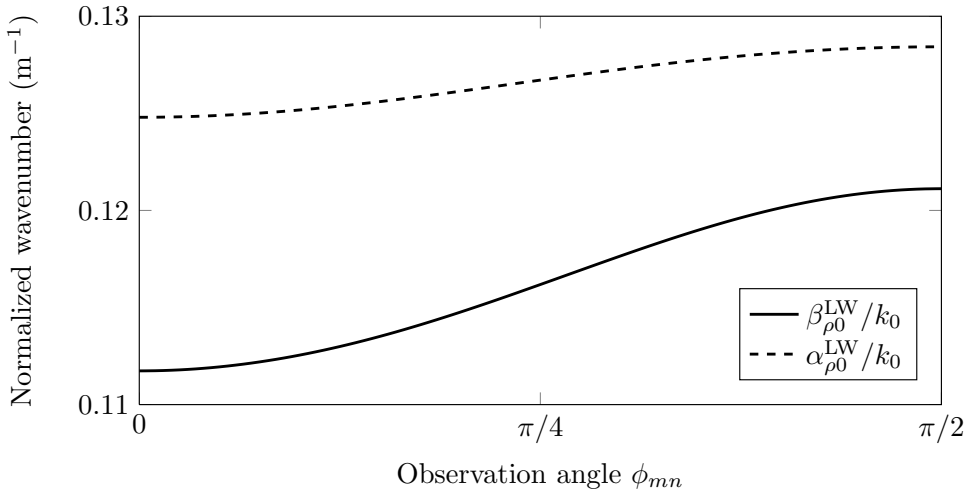

(a) Normalized leaky-wave pole $k_{\rho 0}^{\mathrm{LW}} = \beta_{\rho 0}^{\mathrm{LW}} - j\alpha_{\rho 0}^{\mathrm{LW}}$.

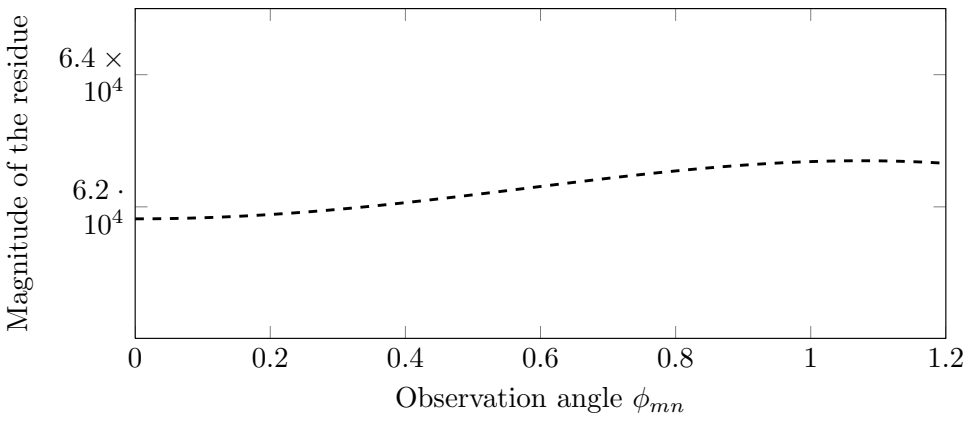

(b) Residue amplitude with respect to the corresponding the leaky-wave poles.

Figure 4.12. Leaky-wave poles and corresponding residues for different observation angles ϕ_{mn}.

From the saddle-point approximation, we have

$$A_{mn}^{\mathrm{LW,SP}} = f(\bar{\phi}_{\mathrm{SP}})e^{\Omega g(\bar{\phi}_{\mathrm{SP}})}\sqrt{\frac{2\pi}{\Omega|g''(\bar{\phi}_{\mathrm{SP}})|}}e^{j\theta_{\mathrm{SDP}}}$$
$$= -\frac{jabk_{\rho 0}^{\mathrm{LW}}}{2\pi}\,\mathrm{Res}\,A_{00}^{\infty}(k_{\rho 0}^{\mathrm{LW}},\phi_{mn})\sqrt{\frac{2\pi j}{k_{\rho 0}^{\mathrm{LW}}\rho_{mn}}}e^{-j(k_{\rho 0}^{\mathrm{LW}}\rho_{mn})}. \tag{4.27}$$

4.3.4.2 Cylindrical Leaky-Wave Propagation

For an x-directed electrical dipole excitation, there will be one TM_x leaky wave propagating on the layered structure. In addition, the patch current mainly flows in the x-direction for narrow patches. Hence we can derive a CAD formula for J_x as

$$A_{mn}^{\mathrm{LW,CAD}} = A^{\mathrm{TM}}(\phi_{mn})H_0^{(2)}(k_{\rho 0}^{\mathrm{TM}}\rho_{mn}), \tag{4.28}$$

where $H_0^{(2)}(\cdot)$ is the zero-order Hankel function of the second kind and

$$k_{\rho 0}^{\mathrm{TM}} = k_{\rho 0}^{\mathrm{LW}}(\phi_{mn}). \tag{4.29}$$

Examining the asymptotic expression for the Hankel function with large argument, and comparing that with the saddle-point asymptotic Eq. (4.27), we can obtain the formula for the TM_x leaky-wave amplitude as

$$A^{\mathrm{TM}} = -\frac{jab}{2}k_{\rho 0}^{\mathrm{TM}}\,\mathrm{Res}\,A_{00}^{\infty}(k_{\rho 0}^{\mathrm{TM}},\phi_{mn}). \tag{4.30}$$

A comparison of the asymptotic formulas is given in Figure 4.13. The *exact* leaky-wave currents obtained from numerically calculating the $\bar{\phi}$-integration Eq. (4.23) along the "Hankel" path (as given in Figure 4.11) is added for comparison. It is observed that the asymptotic formulas are accurate when the observation point is far from the source. This is because the field on the aperture just above the PRS is

dominated by the leaky-wave fields, and hence the leaky-wave aperture field is a good predictor of the far-field properties. The saddle-point approximation is able to give accurate result even when the observation point is close to the source, e.g. on patch $(1, 0)$.

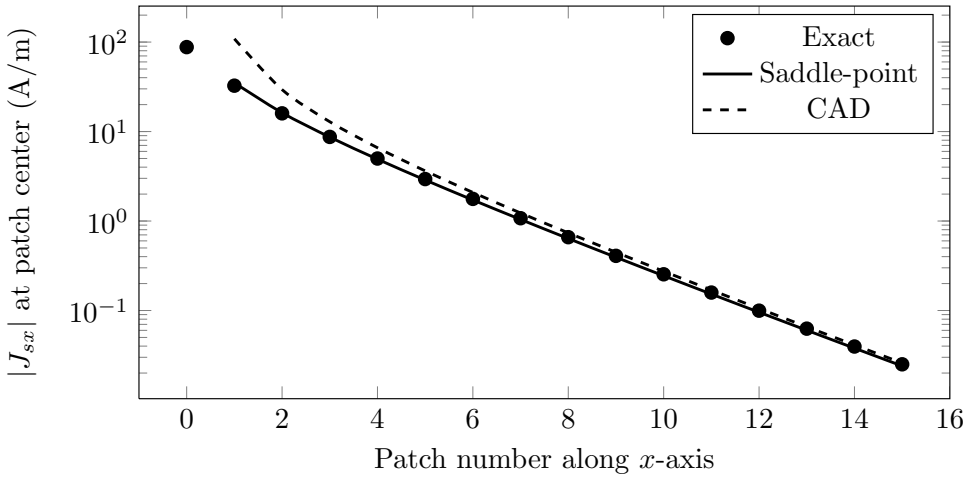

Figure 4.13. Leaky-wave currents using asymptotic formulas Eq. (4.27) and Eq. (4.28). The "exact" leaky-wave current is given by Eq. (4.23) through numerical integration with respect to $\bar{\phi}$.

4.4 Radiation Pattern Calculation

The total radiation from the Fabry-Pérot cavity antenna consists of that from the patch currents and the source dipole embedded in the substrate. The dipole radiation can be found using the reciprocity theorem, where a **p**-directed testing dipole (Il) is introduced in the far-field region. From reciprocity, the far-field p-component of electric field sampled at the testing dipole location is equal to the x-component of that sampled at the source dipole location, due to the radiation from the testing dipole, which can be approximated by a plane-wave incidence. This is expressed as

$$E^{\mathrm{FF}}_{p,\mathrm{dipole}} = E^{\mathrm{inc}}_{x0}(1+\Gamma)e^{j(k_{x0}x_d+k_{y0}y_d)} \cdot \frac{\sin(k^{\mathrm{PW}}_{z1}(z_d+h))}{\sin(k^{\mathrm{PW}}_{z1}h)}, \tag{4.31}$$

where $k_{z1}^{\mathrm{PW}} = \sqrt{k_1^2 - k_{x0}^2 - k_{y0}^2}$. E_{x0}^{inc} is the incoming plane-wave from the testing dipole and is sampled at the origin (the center of the (0, 0) patch),

$$E_{x0}^{\mathrm{inc}} = -\frac{j\omega\mu(Il)}{4\pi r^2}(\hat{\mathbf{p}} \cdot \hat{\mathbf{x}}), \tag{4.32}$$

and the reflection coefficient Γ is that of the layered structure (in the absence of patches), and this is given by Eq. (D.5).

The radiation due to the patch currents can be computed using different methods, namely reciprocity and an array factor approach. The reciprocity approach allows the patch array structure to be infinite and periodic, while the array factor approach requires a finite-size array. For a fair comparison, the patch array size should be large enough to model an infinite periodic structure.

4.4.1 Reciprocity

The radiation pattern for an infinite periodic patch array excited with a single horizontal dipole can be computed using the reciprocity theorem, where a unit-strength "testing" dipole (Il) is introduced in the far-field and the radiating fields from this testing dipole are observed at the original excitation location.

Consider a $\hat{\mathbf{p}}$-directed testing dipole radiating in the far-field region; omitting the details, the EFIE becomes

$$\sum_{n=1}^{\infty} Z_{ij}^{\infty} A_i^{\mathrm{PW}} = E_{x0}^{\mathrm{inc}}(1+\Gamma)\tilde{B}_i(-k_{x0}, -k_{y0}), \tag{4.33}$$

where Z_{ij}^{∞} is the same as in the auxiliary periodic phased-array problem, and A_i^{PW} gives the patch current density due to plane-wave incidence. After solving for A_i^{PW}

the radiation from the patches is

$$E_{p,\text{patch}}^{\text{FF,reciprocity}} = \frac{1}{ab}\sum_{i=0}^{\infty} A_i^{\text{PW}} \sum_{p=-\infty}^{\infty}\sum_{q=-\infty}^{\infty} \tilde{G}_{xx}(k_{xp}, k_{yq}; z_d) \cdot \tilde{B}_i(k_{xp}, k_{yq}) e^{-j(k_{xp}x_d + k_{yq}y_d)}. \tag{4.34}$$

The radiation pattern calculated using reciprocity is shown in Figure 4.14. Five basis functions are used in order to describe the x-variation of the current density on each patch. The $E_{p,\text{patch}}^{\text{FF,reciprocity}}$ is evaluated at different frequencies. As is seen from Figure 4.12 where $\beta_{\rho 0}^{\text{LW}} \approx \alpha_{\rho 0}^{\text{LW}}$, the power radiated at broadside is maximized. This is seen in the pattern plot in Figure 4.14, from which we observe the broadside power reaches the maximum at the resonance frequency $f_0 = 12$ GHz.

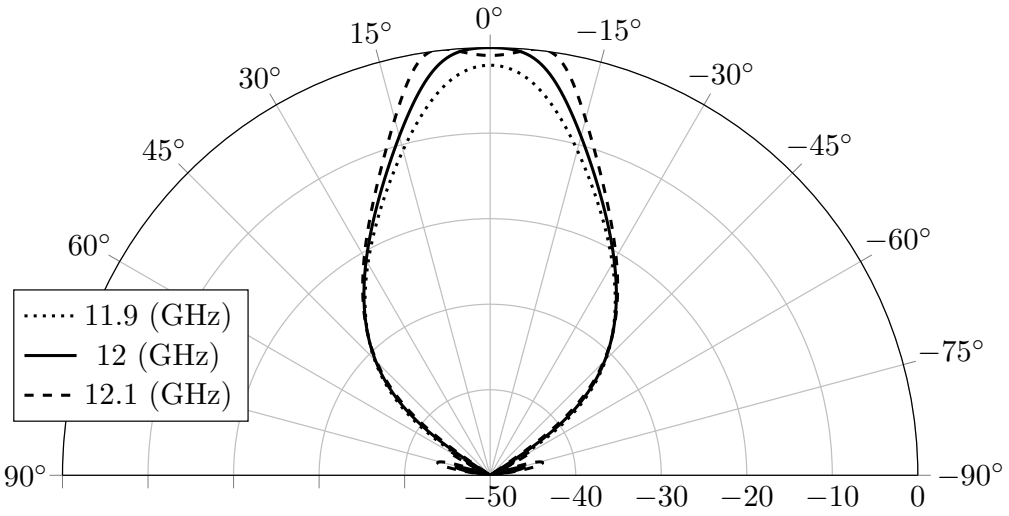

Figure 4.14. The radiation pattern using reciprocity. The far-field values are evaluated at different frequencies. The antenna is optimized to deliver maximum power density at broadside at 12 GHz.

4.4.2 Array Factor

An array factor can also be used to find the radiation from the patch currents. For the i-th order basis function, the array factor is

$$(\mathrm{AF})_i = \sum_{m=-\infty}^{\infty} \sum_{n=-\infty}^{\infty} A_{mn;i} e^{j(k_{x0}ma + k_{y0}nb)}, \tag{4.35}$$

where $A_{mn;i}$ is the amplitude of the i-th order surface current density sampled at the center of patch (m, n). The numerical value of $A_{mn,i}$ is obtained using ASM as in Eq. (4.10).

The element pattern is simply that from a single rectangular patch antenna, where

$$E^{\mathrm{FF}}_{i,p,\mathrm{element}} = E^{\mathrm{inc}}_{x0}(1+\Gamma)\tilde{B}_i(k_{x0}, k_{y0}). \tag{4.36}$$

The total radiation from the patch currents using array factor is then

$$E^{\mathrm{FF,AF}}_{p,\mathrm{patch}} = \sum_{i=1}^{\infty} E^{\mathrm{FF}}_{i,p,\mathrm{element}}(\mathrm{AF})_i. \tag{4.37}$$

The radiation pattern using reciprocity and the array-factor are compared in Figure 4.15. In the array-factor approach, a 31×121 patch array is used to represent an infinite array. Here five basis functions on each patch are used in both methods. It can be seen that the two patterns agree with each other, which demonstrates the accuracy of the patch currents computed using ASM.

4.4.3 Cylindrical Leaky-Wave Radiation

There is only one leaky wave (TM_x) propagating on the air-substrate Fabry Pérot antenna. However, we can decompose this TM_x wave into a TM_z wave and a TE_z wave. The far-field pattern due to cylindrical leaky waves (a TE_z and a TM_z leaky-wave) radiation can be found in [102], where CAD formulas for the radiation pattern are

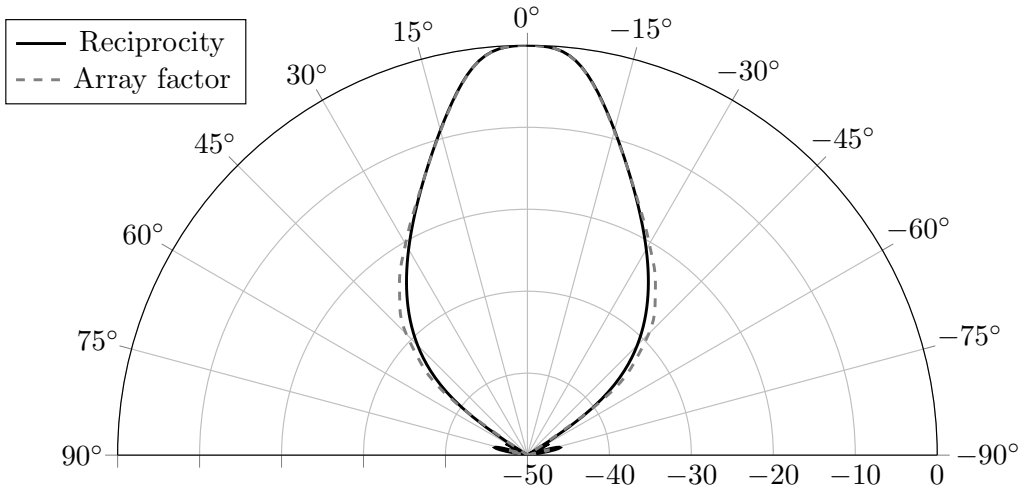

(a) E-plane pattern.

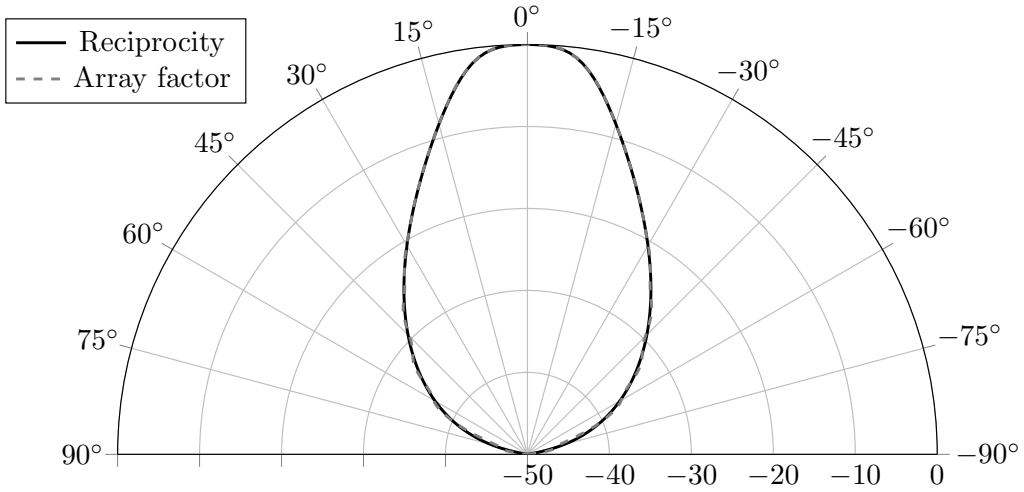

(b) H-plane pattern.

Figure 4.15. The comparison of radiation patterns: reciprocity vs. array factor. In the array factor calculation, the patch currents are obtained using ASM (Eq. (4.10))

given as

$$\begin{cases} E_\theta = R(r)\cos\phi\cos\theta[A^{\mathrm{TM}}P^{(1)}(k_{\rho 0}^{\mathrm{TM}},\theta) + A^{\mathrm{TE}}C(k_{\rho 0}^{\mathrm{TE}},\theta)], \\ E_\phi = -R(r)\sin\phi[A^{\mathrm{TM}}C(k_{\rho 0}^{\mathrm{TM}},\theta) + A^{\mathrm{TE}}P^{(1)}[k_{\rho 0}^{\mathrm{TE}},\theta)], \end{cases} \tag{4.38}$$

where the leaky-wave amplitudes A^{T} and wavenumbers $k_{\rho 0}^{\mathrm{T}}$ are extracted as we compute the CAD leaky-wave current, using equations similar to Eq. (4.29) and Eq. (4.30). $R(r)$ accounts for the spherical-wave propagation and is

$$R(r) = -\frac{j\omega\mu_0}{4\pi r}e^{-jk_0 r}. \tag{4.39}$$

For infinite structure, the auxiliary functions are calculated by

$$\begin{cases} P^{(1)}(k_{\rho 0},\theta) = \frac{2j}{k_{\rho 0}} - \frac{4jk_{\rho 0}}{k_{\rho 0}^2 - k_0^2\sin^2\theta}, \\ C(k_{\rho 0},\theta) = \frac{-2j}{k_{\rho 0}}. \end{cases} \tag{4.40}$$

Figure 4.16 shows the comparison of the leaky-wave radiation patterns. The results obtained from the array-factor approach are compared to those using the CAD formula Eq. (4.38). In the array factor approach, the leaky-wave currents, as given by Eq. (4.23), are taken as the patch currents. The radiation is sum of the leaky-wave currents and the dipole source, and is therefore labeled as "LW + dipole" in Figure 4.16. The results of using the array factor approach but based on the total currents calculated from ASM is also added, and is labeled as "ASM + dipole".

It is observed that the patterns agrees with each other near broadside, which proves that the proposed design is a good leaky-wave antenna, where the leaky-wave dominance is observed. However, the results using the leaky-wave currents to compute the array factor is more accurate than those using the CAD formula Eq. (4.38), especially near the end-fire region in the H-plane.

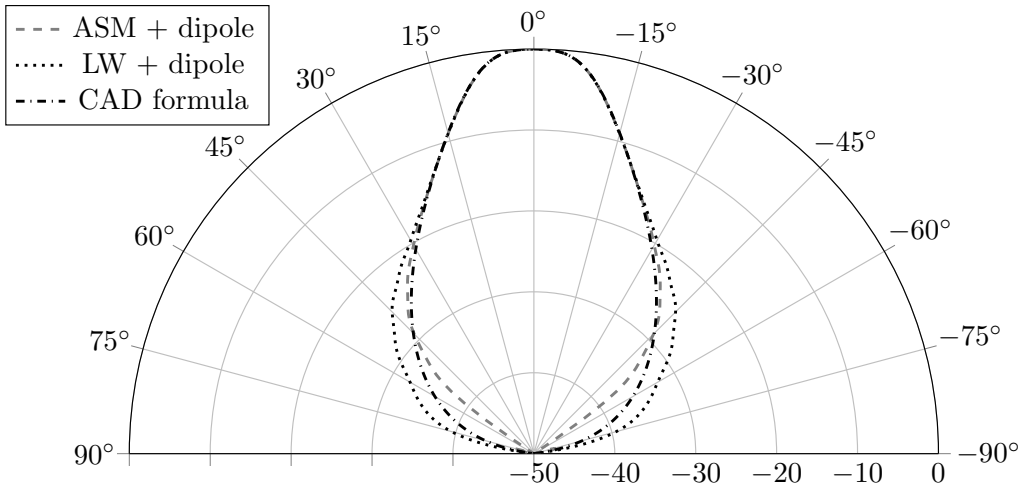

(a) E-plane pattern.

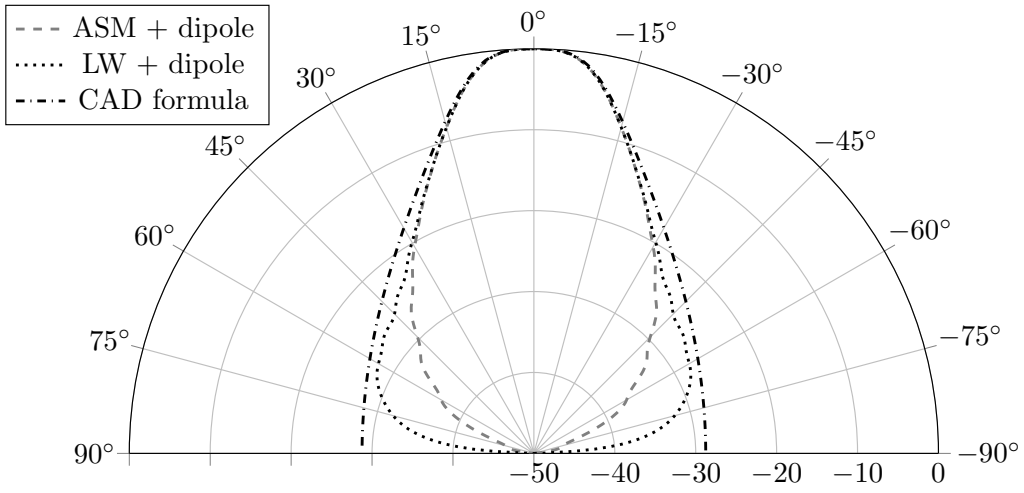

(b) H-plane pattern.

Figure 4.16. The comparison of radiation patterns. The total currents (Eq. (4.10)) and the leaky-wave currents (Eq. (4.20)) are used to compute the array factor. The CAD formula results are obtained using Eq. (4.38).

4.5 Finite-Size Array

4.5.1 Truncation Effects

For a finite-size patch antenna array, the "natural truncation" refers to a structure where the antenna array is taken as a finite size while the layered medium extends to infinity. In the case of the design considered in this chapter with an air-substrate, this natural truncated antenna is simply a finite-size patch array over an infinite ground plane. The current densities of a large antenna array (121 patches in the E-plane, 31 patches in the H-plane) is obtained using Ansys Designer and the results are shown in Figure 4.17.

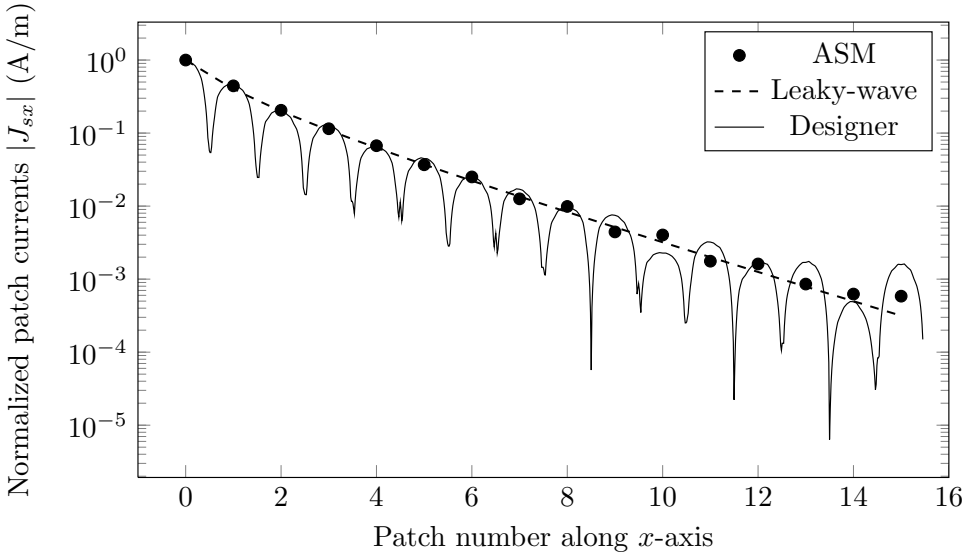

Figure 4.17. The normalized current density $|J_{sx}|$ for a large antenna array. The finite array simulated in Ansys Designer has the size of 121×31 patches.

Assume "ideal absorber" are put surrounding a finite-size patch array as shown in Figure 4.18. The "ideal absorber" is a material that is assumed to absorb all incoming waves and and thus eliminate reflections from the array boundary. Under this assumption, the patch currents should stay the same as for the infinite periodic patch array. These are referred to as "ASM" and "leaky-wave" in Figure 4.17, accounting for the total current and leaky-wave current, respectively. It can be seen

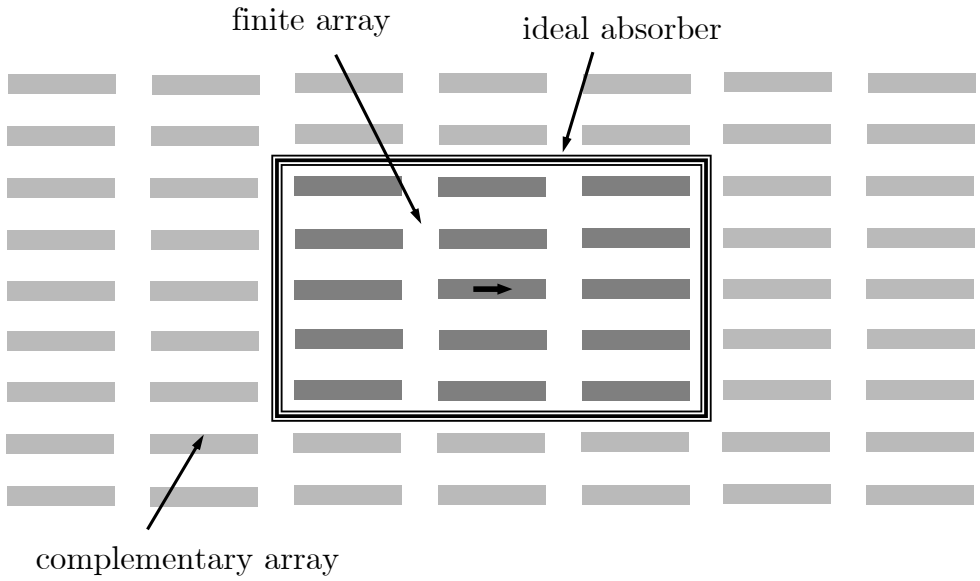

Figure 4.18. A finite-size patch antenna array terminated with an ideal absorber. The currents on the finite array remains the same as those on an infinite array.

that the results agrees reasonably well even at the array boundaries. This is because the array is large enough that the leaky-wave decays very fast and becomes negligible before it reaches the array boundaries. A weak reflection from the array boundary in the E-plane is seen in Figure 4.17 for the results from Ansys Designer.

4.5.2 Radiation Pattern of a Finite Array

The patch currents obtained from ASM can be used to generate the radiation pattern of a finite patch array. Two methods are considered here, namely the addition method ("ASM + dipole"), and the subtraction method. In both methods, the patch currents for the finite-size array are treated the same as those from an infinite patch array.

4.5.2.1 Addition Method

The addition method uses the array factor by summing up the patch current contributions (inside the absorber), plus the radiation from the embedded dipole source. The radiation patterns obtained using this approach is shown in Figure 4.19,

for different sizes of the antenna patch arrays. The pattern for an naturally-truncated array (simulated using Ansys Designer) is added for comparison. It is expected that the "ideal absorber" assumption is accurate especially when the array size is large, yet it is still good to give reasonably results for small arrays.

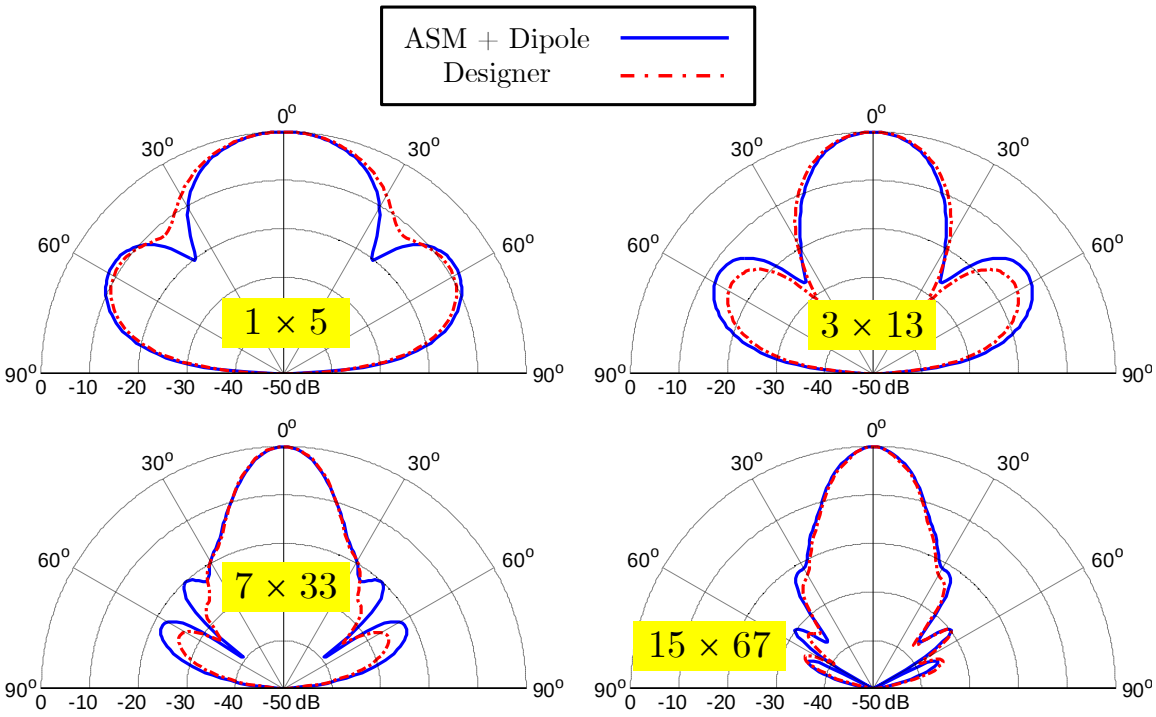

Figure 4.19. The radiation pattern of a finite-size array: addition method vs. Designer. The addition method has the "ideal absorber" assumption.

4.5.2.2 Subtraction Method

In the subtraction approach, a complimentary structure (infinite minus finite-size array) is considered. This complementary structure is shown in Figure 4.18 as the array outside the absorber and extends to infinity. Due to leaky-wave dominance, the currents on the complementary array can be predicted using the leaky-wave formula, either in the strict form, as in Eq. (4.23) or the asymptotic form, as in Eq. (4.27) and Eq. (4.30). The pattern for the finite array is then computed by subtracting the fields radiated by the complementary array from the infinite array, whose pattern is obtained using reciprocity.

A comparison of the radiation patterns computed using the addition method and the subtraction method is shown in Figure 4.20. The results from two methods converge when the antenna array size becomes larger.

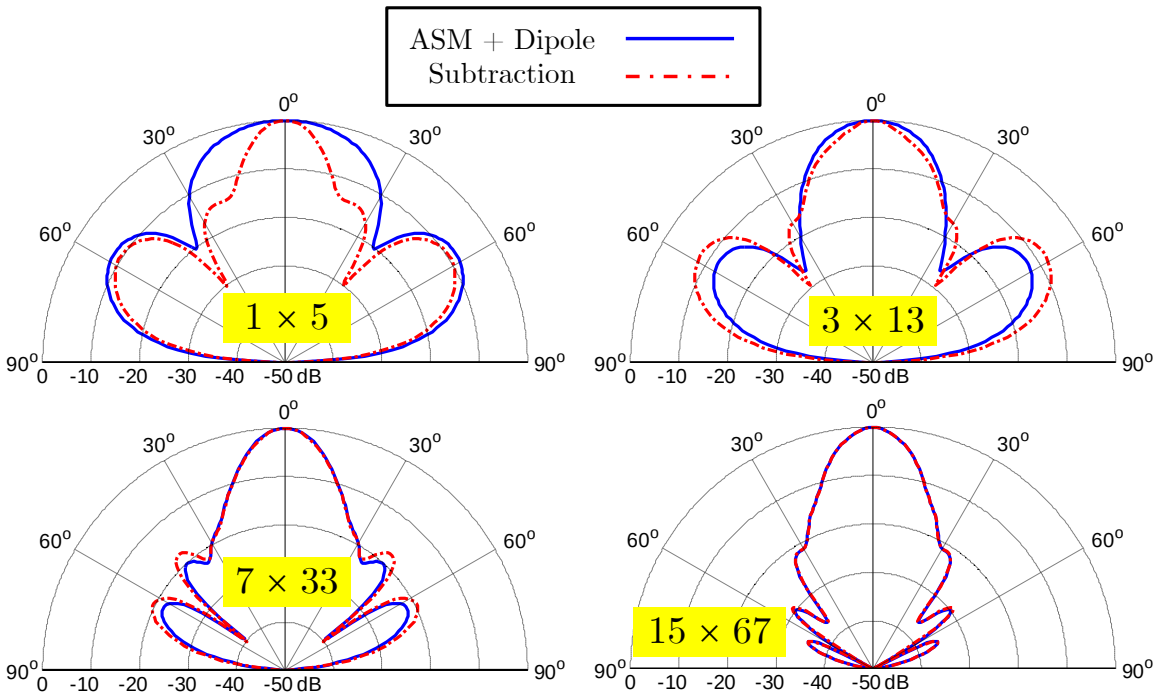

Figure 4.20. The radiation pattern of a finite-size array: addition method vs. subtraction method.

4.6 Conclusions

In this chapter, a Fabry Pérot cavity antenna with a two-dimensional patch array implementation was studied. The antenna surface current density was computed numerically using the array scanning method (ASM).

Starting from the ASM formulation, we proposed the definition of leaky-wave current as the contour integral surrounding the leaky-wave poles, which can be calculated using a residue integration. The extracted leaky-wave current was then compared with the total current calculated from ASM. A leaky-wave dominance was observed. We then derived two asymptotic formulas for the leaky-wave currents using the method of steepest descent and using the expected asymptotic form of a cylindrical

wave.

We also performed a leaky-wave study on a finite-size leaky-wave antenna. An ideal absorber was assumed to be placed at the array boundary to absorb the reflections. The radiation patterns were calculated using the addition method and the subtraction method. The patterns using the ideal absorber assumption were compared to that using a natural truncation from a full-wave simulation.

Chapter 5

Conclusions

5.1 Conclusions

In this dissertation, three advanced electromagnetic models were proposed. Examples presented in this dissertation include (a) an analysis of the conductor surface roughness effects on stripline transmission lines, (b) a model to estimate the radiation and coupling mechanism of massively packed vertical interconnects (vias) and (c) a leaky-wave study of a Fabry-Pérot resonant cavity antenna using a two-dimensional patch array. These structures are shown in Figure 5.1.

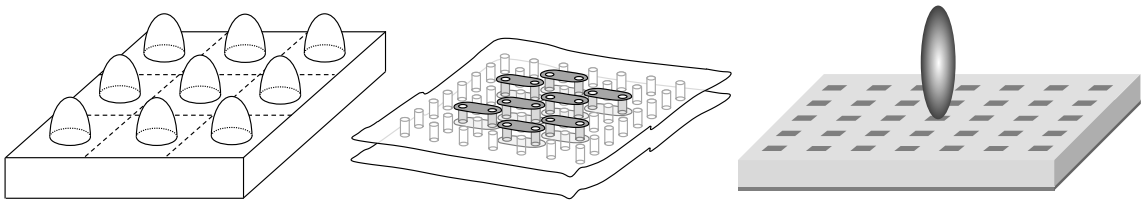

(a) (b) (c)

Figure 5.1. Structures considered in this dissertation: (a) a rough-surface conductor, (b) a via array and (c) a 2-D leaky-wave antenna.

The first part of the dissertation was the study of the conductor surface roughness effects, as discussed in Chapter 2. An equivalent rough surface impedance was extracted using the periodic finite-element analysis. Two structures were analyzed to extract this equivalent surface impedance, namely a long waveguide and an infinite periodic cavity. This rough surface impedance was then used for the modification of the transmission line per-unit-length parameters. The proposed model was validated using both full-wave simulations and measurements.

The second part of the dissertation presented a semi-analytical model for massively-coupled vias with arbitrarily-shaped antipads as proposed in Chapter 3. A novel

model based on the reciprocity theorem was proposed. The use of reciprocity was seen to greatly improve the efficiency, due to the fast-converging mode-matching calculation. The proposed model was validated using full-wave simulations.

The third part of the dissertation was the study of a Fabry Pérot cavity antenna with a 2-D patch array implementation in Chapter 4. The current density of the antenna was calculated using the array scanning method. Based on this, the leaky-wave contribution was extracted using a residue integration. In addition, the radiation properties of a large finite-size array (truncation effects) was evaluated. The numerical results were validated using reciprocity (assuming infinite periodic structure) and also full-wave simulations.

5.2 Future Works

5.2.1 Conductor Surface Roughness Effects

In the proposed approach to compute the fundamental Floquet wavenumber k_{z0}, the constant-β eigenmode solver is used, where the eigenvalues are complex resonant frequencies $f = f' + jf''$. It is suggested we apply analytic continuation, where the $f - \beta$ relation is first obtained assuming complex f through a polynomial curve-fit, and the obtained polynomial representation of f is applied to a real-valued f' to calculate a complex k_{z0}.

Another possible approach is to directly solve the eigenmode problem with eigenvalue $\lambda = e^{-jk_{z0}\Lambda_r}$, and a preliminary discussion of this idea is given in Appendix A.

5.2.2 Via Modeling

In this dissertation, the parallel-plates modeling the ground-plane pairs were assumed to have an infinite horizontal extent. However, we only have finite-size parallel plates in practical PCBs and the infinite-plate assumption becomes less accurate when the via barrels are located close to the plate boundaries. In order to model the effects of a finite ground plane, we can use the PMC boundary conditions at

the plate boundaries, where the magnetic current densities on the PMC walls become unknown and are integrated into the mode-matching calculations.

A more accurate modeling methodology, instead of using PMC walls, would be to enforce an equivalent surface impedance boundary condition for the finite parallel-plates. Since the dominant transmission mode is the 0^{th}-order vertical mode, we can estimate the reflection coefficient of this mode at a finite parallel-plate boundary, from which an equivalent surface impedance can be extracted. Hence, both electric surface current and magnetic surface current unknowns are associated with the parallel-plate side walls and are related by this surface impedance boundary condition.

References

[1] D. G. Kam, M. B. Ritter, T. J. Beukema, J. F. Bulzacchelli, P. K. Pepeljugoski, Y. H. Kwark, L. Shan, X. Gu, C. W. Baks, R. A. John, G. Hougham, C. Schuster, R. Rimolo-Donadio, and B. Wu, "Is 25 Gb/s on-board signaling viable?" *IEEE Trans. Adv. Packag.*, vol. 32, no. 5, pp. 328–344, May 2009.

[2] T. Beukema, M. Sorna, K. Selander, S. Zier, B. L. Ji, P. Murfet, J. Mason, S. Member, W. Rhee, H. Ainspan, B. Parker, and M. Beakes, "A 6.4-Gb/s CMOS SerDes core with feed-forward and decision-feedback equalization," *IEEE J. Solid-State Circuits*, vol. 40, no. 12, pp. 2633–2645, Dec. 2005.

[3] J. F. Buckwalter, M. Meghelli, D. J. Friedman, and A. Hajimiri, "Phase and amplitude pre-emphasis techniques for low-power serial links," *IEEE J. Solid-State Circuits*, vol. 41, no. 6, pp. 1391–1399, Jun. 2006.

[4] R. F. Harrington, Time-Harmonic Electromagnetic Fields. New York: Wiley, 2001.

[5] D. M. Pozar, Microwave Engineering, 4th ed. New York: Wiley, 1997, ch. 3, pp. 153–154.

[6] C. R. Paul, Analysis of Multiconductor Transmission Lines, 2nd ed. New York: Wiley, 2007.

[7] S. H. Hall, Advanced Signal Integrity for High-Speed Digital Designs. New York: Wiley, 2009, pp. 434–441.

[8] S. Hinaga, M. Y. Koledintseva, P. K. R. Anmula, and J. L. Drewniak, *Effect of conductor surface roughness upon measured loss and extracted values of PCB laminate material dissipation factor*. [Online]. Available: http://web.mst.edu/

~marinak/files/My_publications/Papers/S_Hinaga-IPC2009_Formatted.pdf.

[9] G. Brist, S. Hall, S. Clouser, and T. Liang, "Non-classical conductor losses due to copper foil roughness and treatment," in *APEX IPC Print. Circ. Exp. Des. Summi.*, 2005, pp. 1–11.

[10] H. Braunisch, X. Gu, A. Camacho-Bragado, and L. Tsang, "Off-chip rough-metal-surface propagation loss modeling and correlation with measurements," in *Proc. Electron. Comp. Tech. Conf.*, Reno, 2007, pp. 785–791.

[11] E. Hammerstad and O. Jensen, "Accurate models for microstrip computer-aided design," in *IEEE MTT Intl. Microw. Symp. (IMS) Dig.*, vol. 1, Washington: IEEE, 1980, pp. 407–409.

[12] A. E. Sanderson, Effect of surface roughness on propagation of the TEM mode. Cambridge: Academic Press, 1971, pp. 1–57.

[13] X. Gu, L. Tsang, and H. Braunisch, "Modeling effects of random rough interface on power absorption between dielectric and conductive medium in 3-D problem," *IEEE Trans. Microw. Theory Techn.*, vol. 55, pp. 511–517, Mar. 2007.

[14] C. L. Holloway and E. F. Kuester, "Impedance-type boundary conditions for a periodic interface between a dielectric and a highly conducting medium," *IEEE Trans. Antennas Propag.*, vol. 48, pp. 1660–1672, Oct. 2000.

[15] S. Hall, S. G. Pytel, P. G. Huray, D. Hua, A. Moonshiram, G. A. Brist, and E. Sijercic, "Multigigahertz causal transmission line modeling methodology using a 3-D hemispherical surface roughness approach," *IEEE Trans. Microw. Theory Techn.*, vol. 55, pp. 2614–2624, Dec. 2007.

[16] P. G. Huray, S. Hall, S. Pytel, F. Oluwafemi, R. Mellitz, and D. Hua, "Fundamentals of a 3-D snowball model for surface roughness power losses," in *Signal Prop. Interconnects*, IEEE, May 2007, pp. 121–124.

[17] S. Savastiouk, "Moore's Law – the z-dimension: a decade later," *Solid State Technol.*, p. 36, 2008.

[18] S. Savastiouk, "Moore's Law – the z-dimension," *Solid State Technol.*, pp. 83–84, Jan. 2000.

[19] Y.-J. Zhang, J. Fan, and G. Selli, "Analytical evaluation of via-plate capacitance for multilayer printed circuit boards and packages," *IEEE Trans. Microw. Theory Techn.*, vol. 56, no. 9, pp. 2118–2128, Sep. 2008.

[20] Z. Guo and G. G. Pan, "On simplified fast modal analysis for through silicon vias in layered media based upon full-wave solutions," *IEEE Trans. Adv. Packag.*, vol. 33, no. 5, pp. 517–523, May 2010.

[21] E. Laermans, J. D. Geest, D. D. Zutter, F. Olyslager, S. Sercu, and D. Morlion, "Modeling complex via hole structures," *IEEE Trans. Adv. Packag.*, vol. 25, no. 2, pp. 206–214, May 2002.

[22] C. Schuster, Y. Kwark, G. Selli, and P. Muthana, "Developing a physical model for vias - part I," in *DesignCon*, Santa Clara, 2006, pp. 1–24.

[23] G. Selli, C. Schuster, Y. H. Kwark, M. B. Ritter, and J. L. Drewniak, "Developing a physical model for vias - part II : coupled and ground return vias," in *DesignCon*, Santa Clara, 2007, pp. 1–22.

[24] T. Wang, J. R. Mautz, and R. F. Harrington, "The excess capacitance of a microstrip via in a dielectric substrate," *IEEE J. Technol. Computer Aided Des.*, vol. 9, no. 1, pp. 48–56, Jan. 1990.

[25] M. E. Goldfarb and R. A. Pucel, "Modeling via hole grounds in microstrip," *IEEE Microw. Guided Lett.*, vol. 1, no. 6, pp. 135–137, Jun. 1991.

[26] Y.-J. Zhang, R. Rimolo-Donadio, J. Fan, C. Schuster, and E.-P. Li, "Extraction of via-plate capacitance of an eccentric via by an integral approximation

method," *IEEE Microw. Wireless Compon. Lett.*, vol. 19, no. 5, pp. 275–277, May 2009.

[27] L. Tsang and D. Miller, "Coupling of vias in electronic packaging and printed circuit board structures with finite ground plane," *IEEE Trans. Adv. Packag.*, vol. 26, no. 4, pp. 375–384, Nov. 2003.

[28] Z. Z. Oo, E.-X. Liu, E.-P. Li, X.-C. Wei, Y.-J. Zhang, M. Tan, L.-W. J. Li, and R. Vahldieck, "A semi-analytical approach for system-level electrical modeling of electronic packages with large number of vias," *IEEE Trans. Adv. Packag.*, vol. 31, no. 2, pp. 267–274, May 2008.

[29] T. Wang, R. F. Harrington, and J. R. Mautz, "Quasi-static analysis of a microstrip via through a hole in a ground plane," *IEEE Trans. Microw. Theory Techn.*, vol. 36, no. 6, pp. 1008–1013, Jun. 1988.

[30] P. A. Kok and D. D. Zutter, "Scalar magnetostatic potential approach to the prediction of the excess inductance of grounded via's and via's through a hole in a ground plane," *IEEE Trans. Microw. Theory Techn.*, vol. 42, no. 7, pp. 1229–1237, Jul. 1994.

[31] P. A. Kok and D. D. Zutter, "Capacitance of a circular symmetric model of a via hole including finite ground plane thickness," *IEEE Trans. Microw. Theory Techn.*, vol. 39, no. 7, pp. 1229–1234, Jul. 1991.

[32] X. Gu, R. Rimolo-donadio, Z. Yu, F.-D. Paulis, Y. H. Kwark, M. Cocchini, M. B. Ritter, B. Archambeault, A. E. Ruehli, and C. Schuster, "Fast physics-based via and trace models for signal and power integrity co-analysis," *DesignCon*, pp. 1–20, 2010.

[33] X. Gu and M. B. Ritter, "Application of Foldy-Lax Multiple Scattering Method To Via Analysis in Multi-layered Printed Circuit Board," *DesignCon*, pp. 1–18, 2008.

[34] L. Tsang and X. Chang, "Modeling of vias sharing the same antipad in planar waveguide with boundary integral equation and group T-matrix method," *IEEE Trans. Compon. Packag. Manuf. Technol.*, vol. 3, no. 2, pp. 315–327, Feb. 2013.

[35] X. Chang and L. Tsang, "Fast and broadband modeling method for multiple vias with irregular antipad in arbitrarily shaped power/ground planes in 3-D IC and packaging based on generalized Foldy-Lax equations," *IEEE Trans. Compon. Packag. Manuf. Technol.*, pp. 1–12, 2014.

[36] H. Wang, S. Pan, J. Kim, A. Ruehli, and J. Fan, "Capacitance calculation for via structures using an integral equation method based on partial capacitance," *IEEE Trans. Compon. Packag. Manuf. Technol.*, vol. 3, no. 12, pp. 2134–2146, Dec. 2013.

[37] H. Wang, A. E. Ruehli, and J. Fan, "Capacitance calculation for a shared-antipad via structure using an integral equation method based on partial capacitance," in *Electrical Perform. Electron. Packag. Sys.*, San Jose, Oct. 2011, pp. 271–274.

[38] B. Wu and L. Tsang, "Full-wave modeling of multiple vias using differential signaling and shared antipad in multilayered high speed vertical interconnects," *Prog. Electromagn. Res.*, pp. 129–139, 2009.

[39] T. Zhao, D. R. Jackson, J. T. Williams, H.-Y. D. Yang, and A. A. Oliner, "2-D periodic leaky-wave antennas-part I: metal patch design," *IEEE Trans. Antennas Propag.*, vol. 53, pp. 3505–3514, Nov. 2005.

[40] T. Zhao, D. R. Jackson, J. T. Williams, and A. A. Oliner, "General formulas for 2-D leaky-wave antennas," *IEEE Trans. Antennas Propag.*, vol. 53, pp. 3525–3533, Nov. 2005.

[41] T. Zhao, D. R. Jackson, and J. T. Williams, "2-D periodic leaky-wave antennas-part II: slot design," *IEEE Trans. Antennas Propag.*, vol. 53, pp. 3515–3524, Nov. 2005.

[42] T. Tamir and A. A. Oliner, "Guided complex waves Part 1: fields at an interface," *Proc. Inst. Elect. Eng.*, vol. 110, no. 2, 1963.

[43] T. Tamir and A. A. Oliner, "Guided complex waves Part 2: relation to radiation patterns," *Proc. Inst. Elect. Eng.*, vol. 110, no. 2, pp. 325–334, 1963.

[44] D. R. Jackson and A. A. Oliner, "A leaky-wave analysis of the high-gain printed antenna configuration," *IEEE Trans. Antennas Propag.*, vol. 36, pp. 905–910, Jul. 1988.

[45] S. P. Morgan, "Effect of surface roughness on eddy current losses at microwave frequencies," *J. Appl. Phys.*, vol. 20, no. 4, p. 352, 1949.

[46] Z. Zhu, "Efficient integral equation based algorithms for parasitic extraction of interconnects with smooth or rough surface," PhD thesis, Massachusetts Institute of Technology, 2004.

[47] C. L. Holloway and E. F. Kuester, "Equivalent boundary conditions for a perfectly conducting periodic surface with a cover layer," *Radio Sci.*, vol. 35, no. 3, pp. 661–681, May 2000.

[48] M. Y. Koledintseva, A. Koul, F. Zhou, J. L. Drewniak, and S. Hinaga, "Surface impedance approach to calculate loss in rough conductor coated with dielectric layer," in *Int. Symp. Electromagn. Compat.*, vol. 0, Fort Lauderdale, Jul. 2010, pp. 790–795.

[49] S. G. Pytel, "Multi-gigabit data signaling rates for PWBs including dielectric losses and effects of surface roughness," PhD thesis, University of South Carolina, 2007.

[50] A. F. Horn, J. W. Reynolds, and J. C. Rautio, "Conductor profile effects on the propagation constant of microstrip transmission lines," *IEEE MTT Intl. Microw. Symp. (IMS) Dig.*, pp. 868–871, May 2010.

[51] A. Koul, M. Y. Koledintseva, S. Hinaga, and J. L. Drewniak, "Differential extrapolation method for separating dielectric and rough conductor losses in printed circuit boards," *IEEE Trans. Electromagn. Compat.*, vol. 54, pp. 421–433, Apr. 2012.

[52] Rogers Corporation, *Copper foils for high frequency materials*, 2011. [Online]. Available: http://www.rogerscorp.com/documents/749/acm/Copper-Foils-for-High-Frequency-Circuit-Materials.pdf.

[53] Association Connecting Electronics Industries, *IPC-TM-650 Test Methods Manual*, 2001. [Online]. Available: http://www.ipc.org/TM/2-2_2-2-17a.pdf.

[54] M. Eastham, The Spectral Theory of Periodic Differential Equations. London: Scottish Academic Press, 1973.

[55] C. L. Holloway and E. F. Kuester, "DC internal inductance for a conductor of rectangular cross section," *IEEE Trans. Electromagn. Compat.*, vol. 51, pp. 338–344, May 2009.

[56] J. C. Rautio, "An investigation of microstrip conductor loss," *Microw. Mag.*, vol. 1, no. 4, pp. 60–67, Dec. 2000.

[57] K. S. Oh, J. E. Schutt-Aine, R. Mittra, and B. Wang, "Computation of the equivalent capacitance of a via in a multilayered board using the closed-form Green's function," *IEEE Trans. Microw. Theory Techn.*, vol. 44, no. 2, pp. 5–7, 1996.

[58] G. G. Pan, X. Zhu, and B. Gilbert, "Analysis of transient behavior of vertical interconnects in stacked circuit board layers using quasi-static techniques,"

IEEE Trans. Compon. Packag. Manuf. Technol., vol. 18, no. 3, pp. 521–531, 1995.

[59] C. M. Miller, "Capacitance of shielded balanced-pair transmission line," *Electrical Comm.*, 1956.

[60] Q. Li, L. Tsang, and H. Chen, "Quasi-static parameters, low-frequency solutions, and full-wave solutions of a single-layered via," *Microw. Opt. Technol. Lett.*, vol. 35, no. 1, pp. 34–40, Oct. 2002.

[61] G. Blando, S. Microsystems, J. R. Miller, and D. Winterberg, "Crosstalk in via pin-fields, including the impact of power distribution structures," in *DesignCon*, Santa Clara, 2009, pp. 1–24.

[62] R. Rimolo-Donadio, M. Sebastian, X. Duan, M. Kotzev, and C. Schuster, "Efficient, physics-based via modeling: principles and methods," *IEEE Electromagn. Compat. Mag.*, vol. 1, no. Quarter 1, pp. 55–61, 2012.

[63] R. Rimolo-Donadio, G. Selli, F. D. Paulis, X. Gu, Y. H. Kwark, J. L. Drewniak, H.-D. Bruens, and C. Schuster, "Efficient, physics-based via modeling: integration of striplines," *IEEE Electromagn. Compat. Mag.*, vol. 1, no. Quater 2, pp. 74–81, 2012.

[64] Q. Gu, Y. E. Yang, and M. A. Tassoudji, "Modeling and analysis of vias in multilayered integrated circuits," *IEEE Trans. Microw. Theory Techn.*, vol. 41, no. 2, pp. 206–214, 1993.

[65] Q. Gu, M. A. Tassoudji, Y. S. Poh, R. T. Shin, and J. A. Kong, "Coupled noise analysis for adjacent vias in multilayered digital circuits," *IEEE Trans. Circuits Syst. I, Fundam. Theory Appl.*, vol. 41, no. 12, pp. 796–804, Dec. 1994.

[66] Y.-J. Zhang, J. Fan, and G. Selli, "A generalized multiple scattering method for dense vias with axially anisotropic modes in an arbitrarily shaped plate

pair," *IEEE Trans. Microw. Theory Techn.*, vol. 60, no. 7, pp. 2035–2045, Jul. 2012.

[67] M. Sebastian, X. Duan, M. Kotzev, Y.-J. Zhang, J. Fan, X. Gu, Y. H. Kwark, R. Rimolo-Donadio, H.-D. Bruns, and C. Schuster, "Accuracy of physics-based via models for simulation of dense via arrays," *IEEE Trans. Electromagn. Compat.*, vol. 54, no. 10, pp. 1125–1136, Oct. 2012.

[68] Y.-J. Zhang and J. Fan, "An intrinsic circuit model for multiple vias in an irregular plate pair through rigorous electromagnetic analysis," *IEEE Trans. Microw. Theory Techn.*, vol. 58, no. 8, pp. 2251–2265, Aug. 2010.

[69] R. Rimolo-Donadio, X. Gu, Y. H. Kwark, M. B. Ritter, B. Archambeault, F. D. Pauls, Y. Zhang, J. Fan, H.-D. Bruns, and C. Schuster, "Physics-based via and trace models for efficient link simulation on multilayer structures up to 40 GHz," *IEEE Trans. Microw. Theory Techn.*, vol. 57, no. 8, pp. 2072–2083, Aug. 2009.

[70] M. Sebastian, F. Happ, X. Duan, R. Rimolo-Donadio, H.-D. Bruns, and C. Schuster, "Complete modeling of large via constellations in multilayer printed circuit boards," *IEEE Trans. Electromagn. Compat.*, vol. 3, no. 3, pp. 489–499, Mar. 2013.

[71] L. Tsang, H. Chen, C.-C. Huang, and V. Jandhyala, "Modeling of multiple scattering among vias in planar waveguides using FoldyLax equations," *Microw. Opt. Technol. Lett.*, vol. 31, no. 3, pp. 201–208, Nov. 2001.

[72] C.-C. Huang, L. Tsang, and C. H. Chan, "Multiple scattering among vias in lossy planar waveguides using SMCG method," *IEEE Trans. Adv. Packag.*, vol. 25, no. 5, pp. 181–188, May 2002.

[73] E.-X. Liu, E.-P. Li, Z. Z. Oo, X.-C. Wei, Y.-J. Zhang, and R. Vahldieck, "Novel methods for modeling of multiple vias in multilayered parallel-plate structures," *IEEE Trans. Microw. Theory Techn.*, vol. 57, no. 7, pp. 1724–1733, Jul. 2009.

[74] H. Chen, Q. Li, L. Tsang, C.-C. Huang, and V. Jandhyala, "Analysis of a large number of vias and differential signaling in multilayered structures," *IEEE Trans. Microw. Theory Techn.*, vol. 51, no. 3, pp. 818–829, Mar. 2003.

[75] C.-J. Ong, B. Wu, L. Tsang, and X. Gu, "Full-wave solver for microstrip trace and through-hole via in layered media," *IEEE Trans. Adv. Packag.*, vol. 31, no. 2, pp. 292–302, May 2008.

[76] B. Wu and L. Tsang, "Signal integrity analysis of package and printed circuit board with multiple vias in substrate of layered dielectrics," *IEEE Trans. Adv. Packag.*, vol. 33, no. 2, pp. 510–516, May 2010.

[77] E.-p. Li, X.-C. Wei, A. C. Cangellaris, E.-X. Liu, Y.-J. Zhang, M. D-Amore, J. Kim, and T. Sudo, "Progress review of electromagnetic compatibility analysis technologies for packages, printed circuit boards, and novel interconnects," *IEEE Trans. Electromagn. Compat.*, vol. 52, no. 5, pp. 248–265, May 2010.

[78] X. Guo, D. R. Jackson, and J. Chen, "A semi-analytical model for dense via structures with shared antipad configurations," in *IEEE Int. Microw. Symp.*, Tampa, 2014, pp. 1–3.

[79] R. F. Harrington, "Some theorems and concepts," in *Time-Harmonic Electromagnetic Fields*, New York: Wiley, 2001, p. 118.

[80] H. Xu, D. R. Jackson, and J. T. Williams, "Comparison of models for the probe inductance for a parallel-plate waveguide and a microstrip patch," *IEEE Trans. Antennas Propag.*, vol. 53, no. 10, pp. 3229–3235, Oct. 2005.

[81] T. K. Sarkar, "A note on the choice weighting functions in the method of moments," *IEEE Trans. Antennas Propag.*, vol. 33, no. 4, pp. 436–441, Apr. 1985.

[82] R. F. Harrington, Field Computation by Moment Methods. New York: Wiley, 1993.

[83] B. Tomasic and A. Hessel, "Electric and magnetic current sources in the parallel plate waveguide," *IEEE Trans. Antennas Propag.*, vol. 68, no. 1, pp. 1307–1310, Nov. 1987.

[84] B Peterson and S Ström, "T matrix for electromagnetic scattering from an arbitrary number of scatterers and representations of E(3)," *Phy. Rev. D*, pp. 3661–3678, 1973.

[85] Milton Abramowitz and I. A. Stegun, "Bessel functions of integer order," in *Abramowitz and Stegun: Handbook of Mathematical Functions*, Dover Publications, 1965, ch. 9, p. 363.

[86] K. Knopp, Theory and Application of Infinite Series. New York: Dover, 1990.

[87] R. A. Sigelmann and A. Ishimaru, "Radiation from periodic structures excited by an aperiodic source," *IEEE Trans. Antennas Propag.*, vol. 13, pp. 354–364, May 1965.

[88] D. R. Jackson, P. Burghignoli, G. Lovat, F. Capolino, J. Chen, D. R. Wilton, and A. A. Oliner, "The fundamental physics of directive beaming at microwave and optical frequencies and the role of leaky waves," *Proc. IEEE*, vol. 99, pp. 1780–1805, Oct. 2011.

[89] D. R. Jackson, C. Caloz, and T. Itoh, "Leaky-wave antennas," *Proc. IEEE*, vol. 100, no. 7, pp. 2194–2206, Jul. 2012.

[90] D. R. Jackson and A. A. Oliner, "Leaky-wave antennas," in *Modern Antenna Handbook*, Wiley, 2008, ch. 7, pp. 325–368.

[91] L. Liu, C. Caloz, and T. Itoh, "Dominant mode leaky-wave antenna with backfire-to-endfire scanning capability," *Electron. Let.*, vol. 38, no. 23, pp. 1414–1416, 2002.

[92] G. V. Eleftheriades, A. K. Iyer, and P. C. Kremer, "Planar negative refractive index media using periodically LC loaded transmission lines," *IEEE Trans. Microw. Theory Techn.*, vol. 50, no. 12, pp. 2702–2712, Dec. 2002.

[93] S. Paulotto, P. Baccarelli, F. Frezza, and D. R. Jackson, "A novel technique for open-stopband suppression in 1-D periodic printed leaky-wave antennas," *IEEE Trans. Antennas Propag.*, vol. 57, no. 7, pp. 1894–1906, Jul. 2009.

[94] G. V. Trentini, "Partially reflecting sheet arrays," *IRE Trans. Antennas Propag.*, pp. 666–671, Oct. 1956.

[95] G. Lovat, P. Burghignoli, and D. R. Jackson, "Fundamental properties and optimization of broadside radiation from uniform leaky-wave antennas," *IEEE Trans. Antennas Propag.*, vol. 54, pp. 1442–1452, May 2006.

[96] H.-Y. D. Yang, "Theory of microstrip lines on artificial periodic substrates," *IEEE Trans. Microw. Theory Techn.*, vol. 47, pp. 629–635, May 1999.

[97] H.-Y. D. Yang and D. R. Jackson, "Theory of line-source radiation from a metal-strip grating dielectric-slab structure," *IEEE Trans. Antennas Propag.*, vol. 48, pp. 556–564, Apr. 2000.

[98] Y. Kaganovsky and R. Shavit, "Analysis of radiation from a line source in a grounded dielectric slab covered by a metal strip grating," *IEEE Trans. Antennas Propag.*, vol. 57, pp. 135–143, Jan. 2009.

[99] P. Burghignoli, G. Lovat, F. Capolino, D. R. Jackson, and D. R. Wilton, "Highly polarized, directive radiation from a Fabry-Pérot cavity leaky-wave antenna based on a metal strip grating," *IEEE Trans. Antennas Propag.*, vol. 58, pp. 3873–3883, Dec. 2010.

[100] G. Valerio, P. Burghignoli, P. Baccarelli, and A. Galli, "Input impedance of nonperiodic sources exciting 1-D periodic shielded microstrip structures," *IEEE Trans. Microw. Theory Techn.*, vol. 58, pp. 1796–1806, Jul. 2010.

[101] R. Guzman-Quiros, J. L. Gomez-Tornero, A. R. Weily, and Y. J. Guo, "Electronically steerable 1-D fabry-perot leaky-wave antenna employing a tunable high impedance surface," *IEEE Trans. Antennas Propag.*, vol. 60, pp. 5046–5055, Nov. 2012.

[102] A. Ip and D. R. Jackson, "Radiation from cylindrical leaky waves," *IEEE Trans. Antennas Propag.*, vol. 38, pp. 482–488, Apr. 1990.

[103] X. Guo, D. R. Jackson, and J. Chen, "Leaky-wave analysis of Fabry-Pérot resonant cavity antennas," in *URSI Int. Symp. on Electromagn. Theory*, Hiroshima, 2013, pp. 1091–1093.

[104] R. Qiang, J. Chen, F. Capolino, D. R. Jackson, and D. R. Wilton, "ASMFDTD: A technique for calculating the field of a finite source in the presence of an infinite periodic artificial material," *IEEE Microw. Wireless Compon. Lett.*, vol. 17, pp. 271–273, Apr. 2007.

[105] F. Capolino, D. R. Jackson, D. R. Wilton, and L. B. Felsen, "Comparison of methods for calculating the field excited by a dipole near a 2-D periodic material," *IEEE Trans. Antennas Propag.*, vol. 55, pp. 1644–1655, Jun. 2007.

[106] T. Itoh and R. Mittra, "Spectral-domain approach for calculating the dispersion characteristics of microstrip lines," *IEEE Trans. Microw. Theory Techn.*, vol. 21, pp. 496–499, Jul. 1973.

[107] A. A. Oliner, "Radiating periodic structures: analysis in terms of k vs. β diagrams," in *Short Course on Microwave Field and Network Techniques*, New York, 1963, pp. 1–32.

[108] C. M. Bender and S. A. Orszag, "Asymptotic expansion of integrals," in *Advanced Mathematics Methods for Scientists and Engineers*, New York: McGraw-Hill, 1978, ch. 6, p. 280.

[109] R. E. Collin, "Hertzian dipole radiating over a lossy earth or sea: Some early and late 20th-century controversies," *IEEE Antennas Propag. Mag.*, vol. 46, no. 2, Apr. 2004.

[110] D. R. Wilton, "Computational methods," in *Lectures on Computational Methods in Electromagnetics*, 5, vol. c, 1981, pp. 1–54.

[111] J. Webb, "Edge elements and what they can do for you," *IEEE Transactions on Magnetics*, vol. 29, no. 2, pp. 1460–1465, Mar. 1993.

Appendix A

Periodic Finite Element Eigenvalue Analysis

Our goal is to solve the eigen-frequencies (cutoff) of a periodic cavity (see Figure A.1), which is obtained by solving the following vector wave equation

$$\begin{cases} \nabla \times (\mu_r^{-1} \nabla \times \mathbf{E}) - k_0^2 \epsilon_r \mathbf{E} = -j\omega\mu_0 \mathbf{J}^i, & \mathbf{r} \in V, \\ \hat{\mathbf{n}} \times \mathbf{H} = \mathbf{0}, & \mathbf{r} \in S_3, S_4, \\ \hat{\mathbf{n}} \times \mathbf{E} = \mathbf{0}, & \mathbf{r} \in S_5, S_6, \\ \mathbf{E}_2 = e^{-jk_{z0}\Lambda_r} \mathbf{E}_1, \end{cases} \tag{A.1}$$

which is referred to as the *strong form* [110].

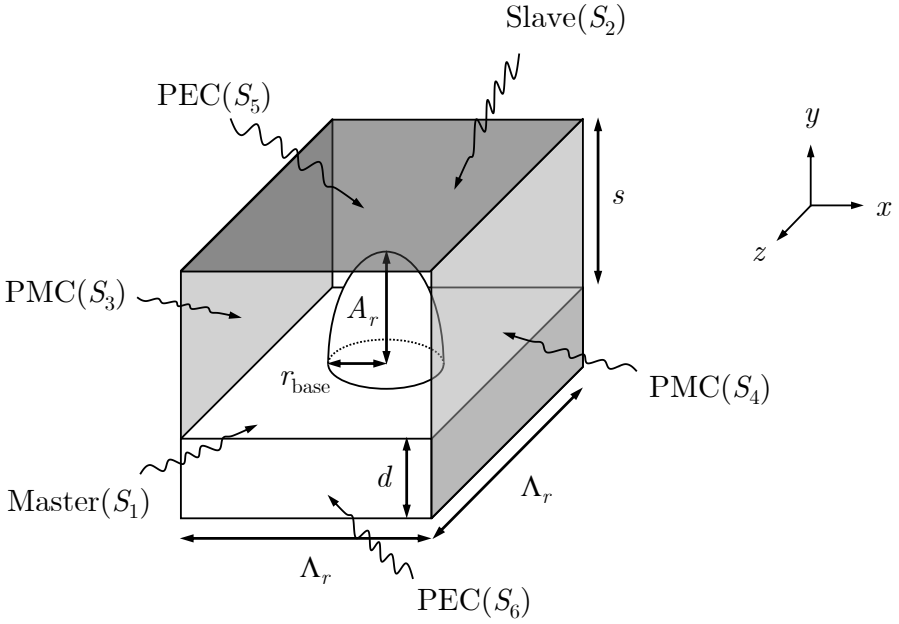

Figure A.1. A periodic cavity.

We start from approximating the solution domain V by finite elements V^e, where V is divided into tetrahedral elements. We represent the vector electric field $\mathbf{E}$ as

$$\mathbf{E} = \sum_{n=1}^{N} V_n \mathbf{\Omega}_n, \tag{A.2}$$

where V_n characterize the intensity of $\mathbf{E}$ along edge n and is to be determined.

$\mathbf{\Omega}_n$ are chosen to be *edge-based basis functions* [111] and ensure tangential continuity and normal discontinuity across element boundaries. Each basis function has a unit tangential component along edge n and linearly goes to 0 on the neighboring edges and remains 0 beyond the neighboring edges. The positive direction of $\mathbf{\Omega}_n$ is assumed to point from the smaller vertex index to a larger one.

A.1 Obtain the Weak Form

We use the basis function $\mathbf{\Omega}_m$ as a testing function to *test* the strong form, and thus obtain the *weak form*

$$< \mathbf{\Omega}_m; \nabla \times (\mu_r^{-1} \nabla \times \mathbf{E}) > - k_0^2 < \mathbf{\Omega}_m; \epsilon_r \mathbf{E} >= -j\omega\mu_0 < \mathbf{\Omega}_m; \mathbf{J}^i > . \tag{A.3}$$

From $\nabla \cdot (\mathbf{A} \times \mathbf{B}) = \mathbf{B} \cdot \nabla \times \mathbf{A} - \mathbf{A} \cdot \nabla \times \mathbf{B}$, we have

$$\begin{aligned} < \mathbf{\Omega}_m; \nabla \times (\mu_r^{-1} \nabla \times \mathbf{E}) >=& < \nabla \times \mathbf{\Omega}_m; \mu_r^{-1} \nabla \times \mathbf{E} > \\ & - \int_V \nabla \cdot (\mathbf{\Omega}_m \times (\mu_r^{-1} \nabla \times \mathbf{E})) dV, \end{aligned} \tag{A.4}$$

in which the last term reduces to

$$\begin{aligned} \int_V \nabla \cdot (\mathbf{\Omega}_m \times (\mu_r^{-1} \nabla \times \mathbf{E})) dV &= \int_S \hat{\mathbf{n}} \cdot (\mathbf{\Omega}_m \times (\mu_r^{-1} \nabla \times \mathbf{E})) dS \\ &= -j\omega\mu_0 \int_S \hat{\mathbf{n}} \cdot (\mathbf{\Omega}_m \times \mathbf{H}) dS = j\omega\mu_0 \int_S \mathbf{\Omega}_m \cdot (\hat{\mathbf{n}} \times \mathbf{H}) dS, \end{aligned} \tag{A.5}$$

where $\hat{\mathbf{n}}$ is the outward normal of the surface S. Let $\mathbf{J}_s = \hat{\mathbf{n}} \times \mathbf{H}$, so that

$$\int_V \nabla \cdot (\mathbf{\Omega}_m \times (\mu_r^{-1} \nabla \times \mathbf{E}))dV = j\omega\mu_0 \int_S \mathbf{\Omega}_m \cdot \mathbf{J}_s dS. \tag{A.6}$$

We arrange the weak-form vector wave equation as given by

$$\begin{aligned} \frac{1}{j\omega\mu_0} < \nabla \times \mathbf{\Omega}_m; \mu_r^{-1} \nabla \times \mathbf{E} > + j\omega\epsilon_0 < \mathbf{\Omega}_m; \epsilon_r \mathbf{E} > \\ - \int_S \mathbf{\Omega}_m \cdot \mathbf{J}_s dS = - < \mathbf{\Omega}_m; \mathbf{J}^i >, \end{aligned} \tag{A.7}$$

where the term $\int_S \mathbf{\Omega}_m \cdot \mathbf{J}_s dS$ vanishes on surfaces S_3, S_4, S_5, S_6. On surfaces S_1 and S_2, the following periodic boundary condition holds,

$$[V_n^{S_2}] = \lambda [V_n^{S_1}], \qquad [I_n^{S_2}] = \lambda [I_n^{S_1}], \tag{A.8}$$

where $\lambda = e^{-jk_{z0}\Lambda_r}$.

Note that both $[V]$ and $[I]$ are unknowns on surfaces S_1 and S_2, which requires an extra set of equations. It is this λ-relation that provides this extra one set of equations.

A.2 Eigenmode Formulation

To solve an eigenvalue problem, the excitation is set to be zero. The system of equations further becomes

$$\begin{bmatrix} [Y_{mn}^{VV}] & [Y_{mn}^{VS_1}] & 0 & [Y_{mn}^{VS_2}] & 0 \\ [Y_{mn}^{S_1V}] & [Y_{mn}^{S_1S_1}] & [\gamma_{mn}^{S_1S_1}] & [Y_{mn}^{S_1S_2}] & [\gamma_{mn}^{S_1S_2}] \\ [Y_{mn}^{S_2V}] & [Y_{mn}^{S_2S_1}] & [\gamma_{mn}^{S_2S_1}] & [Y_{mn}^{S_2S_2}] & [\gamma_{mn}^{S_2S_2}] \end{bmatrix} \begin{bmatrix} [V_n^V] \\ [V_n^{S_1}] \\ [I_n^{S_1}] \\ [V_n^{S_2}] \\ [I_n^{S_2}] \end{bmatrix} = \begin{bmatrix} 0 \\ 0 \\ 0 \end{bmatrix}, \tag{A.9}$$

where the elements in the system matrix can be evaluated by

$$\begin{cases} Y_{mn} = \frac{1}{j\omega\mu_0} < \nabla \times \mathbf{\Omega}_m; \mu_r^{-1} \nabla \times \mathbf{\Omega}_n > + j\omega\epsilon_0 < \mathbf{\Omega}_m; \epsilon_r \mathbf{\Omega}_n >, \\ \gamma_{mn} = - < \mathbf{\Omega}_m; \mathbf{\Omega}_n > . \end{cases} \tag{A.10}$$

Note that the superscript V denotes the basis functions inside the volume V as well as on the PMC surfaces S_3 and S_4.

Clear the zero terms in the linear system (the periodic boundaries S_1 and S_2 do not touch), and then we have

$$\begin{bmatrix} [Y_{mn}^{VV}] & [Y_{mn}^{VS_1}] & 0 & [Y_{mn}^{VS_2}] & 0 \\ [Y_{mn}^{S_1V}] & [Y_{mn}^{S_1S_1}] & [\gamma_{mn}^{S_1S_1}] & 0 & 0 \\ [Y_{mn}^{S_2V}] & 0 & 0 & [Y_{mn}^{S_2S_2}] & [\gamma_{mn}^{S_2S_2}] \end{bmatrix} \begin{bmatrix} [V_n^V] \\ [V_n^{S_1}] \\ [I_n^{S_1}] \\ [V_n^{S_2}] \\ [I_n^{S_2}] \end{bmatrix} = \begin{bmatrix} 0 \\ 0 \\ 0 \end{bmatrix}. \tag{A.11}$$

Defining the unknown vector containing the voltages and currents as $[X]$, we then have an eigenvalue problem for λ such that $[A][X] = \lambda[B][X]$, where

$$\begin{cases} [A] = \begin{bmatrix} [Y_{mn}^{VV}] & [Y_{mn}^{VS_1}] & 0 \\ [Y_{mn}^{S_2V}] & 0 & 0 \end{bmatrix}, \\ [B] = - \begin{bmatrix} 0 & [Y_{mn}^{VS_2}] & 0 \\ [Y_{mn}^{S_1V}] & [Y_{mn}^{S_1S_1}] + [Y_{mn}^{S_2S_2}] & [\gamma_{mn}^{S_1S_1}] + [\gamma_{mn}^{S_2S_2}] \end{bmatrix}. \end{cases} \tag{A.12}$$

The eigenvalue is $\lambda = e^{-jk_{z0}\Lambda_r}$, from which we can solve for a complex fundamental Floquet mode wavenumber k_{z0}. The corresponding eigenvector gives the eigenmode.

A.3 System Matrix Evaluation

It is observed that a basis function $\mathbf{\Omega}_n$ extends to the adjacent tetrahedrons sharing a common edge n. This makes it difficult to evaluate the Y_{mn} and γ_{mn}. However, it is much clearer if we consider it inside a tetrahedral element e with the local basis of $\mathbf{\Omega}^e_{ij}$, since all elements are non-overlapping. The subscript ij is associated with the local indices of the element vertexes i and j and the superscript refers to the element index e.

To parameterize the integral over a tetrahedron, we introduce a set of *normalized volume coordinates* $\xi_i = V_i/V^e$, where V_i is the volume of the sub-tetrahedron that consists of a point with arbitrary location and every vertex except for i. To limit the arbitrary point inside the tetrahedral element e, we have $\sum_{i=1}^{4} \xi_i = 1$. Defining the unit height vector $\hat{\mathbf{h}}_i$ that points to face i, we have

$$\nabla \xi_i = -\hat{\mathbf{h}}_i/h_i = (\mathbf{l}_{jl} \times \mathbf{l}_{kl})/(6V^e), \qquad i \in [1,3], i \neq j \neq l, k > j. \tag{A.13}$$

We note that the vector basis function $\mathbf{\Omega}^e_{ij}$ associated with edge ij should be satisfy two conditions: (a) it should be normal to all edges except for edge ij, and (b) it should have unitary *tangential* component along edge ij.

To satisfy condition (a), it is straightforward that the basis function may take the form $\mathbf{\Omega}^e_{ij} = C\rho_a \hat{\boldsymbol{\phi}}_a$, where (ρ_a, ϕ_a, z_a) is the local cylindrical coordinate in the shaded plane that contains l_{ij} and is perpendicular to l_{kl}, centered at vertex a, as shown in Figure A.2. C is a constant to be determined. The curl of the basis is then found by

$$\nabla \times \mathbf{\Omega}^e_{ij} = -\frac{1}{\rho_a}\frac{\partial}{\partial \rho_a}(\rho_a \Omega^e_{ij\phi})\hat{\mathbf{z}}_a = 2C\hat{\mathbf{z}}_a. \tag{A.14}$$

Since the curl of the basis exists (to the lowest order), the basis function $\mathbf{\Omega}^e_{ij}$ used

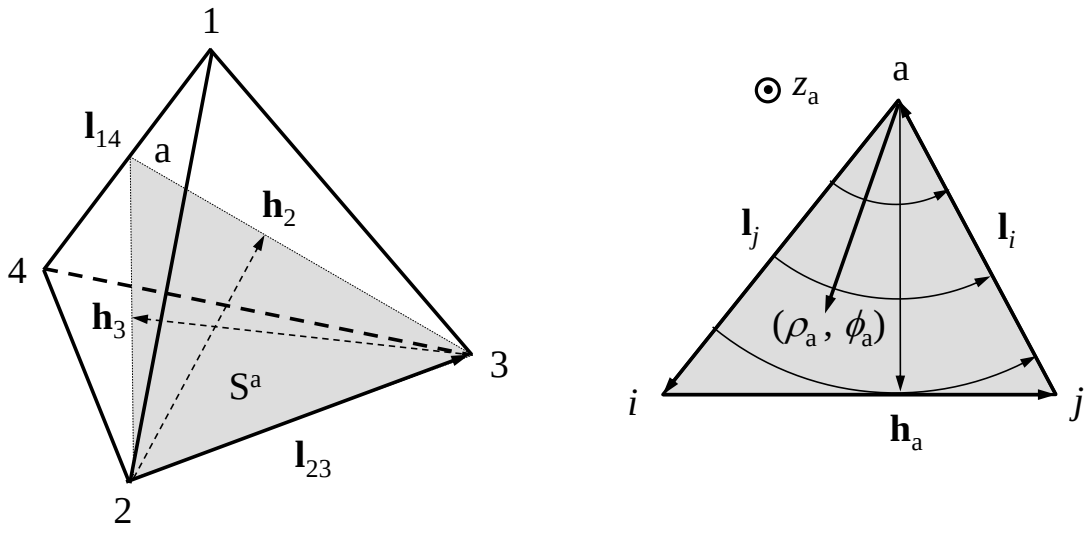

Figure A.2. The curl-conforming basis function. The shaded triangle S^a is perpendicular to l_{14} that contains h_2 and h_3. The local cylindrical coordinate (ρ_a, ϕ_a, z_a) is shown on the right.

here is also referred to as a *curl-conforming* basis.

We then use condition (b) to find the constant C. We note that when $\rho_a = h_a$, $\mathbf{\Omega}^e_{ij} = Ch_a\hat{\boldsymbol{\phi}}_a$. In order to have unitary tangential component, $C = 1/h_a$.

In the local area coordinates for S^a, $\xi_i + \xi_j + \xi_a = 1$. Hence, the basis function can be calculated by

$$\begin{aligned}\mathbf{\Omega}^e_{ij} &= (\rho_a/h_a)\hat{\boldsymbol{\phi}}_a = \hat{\mathbf{z}}_a \times \boldsymbol{\rho}_a/h_a \\ &= \hat{\mathbf{z}}_a \times (\xi_i \mathbf{l}_j - \xi_j \mathbf{l}_i)/h_a \\ &= (-\xi_i l_j \hat{\mathbf{h}}_j + \xi_j l_i \hat{\mathbf{h}}_i)/h_a \\ &= l_{ij}(\xi_i \nabla\xi_j - \xi_j \nabla\xi_i).\end{aligned} \tag{A.15}$$

We can then calculate the element matrix using

$$\int_{V^e} \xi_1^\alpha \xi_2^\beta \xi_3^\gamma \xi_4^\delta dV = \frac{3!V^e\alpha!\beta!\gamma!\delta!}{(\alpha+\beta+\gamma+\delta+3)!}, \tag{A.16}$$

or

$$\int_{S^e} \xi_1^\alpha \xi_2^\beta \xi_3^\gamma dS = \frac{2! A^e \alpha! \beta! \gamma!}{(\alpha+\beta+\gamma+2)!}. \tag{A.17}$$

Hence,

$$\begin{aligned} < \mathbf{\Omega}_{ij}^e; \mathbf{\Omega}_{kl}^e > &= l_{ij} l_{kl} \int_{D^e} (\xi_i \nabla \xi_j - \xi_j \nabla \xi_i) \cdot (\xi_k \nabla \xi_l - \xi_l \nabla \xi_k) dD \\ &= \frac{l_{ij} l_{kl} J^e N_{dim}!}{(N_{dim}+2)!} [(1+\delta_{ik}) \nabla \xi_j \cdot \nabla \xi_l - (1+\delta_{il}) \nabla \xi_j \cdot \nabla \xi_k \\ &\quad - (1+\delta_{jk}) \nabla \xi_i \cdot \nabla \xi_l + (1+\delta_{jl}) \nabla \xi_i \cdot \nabla \xi_k], \end{aligned} \tag{A.18}$$

with $N_{dim} = 3$ for tetrahedral elements ($D = V$) and $N_{dim} = 2$ for triangular elements ($D = S$). J^e is the Jacobian of the element e, and $J^e = V^e$ for tetrahedral elements and $J^e = A^e$ for triangular elements.

Also, it is seen from Eq. (A.15) that $\nabla \times \mathbf{\Omega}_{ij}^e = 2 l_{ij} (\nabla \xi_i \times \nabla \xi_j)$. Therefore

$$< \nabla \times \mathbf{\Omega}_{ij}^e; \nabla \times \mathbf{\Omega}_{kl}^e > = 4 l_{ij} l_{kl} J^e [(\nabla \xi_i \times \nabla \xi_j) \cdot (\nabla \xi_k \times \nabla \xi_l)]. \tag{A.19}$$

$\sigma_{ij}^e \sigma_{kl}^e Y_{ij,kl}^e$ is added to Y_{mn} (similar for γ_{mn}) if m, n are edge DOF indices associated with local edges ij and kl, receptively, of element e. σ_{ij}^e incorporates the sign accounting for the reference choice of the direction of edge ij: $\sigma_{ij}^e = 1$ if the local edge ij is parallel to the global edge m, and $\sigma_{ij}^e = -1$ if is anti-parallel to edge m. Globally, the positive direction for edge m is pointed from the smaller index to the larger index.

Appendix B

TEM Mode Field Calculation

It is well-known that for a wave-guiding structure like a transmission line shown in Figure 2.9 with a guided mode propagating along z-direction, the electromagnetic field can be written in the form

$$\begin{cases} \mathbf{E}(x,y,z) = [\hat{\mathbf{t}}E_t(x,y) + \hat{\mathbf{z}}E_z(x,y)]e^{-jk_z z}, \\ \mathbf{H}(x,y,z) = [\hat{\mathbf{t}}H_t(x,y) + \hat{\mathbf{z}}H_z(x,y)]e^{-jk_z z}. \end{cases} \tag{B.1}$$

The subscript t represents the transverse field components and the subscript z represents the z-directed field components.

For ideal (lossless) transmission lines where the guided mode is a transverse-electromagnetic (TEM) mode, both E_z and H_z are zero. In this case, the wavenumber becomes $k_z = k_0\sqrt{\mu_r\epsilon_r}$, where $k_0 = \omega\sqrt{\mu_0\epsilon_0}$ is the wavenumber of free space. For a TEM mode, the transverse electric field $\mathbf{E}_t$ satisfies the following conditions,

$$\begin{cases} \nabla \cdot \mathbf{E}_t = 0, \\ \nabla \times \mathbf{E}_t = 0, \end{cases} \tag{B.2}$$

which are equivalent to the Laplace condition $\nabla^2\Phi = 0$, where Φ is the static potential and $\mathbf{E}_t = -\nabla\Phi$.

Once we numerically solved for the static potential $\Phi(x,y)$, one can obtain the transverse electromagnetic fields as

$$\mathbf{E}_t = -\nabla\Phi, \qquad \mathbf{H}_t = \frac{1}{\eta_0}\sqrt{\frac{\epsilon_r}{\mu_r}}(\hat{\mathbf{z}} \times \mathbf{E}_t), \tag{B.3}$$

where $\eta_0 = \sqrt{\mu_0/\epsilon_0}$ is the wave impedance of free space.

The transverse plane of a stripline transmission line structure used to solve the Laplace equation $\nabla^2\Phi = 0$ is shown in Figure B.1. The boundary condition for Φ is the Dirichlet (or first-type) boundary condition on the conductor surfaces. We assume the static potential is $\Phi = 1$ V on the surface of the strip conductor and $\Phi = 0$ V on the ground planes and at a infinite distance away from the strip.

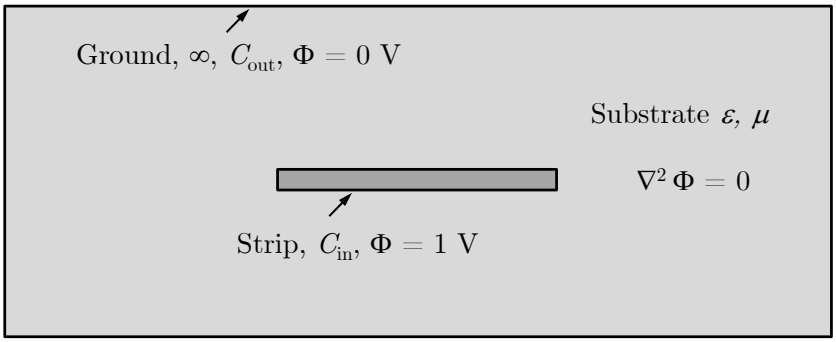

Figure B.1. The cross-sectional geometry of a stripline transmission line used to solve the Laplace equation $\nabla^2\Phi = 0$.

Note that the same Laplace equation also describes the static condition. Hence, the static potential Φ can be written in an integral form that

$$\Phi(\boldsymbol{\rho}) = -\frac{1}{2\pi\epsilon_0\epsilon_r}\oint_C \ln|\boldsymbol{\rho} - \boldsymbol{\rho}'|\rho_s(\boldsymbol{\rho}')dl', \tag{B.4}$$

where ρ_s is the surface charge density on the conductor boundary. Here $\boldsymbol{\rho}$ denotes the observation coordinate system and $\boldsymbol{\rho}'$ denotes the source coordinate system.

To obtain the numerical value of the surface charge density ρ_s, one can use MoM. The boundary l' is first discretized into N small segments and $\rho_s(\boldsymbol{\rho}')$ and $\Phi(\boldsymbol{\rho})$ are represented by linear combinations of the basis functions (rectangular pulses) as shown

in Figure B.2, so that

$$\rho_s(\boldsymbol{\rho}') = \sum_{n=1}^{N} Q_n \Pi_n(\boldsymbol{\rho}'), \tag{B.5}$$

$$\Phi(\boldsymbol{\rho}) = \sum_{m=1}^{N} V_m \Pi_m(\boldsymbol{\rho}). \tag{B.6}$$

Here the basis function is defined as

$$\Pi_n(\boldsymbol{\rho}) = \begin{cases} 1, & \boldsymbol{\rho} \in l_n, \\ 0, & \boldsymbol{\rho} \notin l_n. \end{cases} \tag{B.7}$$

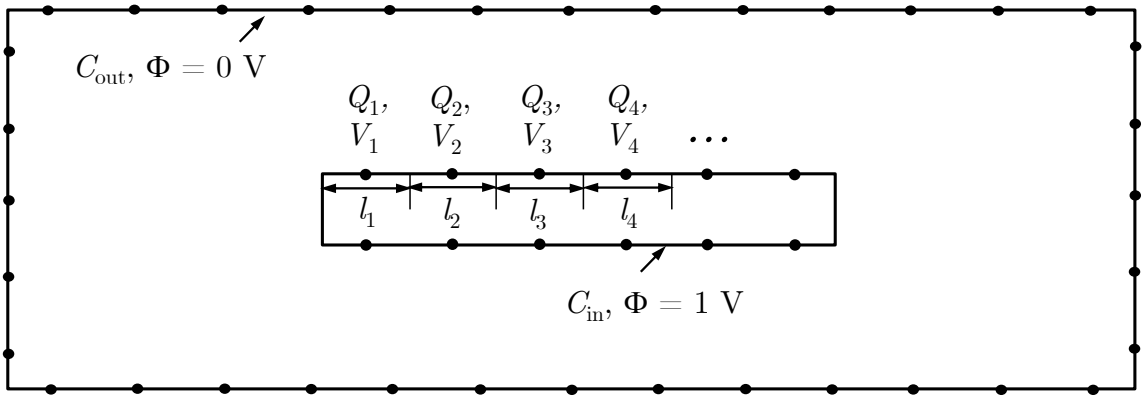

Figure B.2. Boundaries discretization. Basis functions $\Pi_n(\boldsymbol{\rho})$ in the rectangular pulse form are used to represent the unknown ρ_s and Φ.

Performing Galerkin's test on Eq. (B.4) (multiplying both sides with the basis function and then integrating along the entire boundary domain) yields a static potential integral equation in a discretized matrix form,

$$[S_{mn}][Q_n] = [V_m], \tag{B.8}$$

where

$$S_{mn} = -\frac{1}{2\pi\epsilon_0\epsilon_r}\int_{l_n}\int_{l_m} \ln|\boldsymbol{\rho}'_n - \boldsymbol{\rho}_m|\Pi_n(\boldsymbol{\rho}'_n)\Pi_m(\boldsymbol{\rho}_m)dl_m dl_n \tag{B.9}$$
$$= -\frac{1}{2\pi\epsilon_0\epsilon_r}\int_{l_n}\int_{l_m} \ln|\boldsymbol{\rho}'_n - \boldsymbol{\rho}_m| dl_m dl_n,$$

and

$$V_m = \int_{l_m} \Phi(\boldsymbol{\rho}_m)\Pi_m(\boldsymbol{\rho}_m)\Pi_m(\boldsymbol{\rho}_m)dl_m \tag{B.10}$$
$$= \Phi(\boldsymbol{\rho}_m)l_m.$$

The surface charge density ρ_s is then solved using $[Q_n] = [S_{mn}]^{-1}[V_m]$.

In order to obtain the numerical value for the matrix elements S_{mn} for $m \neq n$, one can perform the Gaussian-quadrature integral. And for $m = n$, there exists a logarithm singularity that is integrable. An analytic formula for S_{mm} is

$$S_{mm} = -\frac{l_m^2}{2\pi\epsilon}(\ln l_m - 1.5). \tag{B.11}$$

Appendix C

Measurement of Dielectric Properties

C.1 Existing Measurement Methods

The most popular way to measure the dielectric properties of a transmission line is through its frequency response, e.g., the scattering parameter (S-parameter) S_{21}. If all ports of the transmission line are matched, the wavenumber k_z on the transmission line and the S_{21}-parameter are related by

$$S_{21} = e^{-jk_z L}, \tag{C.1}$$

where L is the length of the stripline and $k_z = \beta - j\alpha$, with α being the attenuation constant and β being the phase constant. The wavenumber k_z is related to the complex dielectric constant ϵ_{rc} by

$$k_z = \omega\sqrt{\mu_0\epsilon_0} \cdot \sqrt{\mu_r\epsilon_{rc}} = \frac{2\pi f\sqrt{\mu_r}}{c_0}\sqrt{\epsilon_{rc}}, \tag{C.2}$$

where $c_0 = 299792458m/s$ is the speed of light in vacuum. Most laminating substrate materials are non-magnetic and thus for usual calculations, $\mu_r = 1.0$.

ϵ_r, or Dk, is the real part of ϵ_{rc}. It can be computed from the phase delay information of the measured S-parameter as

$$\mathrm{Dk} = \Re\left[\frac{c_0}{2\pi f\sqrt{\mu_r}}\frac{\ln S_{21}}{-jL}\right]^2. \tag{C.3}$$

The loss tangent $\tan\delta$, or Df, is the ratio of the imaginary and real part of ϵ_{rc}, and is computed from the measured dielectric attenuation α_d (given that the whole

system is low-loss) as

$$\mathrm{Df} = \frac{c_0 \alpha_d}{\pi f \sqrt{\epsilon_r}}. \tag{C.4}$$

Usually the dielectric loss is not equal to the total loss, so the separation of dielectric loss from the total loss is necessary.

For conductors having smooth surfaces, the loss separation is straight forward. The dominant frequency components manifested in the insertion loss in the S-parameter measurements in this frequency range are $\sqrt{\omega}$, ω and ω^2, so that

$$\alpha_T = K_1\sqrt{\omega} + K_2\omega + K_3\omega^2. \tag{C.5}$$

In Eq. (C.5), the first term in frequency is attributed to the conductor loss $\alpha_{c,\mathrm{smooth}}$ which simply scales with $\sqrt{\omega}$, and the last two terms with ω and ω^2 are attributed to dielectric loss $\alpha_{d,\mathrm{smooth}}$, indicating

$$\begin{cases} \alpha_{c,\mathrm{smooth}} = K_1\sqrt{\omega}, \\ \alpha_{d,\mathrm{smooth}} = K_2\omega + K_3\omega^2. \end{cases} \tag{C.6}$$

The frequency dependency of α_T for a stripline with rough conductors can be also expressed in the form of Eq. (C.5). When the conductor surface is rough, however, the separation of dielectric loss becomes a difficult task because the conductor loss does not purely scale with $\sqrt{\omega}$.

For rough conductors, the conductor loss actually depends on all three terms on the right-hand-side of Eq. (C.5) and is usually entangled with the dielectric loss in most existing methods, which potentially gives larger Df values. In addition, the extra loss due to roughness is closely related to the roughness level (roughness height, shape, surface area, etc.) so that the extracted Df value will change for different copper foils,

even with identical dielectric substrate. This is inconvenient in practical applications.

C.2 Differential Extrapolation Method

Recently, an experimental-based method to separate losses due to frequency-dependent PCB dielectric laminates and conductors, including loss originating from conductor roughness, has been proposed [51]. This method allows for the extraction of a dissipation factor $\tan\delta$ of a PCB dielectric from the loss contributions of the copper foil roughness in the insertion loss for the PCB transmission line.

The approach requires at least three test samples with the same substrate, though different copper foil roughness profiles (e.g., STD–standard, VLP–very-low-profile, and HVLP–hyper-very-low-profile foils). A differential-extrapolation is used and is briefly summarized.

In the differential extrapolation method, the total loss α_T is recognized as three types of losses. They are (a) conductor loss assuming the conductors are smooth $\alpha_{c,\text{smooth}}$, (b) an extra conductor loss caused by surface roughness $\alpha_{c,\text{rough}}$ and (c) the dielectric loss α_d. The expressions for these three losses are

$$\begin{cases} \alpha_{c,\text{smooth}} = a\sqrt{\omega}, \\ \alpha_{c,\text{rough}} = b\sqrt{\omega} + c\omega + d\omega^2, \\ \alpha_{d,\text{rough}} = e\omega + f\omega^2, \end{cases} \tag{C.7}$$

where the unknowns e and f are to be solved to calculate the dielectric loss. Collecting and combining terms gives the relations between the e, f and the K coefficients in Eq. (C.5) as

$$\begin{cases} K_2 = c + e, \\ K_3 = d + f. \end{cases} \tag{C.8}$$

Two degrees of freedom e and f requires at least two equations. The equations

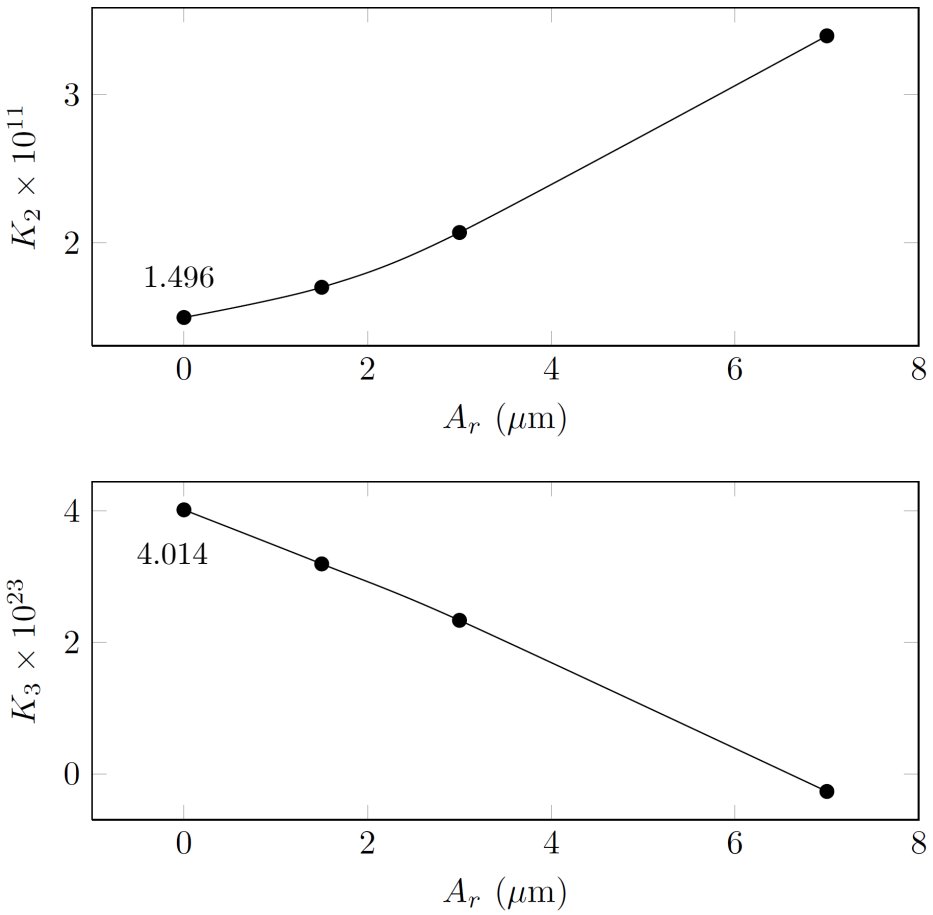

Figure C.1. The extrapolations on (a) K_2 and (b) K_3 as functions of roughness height A_r to zero using a smooth quadratic polynomial fit. When $A_r = 0$, $K_2 = e = 1.496 \times 10^{-11}$ and $K_3 = f = 4.014 \times 10^{-23}$.

describe the relationship between the K-coefficients and the roughness parameters and can be constructed on two foils with different levels of roughness. Once the K values are determined for two A_r, extrapolating the $K - A_r$ functions to $A_r = 0$ yields their values for smooth conductors. And for smooth conductors, $\alpha_{c,\text{rough}} = 0$, c and d vanish, and then $K_2 = e$ and $K_3 = f$. Therefore, the "cleaned from roughness" dielectric loss is obtained.

We here give an example illustrating the differential extrapolation method. Three striplines with identical dielectric substrate but various conductor surface roughness height A_r are used to separate the losses. The values of the curve-fitting coefficients are summarized in Table C.1 and the coefficients obtained by extrapolation of the K-functions are shown in Figure C.1. These values are then substituted back in Eq. (C.7) to calculate the frequency-dependent dielectric loss α_d.

Table C.1. Differential extrapolation K-coefficients ($\alpha_T = K_1\sqrt{\omega} + K_2\omega + K_3\omega^2$)

Foil Type	A_r (μm)	$K_1 \times 10^6$	$K_2 \times 10^{11}$	$K_3 \times 10^{23}$
STD	7.0	1.386	3.399	-0.268
VLP	3.0	2.200	2.070	2.334
HVLP	1.5	2.309	1.745	3.192

Hence, the frequency dependence of the dissipation factor $\tan\delta$, or Df, is extracted. Figure C.2 shows the dielectric properties of the substrate material. The dielectric constant ϵ_r, or Dk, is extracted using the traveling wave transmission-line method from the S-parameters of the smoothest foil (HVLP).

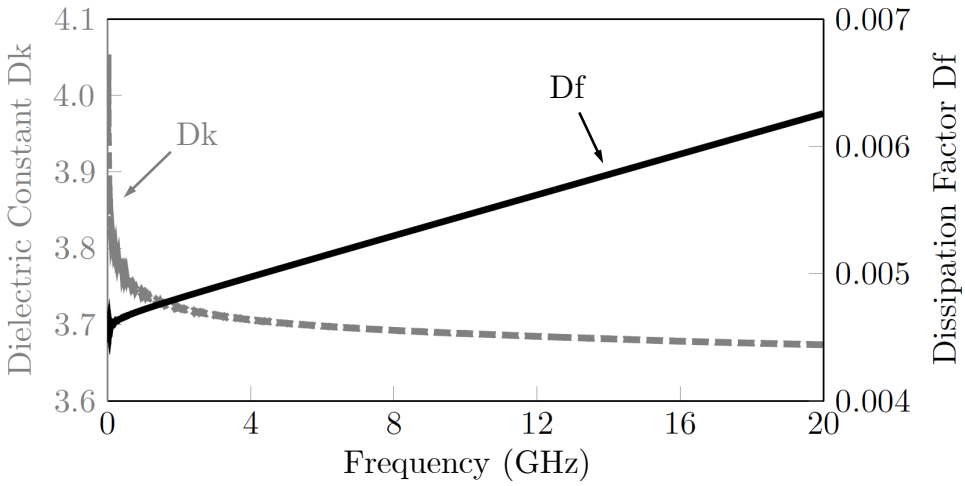

Figure C.2. Dielectric properties of the PCB test board substrate material. Solid line: dissipation factor $\tan\delta$, or Df. Dashed line: dielectric constant ϵ_r, or Dk.

Appendix D

Spectral Periodic MoM Formulation

The electrical fields radiated from the periodic patches and dipoles are first expanded into space-harmonics, namely

$$\begin{cases} E^{\infty}_{x,\text{patch}} = \frac{1}{ab}\sum_{i=1}^{\infty} A^{\infty}_{00;i} \sum_{p=-\infty}^{\infty}\sum_{q=-\infty}^{\infty} \tilde{G}_{xx}(k_{xp}, k_{yq}; 0)\tilde{B}_i(k_{xp}, k_{yq}) e^{-j(k_{xp}x + k_{yq}y)}, \\ E^{\infty}_{x,\text{dipole}} = \frac{1}{ab}\sum_{p=-\infty}^{\infty}\sum_{q=-\infty}^{\infty} \tilde{G}_{xx}(k_{xp}, k_{yq}; z_d)(Il) e^{-j[k_{xp}(x-x_d) + k_{yq}(y-y_d)]}, \end{cases} \tag{D.1}$$

where $A^{\infty}_{00;i}$ measures the current intensity of at the center of patch (0, 0).

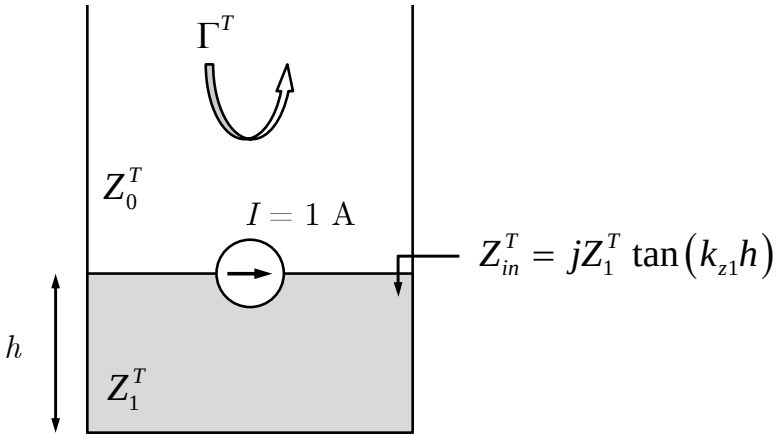

Figure D.1. The equivalent circuit to compute the spectral domain Green's function $\tilde{G}_{xx}$. The impedance seen by the current source at the interface should be $Z_0 \parallel jZ_1 \tan(k_{z1}h)$.

The Green's function relating $\tilde{J}_{sx}$ and $\tilde{E}_x$ for a grounded dielectric slab structure from TEN analysis is ($z < 0$)

$$\tilde{G}_{xx}(k_{xp}, k_{yq}; z) = -\left[\frac{(k_{xp}/k_\rho)^2}{D^{\text{TM}}(k_{z0pq})} + \frac{(k_{yq}/k_\rho)^2}{D^{\text{TE}}(k_{z0pq})}\right]\left(\frac{\sin(k_{z1}(z+h))}{\sin(k_{z1}h)}\right), \tag{D.2}$$

where D^{T} corresponds to the net TM_z or TE_z wave-admittance at the dielectric-air

interface (see Figure D.1), and is given by

$$D^{\mathrm{T}}(k_{z0}) = Y_0^{\mathrm{T}}(k_{z0}) - jY_1^{\mathrm{T}}(k_{z0})\cot(k_{z1}h), \tag{D.3}$$

where

$$Y^{\mathrm{TM}}(k_{z0}) = \frac{\omega\epsilon}{k_{z0}}, \quad Y^{\mathrm{TE}}(k_z) = \frac{k_{z0}}{\omega\mu}. \tag{D.4}$$

The wavenumber k_z is computed from $k_z^2 = k^2 - k_x^2 - k_y^2$. The correct choice for k_{z0} and k_{z1} should both be the "proper" one: the one with negative imaginary part.

A reflection coefficient Γ^{T} can also be computed as

$$\Gamma^{\mathrm{T}} = \frac{jZ_1^{\mathrm{T}}\tan(k_{z1}h) - Z_0^{\mathrm{T}}}{jZ_1^{\mathrm{T}}\tan(k_{z1}h) + Z_0^{\mathrm{T}}}. \tag{D.5}$$

Apply Galerkin's method, i.e., multiplying both sides of Eq. (4.2) with the basis function B_j and then integrating over the surface area of patch $(0,0)$, the resulting E-field integration equation (EFIE) is given by Eq. (4.8), where

$$\begin{cases} Z_{ij}^{\infty} = -\frac{1}{ab}\sum\limits_{p=-\infty}^{\infty}\sum\limits_{q=-\infty}^{\infty}\tilde{G}_{xx}(k_{xp},k_{yq};0)\tilde{B}_i(k_{xp},k_{yq})\tilde{B}_j(-k_{xp},-k_{yq}), \\ R_j^{\infty} = \frac{1}{ab}\sum\limits_{p=-\infty}^{\infty}\sum\limits_{q=-\infty}^{\infty}\tilde{G}_{xx}(k_{xp},k_{yq};z_d)\tilde{B}_j(-k_{xp},-k_{yq})(Il)e^{j(k_{xp}x_d+k_{yq}y_d)}. \end{cases} \tag{D.6}$$

Appendix E

EFIE Approach with 1-D Discretization

We briefly summarize the electric field integral equation (EFIE) approach using 1-D discretization and integration along the antipad boundary, similar to methods described in [34], [35]. The goal is to solve for the induced via currents by enforcing the EFIE (in terms of ϕ-harmonics) on the surface of the via barrels so that $A_{zl}^{\text{sca}} = -A_{zl}^{\text{inc}}$, for each azimuthal n-mode and vertical l-mode.

The incident field onto barrel p due to the antipad aperture radiation at barrel q is computed as

$$A_{zl}^{\text{inc}} = -\frac{j\omega\mu}{k_{\rho l}^2}\hat{\mathbf{z}} \cdot (\nabla \times \mathbf{F}_l). \tag{E.1}$$

The electrical vector potential $\mathbf{F}_l$ due to $\mathbf{M}_l$ is given by

$$\mathbf{F}_l = \epsilon \iint_{S'} \mathbf{M}_l(\boldsymbol{\rho}')G_l(\boldsymbol{\rho}, \boldsymbol{\rho}')dS', \tag{E.2}$$

where $\boldsymbol{\rho}$ denotes the observation coordinate (barrel p) and $\boldsymbol{\rho}'$ denotes the source coordinate (barrel q). $\mathbf{M}_l$ is the l-order Fourier spectrum of the magnetic surface current $\mathbf{M}_s$ located at $z = z'$ (used to represent the antipad at barrel q),

$$\mathbf{M}_l(\rho', \phi') = d_l\mathbf{M}_s = \frac{2\cos(k_{zl}z')}{h(1+\delta_{l0})}\mathbf{M}_s. \tag{E.3}$$

$G_l(\boldsymbol{\rho}, \boldsymbol{\rho}') = (-j/4)H_0^{(2)}(k_{\rho l}|\boldsymbol{\rho} - \boldsymbol{\rho}'|)$ is the parallel-plate Green's function. S' is the antipad area related to barrel q.

Using the TEM port assumption ($\mathbf{M}_s = \hat{\mathbf{z}}' \times \nabla'\Phi$ and $\nabla^{2\prime}\Phi = 0$) and the fact that

$\nabla = -\nabla'$, we have

$$\nabla \times \mathbf{F}_l = \hat{\mathbf{z}}' \epsilon d_l \iint_{S'} \nabla' \cdot (G_l \nabla' \Phi) dS'. \tag{E.4}$$

Applying the 2-D divergence theorem, we obtain the incident field expression,

$$A_{zl}^{\text{inc}} = \frac{j\omega\mu d_l}{k_{\rho l}^2} \oint_{C'} \rho_s(\boldsymbol{\rho}') G_l(\boldsymbol{\rho}, \boldsymbol{\rho}') dl', \tag{E.5}$$

as we recognize $\hat{\mathbf{n}}' \cdot \nabla' \Phi = (1/\epsilon)\rho_s$, $\hat{\mathbf{n}}'$ being the outward normal of C' (the boundary of S').

The scattered field from the barrel current radiation can be expressed by Eq. (3.10) – Eq. (3.12). Hence, we can solve for the coefficients $c_n^{q;l}$ using similar procedures as discussed in Section II-B. In fact, we can use the identical system matrix $[T_{m,n}^{p,q;l}]$ as given in Eq. (3.16), but a different right-hand-side. This is because of the incident/scattered-field formulation. The new RHS vector $[b_m^{p;l}]$ has the expression of

$$b_m^{p;l} = -\frac{1}{2\pi} \int_0^{2\pi} A_{zl}^{\text{inc}} e^{-jm\phi} d\phi, \tag{E.6}$$

which is in the form of *two* line integrals and can be simplified using the property

$$\oint_C G_l(\boldsymbol{\rho}, \boldsymbol{\rho}') e^{jm\phi} dl = \frac{\pi a J_m(k_{\rho l} a)}{2j} H_m^{(2)}(k_{\rho l} \rho_p') e^{jm\phi_p'}, \tag{E.7}$$

where C is the boundary of via p, having a radius of a. Here $\boldsymbol{\rho}_p' = \boldsymbol{\rho}' - \boldsymbol{\rho}_p$ with $\boldsymbol{\rho}_p$ being the center of via p. This gives the final formula for the RHS as

$$b_m^{p;l} = \frac{\omega\mu J_m(k_{\rho l} a) \cos(k_{zl} z')}{-2k_{\rho l}^2 h(1+\delta_{l0})} \oint_{C'} \rho_s H_m^{(2)}(k_{\rho l} \rho_p') e^{-jm\phi_p'} dl'. \tag{E.8}$$

It is noted the numerical integration above is along the antipad boundary, which requires only a 1-D discretization.

The l-order current at barrel q is related to the $c_n^{q;l}$ coefficient by taking the $n = 0$ surface current density and multiplying by $2\pi a$,

$$I_z^{q;l} = \frac{j4c_0^{q;l}}{\mu J_0(k_{\rho l}a)}, \tag{E.9}$$

and the total port current is obtained by summing the components for each l-order mode.

Appendix F

Estimation of Bessel Function Calls

F.1 Calls of Bessel Functions for the Proposed Method

The proposed algorithm is a 2.5-D approach that requires many evaluations of the Bessel functions, i.e., $J_n(\cdot)$, $H_n^{(2)}(\cdot)$. We can therefore estimate the computational cost based on the number of calls of the Bessel functions needed to generate the system of equations Eq. (3.15). In the following, the total number of calls of the Bessel functions required to generate the full S matrix at a single frequency point is evaluated.

For the lower-order vertical modes, we need to build the system matrix $[T_{m,n}^{p,q;l}]$ to describe the interaction among via posts. Making use of the symmetry that $T_{m,n}^{q,p;l} = (-1)^{n-m} T_{m,n}^{p,q;l}$ for $p \neq q$, it requires n_T^{low} calls of the Bessel functions where

$$n_T^{\text{low}} = P(2N+1) + P(P-1)(2N+1)^2. \tag{F.1}$$

Once we have solved for the coefficients $[c_n^{q;l}]$, we can compute the testing frill radiation A_{zB} by sampling along the antipad outer boundary (the integration of A_{zB} along the inner boundary is already given by $[b_m^{p;l}]$). It should be noted that for multiple vias sharing one antipad, the calculation of A_{zB} is required only once for each antipad. Supposing we have P_{out} points along the *outer* boundary of the antipad, this requires n_A^{low} calls of the Bessel functions for the A_{zB} evaluated on all antipads,

$$n_A^{\text{low}} = P(2N+1) P_{\text{out}} N_{\text{antipad}}, \tag{F.2}$$

where N_{antipad} is the number of antipads of the system.

For the higher-order vertical modes, on the other hand, it is not necessary to build

the $[T^{p,q;l}_{m,n}]$ to compute A_{zB}. Instead, we assume that the currents on all via barrels are negligible except for the one where the testing frill is located (barrel *test*). This assumption is valid as long as the ratio of the self-term and the mutual-term of the $[T]$ matrix is large enough. Since barrel *test* radiates as if radiating alone in terms of the higher-order modes, only the $c_0^{test;l}$ coefficient contributes to the total radiation. Hence the higher-order A_{zB} calculation requires n_A^{high} calls of the Bessel functions,

$$n_A^{\text{high}} = P_{\text{out}} N_{\text{signal}}, \tag{F.3}$$

where N_{signal} is the number of signal vias (the vias that have an antipad associated with them).

For vertical modes with even higher order such that the radiation for barrel *test* is noticeable only along the boundary of barrel *test* Eq. (3.18), we do not need any Bessel functions for the A_{zB} evaluation.

In summary, the total calls n_{total} of the Bessel functions required by the proposed algorithm is

$$n_{\text{total}} = L^{\text{low}}(n_T^{\text{low}} + n_A^{\text{low}}) + L^{\text{high}} n_A^{\text{high}}, \tag{F.4}$$

where L^{low} is the number of lower-order vertical modes l that satisfies

$$\frac{|H_0^{(2)}(k_{\rho l}a)|}{|J_0(k_{\rho l}a)H_0^{(2)}(k_{\rho l}s)|} < t_T, \tag{F.5}$$

and L^{high} is the number of higher-order vertical modes l, with l outside the lower-order range and satisfying

$$\frac{|H_0^{(2)}(k_{\rho l}a)|}{|H_0^{(2)}(k_{\rho l}b)|} < t_T. \tag{F.6}$$

Here the threshold number t_T is chosen to be a large number, e.g., $t_T = 10^4$. $k_{zl} = l\pi/h$ is the vertical wavenumber and $k_{\rho l} = \sqrt{k^2 - k_{zl}^2}$ is the horizontal wavenumber.

F.2 Calls of Bessel Functions for 1-D EFIE

For the 1-D EFIE approach with the identical system matrix $[T_{m,n}^{p,q;l}]$, we have the same n_T^{EFIE} as given in Eq. (F.1). The right-hand-side incident-field vector is computed from a 1-D integral along the antipad boundary (inner and outer boundary), which is similar to what has been proposed in [34], [35], as

$$b_m^{p;l} = \frac{\omega\mu J_m(k_{\rho l}a)\cos(k_{zl}z')}{-2k_{\rho l}^2 h(1+\delta_{l0})} \oint_{C'} \rho_s(\rho_p', \phi_p') H_m^{(2)}(k_{\rho l}\rho_p') e^{-jm\phi_p'} dl', \tag{F.7}$$

where (ρ_p', ϕ_p') is measured from the center of barrel p, and ρ_s is the surface charge density at the boundary of the antipad. Assume there are P_{in} sample points along the antipad inner boundaries and P_{out} along the outer boundaries. We then have

$$n_A^{\text{EFIE}} = P(2N+1)(P_{\text{out}} + P_{\text{in}} + 1)N_{\text{signal}}, \tag{F.8}$$

and the total calls $n_{\text{total}}^{\text{EFIE}}$ of Bessel functions required by the 1D-EFIE method is

$$n_{\text{total}}^{\text{EFIE}} = (L+1)(n_A^{\text{EFIE}} + n_T^{\text{EFIE}}). \tag{F.9}$$

It should be noted that the above estimate is based on Eq. (F.7). Indeed, it is possible to program the 1D-EFIE method more efficiently using similar techniques as in the proposed approach. For example, one can use different formulations for different vertical modes, and the Hankel functions used in Eq. (F.7) can also be stored to reduce the number of calls. These were not done here in the given estimates, however.